Stability of All-Inorganic Metal Halide Perovskite Nanocrystals Encapsulated in Cyclic Olefin Copolymer and Graphene at Room and Cryogenic Temperatures

Mutibah S. Alanazi

Queen's College

University of Oxford

A thesis submitted for the degree of

Doctor of Philosophy

Trinity 2024

Acknowledgements

The author would like to seize this moment to briefly depart from the passive voice.

I was privileged to have a group of supervisors who provided valuable expertise and guidance during my PhD, supporting me throughout the 38-month journey. The time that I spent at Oxford has left me indebted to many people.

First and foremost, I would like to express my profound gratitude to my supervisor, Professor Robert Taylor, for his unwavering support, invaluable guidance, and wonderful patience over the past four years. He gave me a lot of space to delve into different projects. His profound understanding in quantum photonics and optoelectronics , material sciences and invaluable guidance are instrumental in keeping me on track to successfully complete my Ph.D. In addition, his passion for science greatly impacts, inspires, and drives me to pursue my future Ph.D. I am incredibly grateful for his presence and support at every step, as all my works presented in this thesis, or ongoing projects rely on his invaluable contributions.

I would like to express my gratitude to Tristan Farrow, who consistently generates intriguing experimental ideas rooted in profound principles of physics. I genuinely appreciate his invaluable help, especially his professional and encouraging mentorship throughout my first PhD project, which centered around synthesizing inorganic quantum dots, methods for encapsulating them, and the essential fabrication techniques of a microcavity. These projects have influenced my perspective on the structure of authentic research and honed my fundamental abilities in cryogenic systems, sample growth, and optical measurement. Regarding the technical aspects of the project, it is important to acknowledge the contribution of Professor Henry Snaith from the University of Oxford. He has been a generous collaborator and has provided the samples that were examined in Chapters 3 and 4 of this thesis. I would like to express my sincere appreciation to Ashley Marshall and Shoani Kar in his group for their invaluable contributions in photographing the transmission electron microscope images and X-ray diffraction data presented in this thesis.

Thanks to their valuable contributions, I was able to achieve the results enclosed here. In addition, I would like to express my deepest gratitude to Youngsin Park, who works at the Ulsan National Institute of Science and Technology. He has collaborated with me on numerous experiment measurements and significantly contributed to the data analysis in Chapter 6 of this thesis. His collaborator, Atanu Jana from Dongguk University, has

fabricated of graphene-covered $CsPbBr_3$ quantum dot and has taken all the transmission electron microscope images. Special thanks have to go to Geunsik Lee from Dongguk University and Elham Oleiki from Ulsan National Institute of Science and Technology who performed the density functional theory calculations.

Many thanks go to the people in the Quantum optoelectronic group for providing a friendly and joyful environment for discussion and work. Turning to the group that has offered such a stimulating and enriching working environment, I have genuinely appreciated and thoroughly enjoyed my time with every single member, both past and present and working alongside them has been a great pleasure. I would like to express my gratitude to the former PhD students Guanhua Ying and Vitaly Osokin for their invaluable guidance in helium handling and optical systems. They have imparted numerous useful skills that have greatly contributed to my knowledge and expertise in the lab.

Last but not least, I would like to express my sincere gratitude to my parents for their unwavering support during my decision to study abroad . Their only wish is that I continue to flourish academically and socially. I won the wormwood, the tree's heart, and the blessing of nourishment, and I can't give it back. My greatest hope will always be for you to be healthy and happy for eternity!

As this dissertation is nearly completed, I am filled with anticipation and excitement to take a step forward in my future work path.

List of Publications

- **Mutibah Alanazi**, Ashley Marshall, Shaoni Kar, Yincheng Liu, Jinwoo Kim, Henry J. Snaith, Robert A. Taylor, and Tristan Farrow, Stability of Mixed Lead Halide Perovskite Films Encapsulated in Cyclic Olefin Copolymer at Room and Cryogenic Temperatures, The Journal of Physical Chemistry Letters, 14(50), (2023). DOI:https://orcid.org/0000-0002-2393-9745.

- **Mutibah Alanazi**, Ashley R. Marshall1, Yincheng Liu1, Jinwoo Kim1, Shaoni Kar, Bernard Wenger , Henry J. Snaith, Robert A. Taylor, and Tristan Farrow, Inhibiting the Appearance of a Green Glow in Mixed Lead Halide Perovskite Nanocrystals for Pure Red Emission (Accepted to ACS Nano letters).

- Guanhua Ying, Elham Oleiki, Atanu Jana, **Mutibah Alanazi**, Vitaly Osokin, Sangeun Cho, Hyunsik Im, Robert A. Taylor, Youngsin Park and Geunsik Lee, Dramatic photoluminescence enhancement of graphene covered $CsPbBr_3$ quantum dots (submitted).

- Guanhua Ying, Tristan Farrow, Atanu Jana, Hanbo Shao, Vitaly Osokin, **Mutibah Alanazi**, Youngsin Park, and Robert A. Taylor, Resonantly pumped bright-triplet exciton lasing in caesium lead bromide perovskites, ACS Photonics 8, 2699, (2021). DOI:https://doi.org/10.1021/acsphotonics.1c00720.

Abstract

All-inorganic perovskites, including $CsPbI_3$, $CsPbBr_3$, and their mixed composition $CsPbI_{(1-x)}Br_x$ have drawn significant attention due to their thermal and chemical stability at operating conditions compared to organic-inorganic counterparts, allowing for diverse applications in wide-band light-emitting diodes (LEDs), lasers, and multijunction solar cells. However, single halide caesium perovskites of $CsPbI_3$ are typically unstable at room temperature, whereas orthorhombic $CsPbBr_3$ has a wider band gap (2.25 eV), and is consequently inappropriate for highly efficient applications. Indeed, the long-term stability of mixed halide perovskites under ambient conditions is still an issue affecting their progress and development for such applications, primarily attributable to halide segregation.

The initial part of this thesis focuses on lead mixed halide perovskites (LHPs) represented by $CsPbBrI_2$ thin films and tracks the microscopic processes occurring during halide segregation using combined spectroscopic measurements at room and cryogenic temperatures. A passivation strategy is evaluated to mitigate the halide migration of Br/I ions in the $CsPbBrI_2$ thin films by over-coating with cyclic olefin copolymer (COC). The results explain comprehensively the correlation between grain size, intensity dependencies, phase segregation, activation energy barrier, and their influence on photo-induced carrier lifetimes. Importantly, COC treatment increases the lifetime of charge carriers in mixed halide thin films, improving efficient charge transport in perovskite solar cell applications.

Following these promising results, the different roles of photooxidation on unbalanced iodine and bromine migrations between $CsPbI_2Br$ nanocrystals and $CsPbI_2Br$ thin films has been highlighted in the second part of this thesis. Cyclic olefin copolymer (COC) is a non-polar aliphatic chain, which is a relatively new type of polymer. It demonstrates excellent chemical resistance and acts as a barrier to other solvents, such as alcohols, and it is significantly resistant to damaging effects from acids and bases. Using a cyclic olefin copolymer (COC) matrix, the distinct photochemical decomposition processes between the pristine $CsPbI_2Br$ nanocrystals, $CsPbI_2Br$ thin films, and their encapsulated counterparts have been revealed. Upon continuous illumination, the $CsPbI_2Br$ nanocrystals tend to develop a green glow, and the emission shifts towards the blue end of the spectrum, with iodine ion agglomeration at deep red regions. Interestingly, the encapsulated $CsPbI_2Br$ nanocrystals show stable spectral emission at 615 nm, an increased halide ion migration barrier from E_a of 0.50 meV to 1.3 meV above 160 K and from 0.060 meV to 0.47 meV

below 160 K and reduced halide vacancy generation. The COC matrix hinders iodine oxidation or aggregation, prevents iodine gas leakage, inhibits a green glow which can help develop and produce a pure red light-emitting diode (red-LEDs).

Ultimately, the remaining experimental part of this thesis focuses on investigating the photoelectric properties of $CsPbBr_3$ as an example of a lead halide perovskite. The optical properties of graphene (Gr)-covered $CsPbBr_3$ quantum dots (QDs) are studied by micro-photoluminescence. Compared with bare $CsPbBr_3$ QDs, the PL intensity of the Gr-covered $CsPbBr_3$ QDs is dramatically enhanced by three orders of magnitude. Density functional theory (DFT) calculations reveal that contacting with Gr on the top side of the $CsPbBr_3$ surface generates interfacial electrostatic potential barriers which impede carrier leakage from the perovskite to the Gr layer under illumination conditions, resulting in an enhanced radiative recombination rate. In addition, $CsPbBr_3$ surface defect states are passivated by the Gr covering, suppressing the non-radiative recombination rate of photo-generated electrons and holes compared to the bare QDs. At the same time, Gr is n-doped and its plasmon mode is activated through resonant coupling with photo-generated excitons in the perovskite. The momentum mismatch between the Gr plasmon and propagating photons in free space can be resolved through plasmon scattering by Gr/$CsPbBr_3$ interface corrugations, leading to the observed super bright emission. Both experimental and theoretical investigations demonstrate the vital role of the Gr top contact in producing dramatic PL enhancement in the $CsPbBr_3$ QDs.

Contents

List of Figures

1 Introduction

Contents

1.1 Motivation and Aims

Halide perovskite (HP) materials have recently garnered significant global interest owing to their rapid advancements within the photovoltaic community. For single junction architectures, the photoconversion efficiencies (PCEs) of solar cells incorporating halide perovskites have rapidly increased from 3.8% [1] to over 25% [2], surpassing the maximum efficiencies of CdTe (22.1%) and CIGS (22.9%)[2]. Besides fabricating high-efficiency solar cells, HPs have been implemented in manufacturing photodetectors [3], light-emitting diodes (LEDs) [4, 5], light amplifiers[6, 7], and lasers [8, 9].

The exceptional diversity of halide perovskite materials drives these tremendous potentials for optoelectronic applications. For instance, all the structural elements of halide perovskites, indicated by the general chemical formula ABX_3, can be adjusted effortlessly depending upon the specific requirements of concrete optoelectronic applications. In particular, manipulating the cation's size can accomplish distinct dimensionalities

in halide perovskites (e.g. 3D, 2D, 1D and 0D). In addition to their versatility, low non-radiative recombination, even for polycrystalline samples resulting from beneficial physical defects [10], further contributes to the success of these materials. Moreover, halide perovskites can be synthesized via solution methods at low temperatures, thereby enabling the use of cost-effective fabrication techniques. Using solution processes allows halide perovskites to readily combine with other chemical materials.

However, incorporating mixed halides into these materials such as $CsPbBrI_2$ results in instability issues since they easily segregate into Br-rich and I-rich domains under continuous illumination; therefore, the long-term stability of perovskite solar cells and pure red light-emitting diodes (Pe-LEDs) is still challenging. Despite advances in synthesizing single halide perovskite $CsPbBr_3$ quantum dots (QDs), nanocrystals' heterostructures often show various intriguing functionalities for super-bright LEDs.

The migration and rearrangement of ions in halide perovskites, which lead to changes in their composition and properties, are multiphysics processes and, thereby, are difficult to characterise fully. Therefore, understanding the conditions and drivers behind such processes to control the properties of these materials better would allow the scientific community to produce highly stable optoelectronic applications and represent a technological advancement. In addition, halide perovskite nanocrystals are commonly passivated with different ligands or polymers, which are susceptible to facile desorption because of their feeble dynamic binding. Therefore, understanding surface-ligand interactions is also required to set criteria for strong ligand binding to the ionic perovskite surfaces in which strong ligand bonding is essential for nanocrystals to be economically feasible.

In this thesis, we will conduct an extensive investigation to gain a comprehensive understanding of the mechanisms mentioned above. We will then compare the extent to which surface passivation using the COC matrix enhances the photo-stability of lead mixed halide perovskites $CsPbBrI_2$ thin films with that of $CsPbI_2Br$ nanocrystals. Furthermore, we will explore how the optoelectronic properties of $CsPbBr_3$ quantum dots (QDs) can be modified by applying graphene surface decoration.

1.2 Thesis layout

The following chapter in this thesis will represent the theoretical concepts and the general background of all inorganic perovskite materials, including electronic structures and electronic and optical properties. The remainder of **Chapter 2** will then describe a brief introduction to the key concept of thermodynamic and kinetic models of the photoinduced phase segregations in all inorganic mixed Halide perovskite, such as miscibility gap, polaron-mediated lattice strain, the photocarrier energy model and the redox model, and then mitigation methods.

Chapter 3 presents a comprehensive overview of the laboratory techniques and essential methodology used in the experimental sections, which initially describes the different excitation sources such as lasers, followed by an overall description of micro-photoluminescence, time-resolved spectroscopy measurements, and 2D mapping carried out at both room and cryogenic temperatures.

Chapter 4 provides an experimental investigation of the possible microscopic processes occurring during halide segregation in $CsPbBrI_2$ films using combined spectroscopic measurements at room and cryogenic temperatures. The role of a passivation strategy for mitigating the halide migration of Br/I ions in the films by overcoating with cyclic olefin copolymer (COC) is shown in this chapter, along with a complex contribution between the stability of perovskites and grain size, the activation energy barrier of halide vacancies, non-linear intensity dependencies, and their corresponding charge carrier transport, which can provide a directional guide for further passivation strategies.

A comparative study contrasting the behavior of $CsPbI_2Br$ nanocrystals and $CsPbI_2Br$ thin films is covered in **Chapter 5**. The circumstances favouring phase separation over illumination time of $CsPbI_2Br$ nanocrystals will be demonstrated and addressed using the photo-oxidation and reduction reactions principle. The evidence in this chapter will show that in the absence of grain boundaries in the nanocrystals, halide sublimation will play an essential role because of large surface-to-volume ratios, which will predominantly occur in the outermost layer, leaving behind surfaces enriched with excess uncoordinated ions (Pb^{2+} and Cs^{2+}). The role of surface ligands in stabilising these ions, facilitating

the production of tribromide $CsPbBr_3$ and exhibiting a green glow is identified in detail. The usefulness of encapsulation using a COC matrix, the potential causes of a thermodynamically closed system and the energy exchange and chemical equilibrium concentrations of solid and gas products are explained in both nanocrystals and thin films. The long-term photochemical stability with pure colour emission in the 610 nm range of nanocrystals has been further identified at room temperature for highly stable pure red-light emitting diodes.

Chapter 6 covers a comparative analysis of the optical and electronic properties of bare $CsPbBr_3$ QDs and $CsPbBr_3$ QDs covered with graphene. The mechanism of the dramatic enhancement in the PL intensity Gr/$CsPbBr_3$ is thoroughly determined by using density functional theory (DFT) to analyze the electronic structure of the Gr/$CsPbBr_3$/SiO_2 heterosystem. The effect of interfacial electrostatic potential barriers on carrier transfer and recombination rates at the Gr/$CsPbBr_3$ interface in the Gr/$CsPbBr_3$/SiO2 hetero system is elucidated by DFT calculation. Through the use of TRPL measurements, the impact of graphene on surface defects in perovskites and its ability to inhibit non-radiative recombination of photo-generated charge carriers is also discussed. The role of resonant excitation of a Gr plasmon by perovskite photo-generated excitons, followed by its conversion to photons through interaction with Gr/$CsPbBr_3$ interface corrugations, is described in detail.

The conclusion of the thesis is presented in **Chapter 7**, which is an overview of current achievements involving tracking the mechanisms that induced halide segregation of $CsPbBrI_2$ thin films and nanocrystals, the mitigating of instability through the passivation of trap states using cyclic olefin copolymer (COC) treatment and tailoring the optoelectronic properties of $CsPbBr_3$ QDs using graphene. The outlook and future perspectives are highlighted for further developments in manufacturing longer-term stability for optoelectronic applications working under ambient conditions.

The appendix provides a manual for analyzing X-ray Diffraction Peaks (XDR) shown in **Chapter 3** using Fullprof software . This program is useful for XRD refinement to empirically estimate the threshold size of particles that induced halide separation using the Williamson-Hall and size-strain plot methods. It also briefly introduces the theory

of the optical frequency response of metals and the Drude model, which elucidates the surface plasmon effect shown in **Chapter 5**.

2
Background

Contents

2.1 Overview

In 1839 the German mineralogist Gustav Rose discovered of the mineral perovskite – calcium titanium oxide $CaTiO_3$ [11, 12]. The definition of perovskite has changed since Victor Goldschmidt's 1926 crystallographic paper revealing its crystal structure[13] and it currently refers to a class of minerals with a crystalline structure like that of $CaTiO_3$.

Magnesium silicate perovskite $MgSiO_3$ is the major material found in the earth, making it one of the most prevalent perovskite structures in nature. The chemical formula of these materials is ABX_3 in which both A and B are cations bounded by the X anion. These materials can be specified based on their anion nature in two main categories, i.e. oxide and halide perovskites [14]. Since 1956 the oxide perovskites have been extensively studied due to their ferroelectric properties, which are considered a desirable property for optoelectronic and light-conversion applications [11, 15]. In contrast to oxide perovskites, interest in halide perovskites has risen within the last few decades. Despite this late interest, the scientific research community have devoted their efforts to study these materials, which have revolutionised our understanding of this class of semiconductor materials [14]. The halide perovskites have been revealed as promising candidates for optoelectronic applications such as solar cells, light-emitting devices, lasers, and photodetectors due to their exceptional physical properties [14, 16]. This work will only focus on metal-halide perovskites and provide descriptions involving the structural, electronic, and optical properties of all-inorganic perovskite materials.

2.2 Electronic structure of all inorganic perovskite

2.2.1 The crystal structure

All perovskite materials have the same formula of ABX_3, in which X are anions of charge -1 and A cations of charge +1, which are usually larger than the B cations of charge +2 [17]. There are several ways to combine A, B, and X, although not all cation and anion mixtures have desirable properties. For example, the mixed halide perovskites materials studied in chapter 4 and 5 contain varying mixtures of iodine and bromine at the X site, and a mixture of Pb at the B site and Cs at the A site, as illustrated in Figure 2.1. The mixture of such cations and anions can lead to a variety of compositions of perovskite; however, this thesis will focus on a specific combination consisting of single and mixed halide-based all inorganic perovskites involving $CsPbBr_3$ and $CsPbI_2Br$ compositions.

The monovalent (A) cation can be formed from organic atoms consisting of several functional groups such as methylammonium (Ma^+, CH_3 NH_3^+) and formamidinium

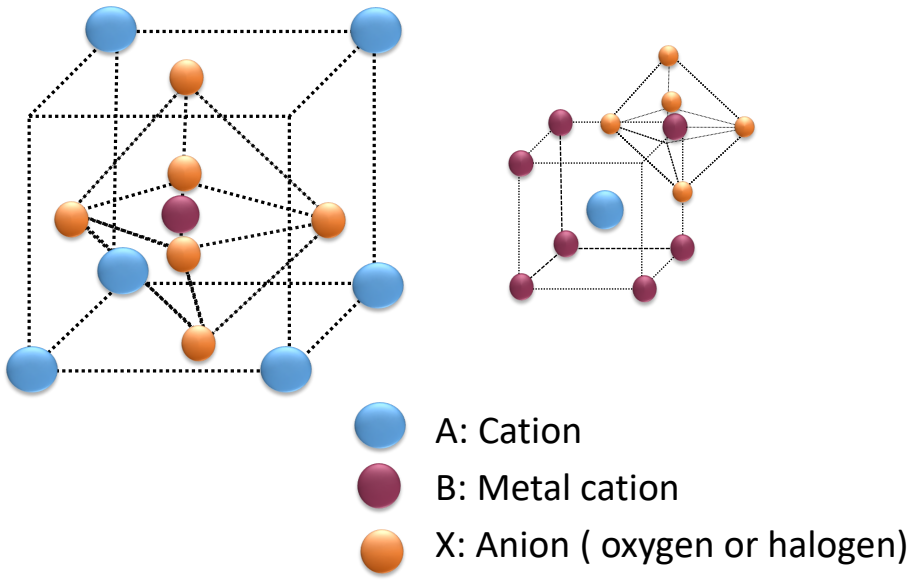

Figure 2.1: The typical crystal and lattice structures of perovskite with a general chemical formula ABX_3, in which X is oxygen or halogen.

(Fa^+, $C_2H_5\ NH_3^+$) or inorganic atoms like caesium (Cs^+) and rubidium (Rb^+). Based on the increased size of perovskite structure, the most popular choice for A^+ cation is among Cs^+, Ma^+ and Fa^+, respectively. However, the variation of both the size and coordination of A lead to distortion of the symmetry for the tetragonal or orthorhombic structure. For instance, Ma^+ is a relatively small organic cation with tetragonal unit cell resulting in a lack of symmetry and hence corresponding large bandgap of 1.51-1.55 eV. The hybridisation of larger organic cations like Fa^+ leads to cubic cell formation, which can highly enhance the cell symmetry, reducing the bandgap, consequently improving absorption at long-wavelengths (red-shift of the absorption spectrum). As a result, the different symmetry of the perovskite materials leads to various properties that in turn change the band gap and lead to phase transitions at certain temperatures [17, 18].

The (B) cations are mainly divalent metal ions such as (Pb^{2+}, Sn^{2+}, Eu^{2+} and Cu^{2+}) surrounding by six X atoms at the face centre which is commonly iodine (I^-), bromine (Br^-) or chlorine (Cl^-), forming a $[BX_6]^{4-}$ - 3D octahedral structure. According to the geomatics fitness and tolerance factor, only methylammonium, formamidinium and caesium (Cs^+) ions are stable in the 3D $[PbX_6]^{4-}$ structure. Thus, they can be

constructed in 2D, 1D, or 0D networks depending on whether the additional cation size is larger or smaller [18].

The (X) refers to halide ions including (Cl^-, Br^-, I^-) used as composite anions in the perovskite structure in which I^- is the most stable candidate among others. Due to the valence orbital shifts from 3p to 4p to 5p as the size of the halide anion increases, then I forms a stronger covalent connection with Pb^{2+}, as it is the periodic table's closest element to Pb.

2.2.2 Unit Cell and Symmetry

The unit cell of the perovskite structure has an A cation in the centre surrounded by eight connected octahedra of BX_6 groups. These materials favour cubic symmetry over other symmetry types owing to their strong ionic bonding and have a Pm3m space group known as the α - phase. The chemical bonds between B-X can specify the electronic properties of the perovskite materials as shown in Figure2.1. Although A-site cations do not directly contribute to the band structure, they significantly contribute to structural stability through charge compensation due to their electrostatic (van der Waals) interactions with the BX_6 octahedral framework [19]. Their electron affinities and ionisation energies do not exhibit a consistent pattern. However, the perovskite's optical properties can be altered due to any alteration in the size of the A component, which can either contract or expand the crystal lattice[20–22].

It is known that the perovskite structure is very flexible in that the A and B ions can be manipulated, leading to a large number of perovskite compounds or related systems. However, most perovskites can be easily distorted, therefore, do not have a better cubic structure. Three main factors identify the symmetry of the unit cell, which are responsible for the lattice distortion involving the size effects, the deviations from the ideal composition and the Jahn-Teller effect. The lattice distortion is rarely determined by a single effect for a specific perovskite compound. Geometrically, the unit cell axis, (a), in the ideal cubic structure is related to the ionic radii (r_A, r_B, and r_X) as illustrated in equation (2.1):

$$a = \sqrt{2}(r_A + r_X) = 2(r_B + r_X) \tag{2.1}$$

The proportion of both expressions for the cell length is known as Goldschmidt's tolerance factor t which estimates the degree of distortion and the symmetry. It is based on ionic radii, which implies that pure ionic bonds are assumed. It can be used to identify compounds with a high degree of ionic bonding as described in Equation (2.2).

$$t = \frac{r_A + r_X}{\sqrt{2}(r_B + r_X)} \tag{2.2}$$

For instance, Goldschmidt's tolerance factor in the ideal cubic perovskite is estimated to be $t = 1.00$, in which r_A = 1.44 Å, r_B = 0.605 Å, and r_X = 1.40 Å. For the range of the cubic symmetry in halide perovskites the tolerance factor is estimated to be in the range $0.89 < t < 1$ [13, 23].

However, If the A ion is small the t is less than the optimal value, (e.g., $t < 1$), the BX_6 octahedra will tilt to fill the available space. In this regard, the symmetry of the crystal structure will decrease when t values are reduced. To be more precise, with t less than 0.85, the B-X bond shrinks, requiring the A-X bonds to extend to maintain structural stability. This can happen by tilting the octahedra to lower the degree of symmetry. On the other hand, when t is more than 1.11, a higher symmetry is attained by having a substantially larger A site cation than the B anion compared to the cubic phase. As detailed, the tolerance factor t is not sufficient to predict the structure or the formation the perovskites. Since these materials are not truly ionic compounds and the t-value also depends on the ionic radii; thus, the tolerance factor is merely a rough approximation. Therefore, an additional factor is needed to describing the geometric structure of the octahedra. The ratio of the ionic radii of the B and X ions is known as the octahedral factor μ given by equation (2.3).

$$\mu = \frac{r_B}{r_X} \tag{2.3}$$

For instance, a stable structure in the halide-based perovskite only forms at an octahedral factor value higher than 0.442. Therefore, both tolerance and octahedral factors determine the degree of cubic symmetry and structure stability for perovskite compositions. The combination of the tolerance and the octahedral factors able to study the perovskite formability and investigating the regularities of formability for the general and cubic perovskite [24].

2.2.3 Electronic properties

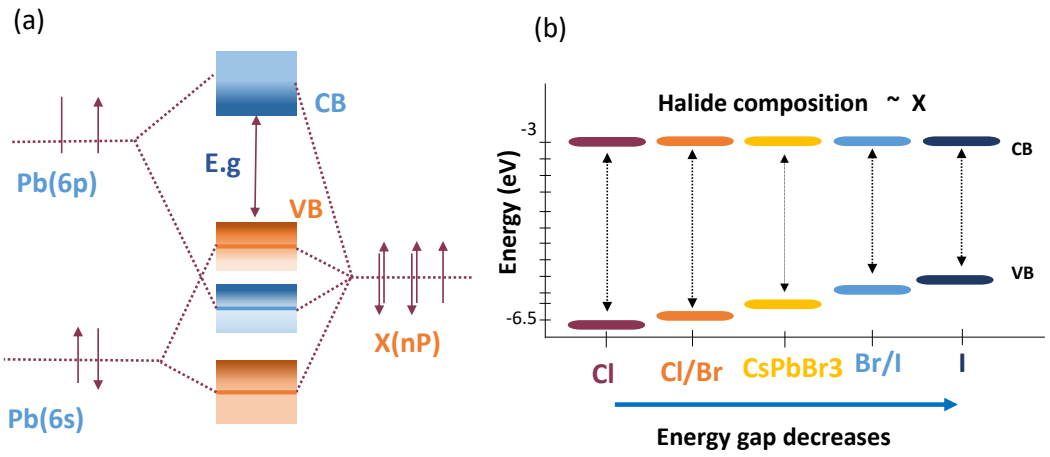

Figure 2.2: (a) Schematic diagram illustrating the synthesis of valance band (VB) and conduction band (CB) in the bonding and antibonding orbitals of $APbX_3$. (b) The band edge energies of $CsPbX_3$ nanocrystals with varying halide compositions and an average size of 11 nm (ultraviolet photoemission spectroscopy)

Perovskite optical transitions and charge transfer depend on their electrical characteristics. In typical inorganic perovskites, the antibonding mixing of the halide p orbitals and the dominating Pb 6p orbital determines the conduction band [25, 26]. On the other hand, the p orbitals of the halide ions and the Pb 6s orbital both contribute to the valence bands, while the p orbitals of the halides are the main contributors. The electronic structures in all-inorganic perovskites are illustrated in Figures 2.2 (a)-(b). The Cs cations in inorganic perovskites have a negligible effect on the electronic states, meaning they have no essential effect on the band-gaps. All-inorganic perovskites also exhibit direct bandgaps suggesting that their light-response behavior is promising for opto-electronic applications [27]. However, the band-gaps in perovskites may become indirect as a result of the Rashba effect. Like hybrid perovskites, Marrionnier et al. discovered that the inorganic perovskite $CsPbI_3$ has an indirect band gap due to the Rashba effect [28, 29]. Although the Cs cation has a minor effect on the electronic structure near the band edge, it indirectly affects the excitation and recombination of electrons and holes due to the

Compound	**Phase**	E_g (meV)	R^* (meV)	$\mu(m_0)$	ε(eff)
$CsPbI_3$	cubic	1.7723	15 ± 1	0.114 ± 0.01	10
$CsPbI_2Br$	cubic	1.906	22 ± 3	$0.124 \pm 0{,}02$	8.6
$CsPbBr_3$	orthorhombic	2.342	33 ± 1	0.126 ± 0.01	7.3

Table 2.1: The values of the energy gap E_g, the exciton binding energy R^*, the exciton reduced mass $\mu(m_0)$ and the dielectric constant ε(eff) for $CsPbBr_3$, $CsPbI_2Br$ and $CsPbI_3$ compounds were estimated in the previous study [31]

tilting of PbX_6 octahedra. Furthermore, the high carrier mobilities in the perovskite materials are attributed to the effective masses of electrons and holes. The energy levels of the halide p orbitals decrease as the halide composition shifts from iodide to chloride, which causes the valence band to shift towards higher positive potentials. The calculated valence band positions of $CsPbBr_{1.5}I_{1.5}$, $CsPbBr_3$, and $CsPbBr_{1.5}Cl_{1.5}$ are 6.1, 6.5, and 6.5 eV, and the conduction bands are 4.3, 4.15, and 3.8 eV, respectively [30]. The band gap variation with halide compositions changes is one significant aspect influencing the halide segregation phenomenon which will be discussed in section 4.

The effective mass and exciton binding energies were calculated and reported by analyzing the magnetic field dependence of hydrogenic and free carrier transitions [31]. The exciton binding energy of $CsPbBr_xI_{3-x}$ perovskites is increased with an increase in the Br concentration. $CsPbI_3$ has an exciton binding of a energy of 15.1 meV, which is comparable to that of $MAPbI_3$ at 16.2 meV, while an exciton energy increases to 22.3 meV for $CsPbI_2Br$ and 33 meV for $CsPbBr_3$. The values of effective mass, effective dielectric constant, and exciton binding energy for Cs-based inorganic perovskites with various bandgaps (halide compositions) in Table 2.1. The carrier effective mass often rises with the bandgap, suggesting that the halide anions have a major impact on the electrical characteristics of perovskites.

2.2.4 Quantum confinement effect

For mixed-halide perovskite nanocrystals PNCs, the quantum confinement effect happens when the perovskite crystal size is smaller than the Bohr radius[27, 32, 33]. Perovskite nanocrystals (PNCs) exhibit superior optical and electrical properties over bulk films or single crystals because of their high surface-volume ratio, low trap densities, and

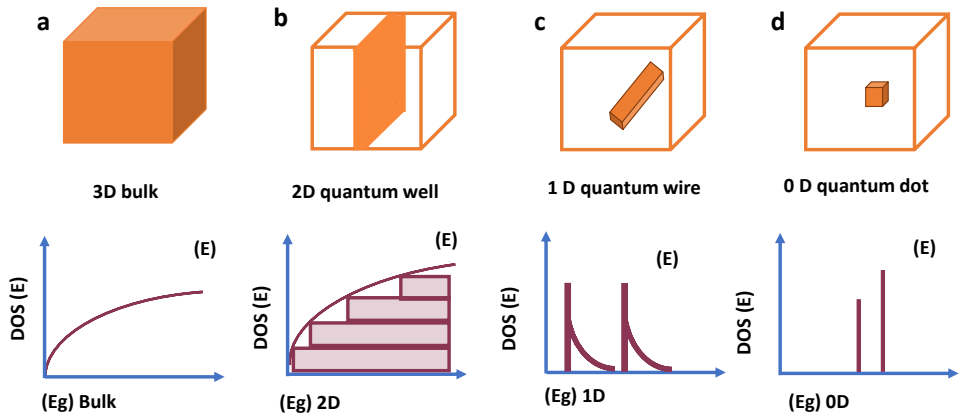

Figure 2.3: The schematic illustration represents a three-dimensional (3D) bulk semiconductor and its corresponding two-, one-, and zero-dimensional (0D) quantum nanostructures. The density of states DOS E between CB and VB bands are represented as a function of the energy, assuming the infinite confinement potentials and an effective mass model for both bands. The quantum confinement can lead to an increase in the electronic band gap compared to the bulk material. The 3D DOS is also reconstituted by combining 2D DOS associating with electrical sub-bands in the VB and CB.

flexible functionalisation. Examining the electron-hole pair provides a deeper physical perspective on the quantum confinement effect. An excited electron in the CB is bound to the hole in the VB due to Coulomb interactions, generating an electron-hole pair (exciton), occupying a specific 'space'. This space can be described by the exciton Bohr radius a_0, as is illustrated in equation 2.4. [34, 35].

$$a_0 = \frac{\hbar^2}{e^2}\varepsilon\left[\frac{1}{(m_e^*)} + \frac{1}{(m_h^*)}\right] \tag{2.4}$$

The exciton Bohr radius a_0 depends upon the effective masses of both electron and the hole in which depend on the material they are in. Consequently, the a_0 depends on the material; for example, the exciton Bohr radius of $CsPbCl_3$, $CsPbBr_3$ and $CsPbI_3$ is 5, 7 and 12 nm, respectively [27]. First, the exciton can move freely when the size of the mixed halide perovskite is larger than the Bohr radius (a_0). Second, if the size of the perovskite nanocrystals (PNCs) is equal to a_0, the exciton will be spatially limited since it can no longer go freely through the material. Third, when the size of the PNCs decreases further to be smaller than a_0, the exciton will be confined, and its energy

is increased. The bandgap of a nanocrystals can be explained by the Brus Equation [36] as shown in equation 2.5:

$$E_{\mathrm{QD}} = E_{\mathrm{gap}} + \frac{h^2}{8r^2}\left[\frac{1}{(m_e^*)} + \frac{1}{(m_h^*)}\right] \tag{2.5}$$

In this case, the band gap increases as the nanocrystal size decreases. Due to the exciton Bohr radius relying on the perovskite composition, the degree of quantum confinement of a specific nanocrystal size depends on its composition. Quantum confinement effects, for example, will not be seen in a 20 nm $CsPbBr_3$ PNCs (a_0 = 5 nm) because of its size being much larger than its exciton Bohr radius.

This scenario explains the quantum confinement effects for PNCs in which three dimensions are all confined, known as quantum dots. The sizes of PNCs can be synthesized in different shapes which are classified by their dimensionality. For example, although "three-dimensional" (3D) nanocrystals have features similar to their bulk counterparts, their dimensions do not show quantum confinement. Two-dimensional (2D) nanosheets (NSs) or quantum wells are examples of two-dimensional 2D PNCs that exhibit quantum confinement in only one dimension. One-dimensional (1D) nanowires are elongated nanowires with two dimensions showing quantum confinement. Quantum confinement is most pronounced in zero-dimensional (0D) systems, like clusters or QDs, where all three dimensions display quantum confinement. The dimensional changes of perovskite sizes have a strong effect on the DOS, in which the bands of a bulk perovskites are square root dependent of their energy ($E^{\frac{1}{2}}$), as illustrates in Figure 2.3 (a-d).

Although excitons are confined in the lateral dimension, they move in two dimensions in a 2D quantum well, and the density of states (DOS) has a stepwise structure due to the quantization of energy levels in the confined dimension, which is usually independent of the energy (E_0 = constant). This structure means that whilst all energies are available, the DOS only increases in quantifiable stages at the onset of new subbands. The DOS within each subband remains constant, reflecting the unique electronic properties of 2D systems. This behaviour is essential for understanding quantum wells' electronic and optical properties and designing devices based on these materials.

In a quantum wire, the exciton can move along the wire, leading to a DOS with an inverse square energy dependence ($E^{-\frac{1}{2}}$). Here, the DOS only increase to quantifiable levels whereas it decreases rabidly between each quantifiable step. Finally, 0D quantum dots show a DOS where states are only permitted at specific energies. It is worth noting that perovskite NCs cannot simply be described by the DOS of 2D, 1D or 0D states due to their various sizes and shapes. For example, $CsPbBr_3$ nanoplatelets with an exciton Bohr radius of 7 nm were synthesized with dimensions of $20 \times 5 \times 2$ nm. As a result, one dimension in these $CsPbBr_3$ nanoplatelets has bulk characteristics and will not show quantum confinement. One dimension shows weakly confined excitons in which the bandgap only exhibits a small increase. One dimension exhibits a very strong quantum confinement (strongly confined excitons with very discrete states and a large increase in bandgap). This thus results in a quasi-2D model.

2.3 Optical properties of all inorganic mixed Halide perovskite

2.3.1 Bandgap tunability and stability

All-inorganic perovskites often have multiple structural and phase transitions triggered by external stimuli as shown in Figure 2.4. The cubic phase α-$CsPbI_3$ with a bandgap of 1.73 eV is an excellent material for the absorber layer in perovskite solar cells [37]. Nevertheless, the α-$CsPbI_3$ is metastable at ambient temperature and stability can only be obtained beyond 315°C. It has been shown that, at the expense of a larger bandgap, the partial replacement of I^- by Br^- lowers the phase transition temperature of $CsPbI_3$ and stabilizes the cubic phase. The $CsPbI_3$ transforms to tetragonal (β-$CsPbI_3$) at a temperature of 281°C whereas it converts to orthorhombic (γ-$CsPbI_3$) at a temperature above 184°C. The γ-$CsPbI_3$ changes into the non-perovskite σ $CsPbI_3$ phase after being exposed to ambient air[37]. It also can be converted back to the cubic phase by heating it over 315°C. The yellow σ-$CsPbI_3$ phase can be detrimental to optoelectronic applications as a result of a large bandgap (2.83 eV) and low electronic transport properties. The perovskite structures of other halide compositions, including $CsPbBr_3$ and $CsPbCl_3$,

undergo phase transitions from cubic to tetragonal at 130° and 47°C, while they transform from tetragonal to orthorhombic at 88°C and 42°C, respectively [38, 39]. Moreover, the bandgap in perovskites can be tuned across the whole visible spectrum by mixing halide ions. These mixtures not only help to stabilize the cubic phase at operational temperatures but also can tune the bandgap, facilitating their applications as top layer in tandem solar cells [27, 40, 41].

Furthermore, there are significant similarities between the physical properties of inorganic halide perovskites and their counterparts in the organic–inorganic hybrid state. For instance, using density functional theory calculations (DFT) Draguta et al.found that replacing the organic cation with inorganic Cs does not significantly alter the optoelectronic characteristics of hybrid perovskites [40]. The real component of the dielectric function, the absorption coefficient, and the reflectivity all show a similar trend between $MAPbI_3$ and $CsPbI_3$. Using low-temperature magneto transmission spectroscopy, Nicholas et al. revealed for the first time the essential properties of all-inorganic perovskites, including their reduced mass, phase transition, and exciton binding energy [31, 42]. The bandgap varies in all-inorganic perovskites at various temperatures in which the bandgap energy red shifts when more I^- was substituted for Br^-, which matched the experimental finding of a smaller bandgap when a heavier halide was substituted [31, 42].

2.3.2 Phase segregation in all inorganic mixed Halide perovskites

It is indicated that a straightforward approach for adjusting the bandgap of perovskite materials across the whole visible spectrum is the halide-mixing method [45]. However, these materials undergo halide phase segregation into I-rich and Br-rich domains under continuous illumination, deterring the progress in optoelectronic devices based on such materials. Several mechanisms have been suggested that can be a reason for halide segregation resulting from ion migration in perovskite thin-films, involving chemical gradient, thermal gradient, applied electric field and light-induced photo-excitation. The first observations of such a phenomenon was shown by Hoke et al. in $MAPb(I_{1-x}Br_x)_3$. They demonstrated that a reversible emission red-shift under continuous illumination caused the formation of I-rich domains within pristine mixed-halide films [46]. The

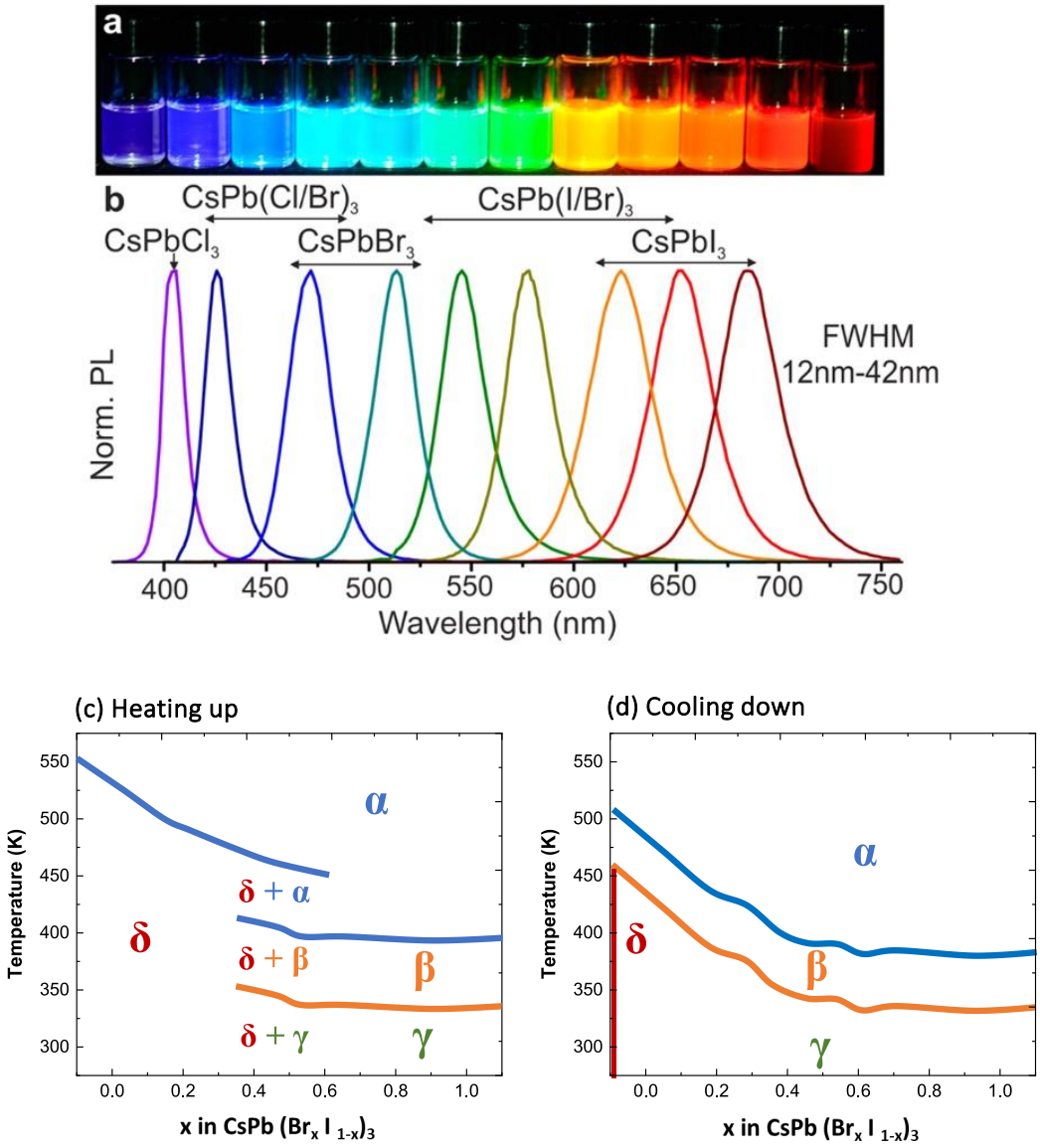

Figure 2.4: Bandgap tuning for different halide composition of $CsPbB_x$ perovskites. Copyright, 2015, American Chemical Society in reference [27] (a) perovskite solutions diluted in toluene exposed to UV lamp of 365 nm; (b) PL spectra for perovskite solution. Structure transition of all inorganic mixed halide perovskites at different temperatures (c) heating up (d) cooling down.

Material	Room Temperature phase	Other phase	Notes
$CsPbBr_3$	Black phase E_g = 2.25 eV [43]	$T \geq 88^\circ$C Tetragonal phase, $T \geq 130^\circ$C Orange phase [43]	While the room temperature phase is stable, the large band gap makes it unsuitable for use as a PV absorber.
$CsPbI_2Br$	Brown phase E_g = 1.92 eV	Yellow phase E_g = 2.85 eV	The optimal equilibrium between ambient temperature stability and band gap.
$CsPbI_3$	Yellow phase E_g = 2.85 eV [44]	$T \geq 310^\circ$C Black phase at room temperature E_g = 1.73 eV [44]	It has a band gap that is adequate for a PV application; however, it is a metastable phase at room temperature.

Table 2.2: Summary of the main phase, band gap of the most used compounds of the $CsPbI_{3-x}Br_x$ mixed halide perovskites

optoelectronic properties (e.g. bandgap) differ from its pristine mixed-halide phase. Such a demixing phase can be detrimental to photovoltaics and light-emitting applications. This is because the emission wavelengths deviate from the pristine state, and consequently lead to degradation of the perovskite phase [47]. The intrinsic property of halide ion movement in the perovskite materials can be described by diffusion, in which ions move from site to site through lattice defects. The diffusion coefficient (D_{ion}) can be expressed by Arrhenius relationship:

$$D_{\text{ion}} = D_0 \exp \frac{-\Delta(E_{\text{a,ion}})}{k_B T} \tag{2.6}$$

where D_0 is a temperature-independent pre-factor, Δ ($E_{\text{a,ion}}$), is the activation energy for diffusion, T is temperature and k_B is the Boltzmann constant. Although, this equation generally describes mobile ion diffusion in materials, the term ion migration in the halide phase segregation case is used to describe halide ion movement instead of diffusion. These

halide ions have a preferable path, otherwise halide movement will not result in separate halide rich domains. Therefore, this effect can be described using the ion flux expression.

$$J_{\text{ion}} = -D_{\text{ion}} \frac{\partial C_{\text{ion}}}{\partial x} \tag{2.7}$$

where C_{ion} is the ion the concentration of ion and x is the distance for a single hopping process. Hence, ion migration is dependent on both activation energy (E_{a}) and the concentration of available lattice defects C_{ion}. It is well-known that ion migration in perovskites results from the existence of point defects including ion vacancies, interstitial sites and anti-sites in the crystal lattice [48]. Among these defects, the most common defects in mixed halide perovskite materials are halide vacancies due to them having the lowest formation energies. According to theoretical and experimental results on ionic conductivity measurements the activation energy (E_{a}) for ion vacancies is given by $V_{\text{Cl}^-} < V_{\text{Br}^-} < V_{\text{I}^-} < V_{\text{MA}^+} < V_{\text{FA}^+} < V_{\text{Cs}^+} < V_{\text{Pb}^{2+}}$ [49]. It has been suggested that halide vacancies V_{X^-} are the essential reason for ion migration in such materials. Figure 2.5 provides an example of halide vacancy-mediated phase segregation from an I/Br mixed-phase under illumination. The investigations on $\text{MAPb}(\text{I}_{0.6}\text{Br}_{0.4})_3$ temperature-dependent emission prove this suggestion. These investigations yield the estimated phase segregation activation energy $E_{\text{a}} = 0.27\,\text{eV}$, near the theoretical E_{a} values for V_X given in [46]. Barket et al. indicated that the halide vacancy densities are closely attributed to phase segregation kinetics in demonstrated in $\text{MAPb}(\text{I}_{1-x}\text{Br}_x)_3$ films. The presence of halide vacancies triggers a much faster Br^- migration (within 3 ps) and therefore reduces activation energy for migration as compared to a perfect saturation of undercoordinated PbX_6 octahedral systems with I/Br mixed halides [50–52]. Owing to halide vacancies providing low-energy migration pathways, the mixed-halide systems typically have lower thresholds for halide segregation [52]. This section will demonstrate the underlying mechanism of halide phase segregation based on three theoretical models and will discuss methods to mitigate this effect.

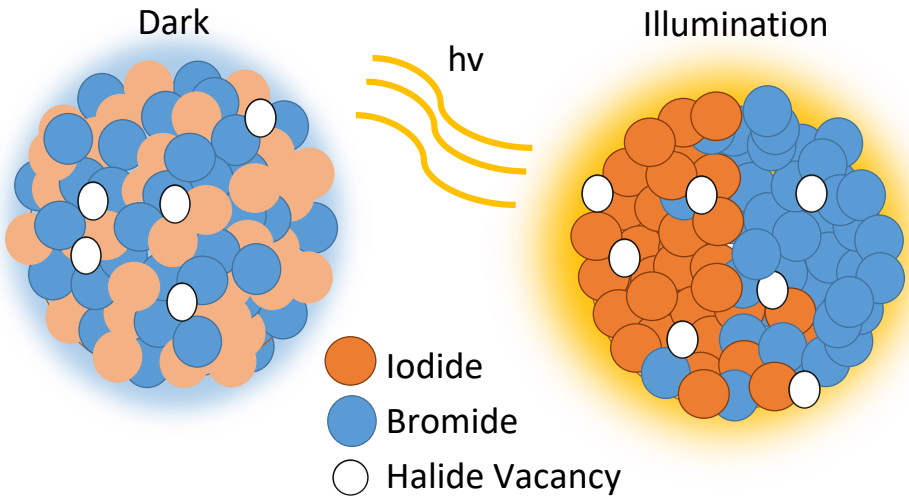

Figure 2.5: Illustration of the kinetic dynamics of anion photosegregation mediated by halide vacancies in mixed I/Br perovskites.

2.4 Phase segregation models

The driving force induces phase segregation in mixed halide perovskites, resulting in the system favouring lower total-free energy. The total free energy can be indicated by the equation $\Delta G = \Delta H - T\Delta S$, where ΔH represents enthalpy and ΔS refers to the entropy of the system [53]. Specifically, ΔS can be interpreted as the degree of distortion in the system, meaning that mixed halides are a spontaneous process in which the systems tend to reduce their ΔG by increasing their ΔS term for thermodynamic stabilization. Based on a thermodynamic model using DFT calculations, it has been suggested that entropy dominates formation free energies and can determine the composition variation in each phase domain [53]. For example, when MHPs like $CsPbBr_xI_{1-x}$ are exposed to continuous irradiation with excitation energy above the bandgap, it leads to the separation of halide ions. This separation results in the formation of domains that are rich in bromide ions (Br-rich) and iodide ions (I-rich), respectively [46, 54, 55]. The formation of two segregated phases (Br- and I-rich domains) and the decrease of mixed halide phases were confirmed by carrying out in-situ time-resolved absorption or emission measurements[54, 56]. It is intriguing that the reverse process of dark remixing can occur easily because of entropic stabilization when the light irradiation mechanism is halted [54, 57]. The dominance of configurational entropy of mixing over the penalty of enthalpy of mixing,

due to lattice strain, is considered when evaluating the change in free energy throughout the process of halide ion remixing. This implies that the segregated phases tend to revert to the original mixed halide composition in the absence of light, facilitated by the movement of halide ions through thermal assistance. The relative concentration of halide ion defects is a critical factor in determining the halide ion mobility during the reversible halide ion segregation and dark remixing. In the perovskite community, the preservation of the original mixed halide phase stability and the suppression of halide ion migration continue to be major concerns. The underlying processes of halide ion segregation have been thoroughly investigated in terms of the thermodynamics and kinetics of halide ion migration. In perovskite lattices, carrier generation induces halide ion migration, which results in the accumulation of electrons and holes at lower bandgap sites. The consequence of this is the alteration of MHP colour purity in PeLEDs and the reduction of power conversion efficiency in PSC due to undesired radiative recombination [57–59].

On the other hand, the entropy can be enhanced with elevated temperature, which drives the mixing of halide phases. Elmelund et al. also showed that mixed halide perovskites result in quick exchange between halide ions, driven by entropy of mixing phases. In addition, the rate of mixing increases with temperature evidencing a thermally activated process [54, 60]. It is worth noting that the halide phase segregation processes can be reversed in the dark where segregated halide phases can recover to their original optical properties, confirming the mobility of halide ions in opposite pathways [35]. Therefore, ΔS dominates in dark conditions and consequently drives the segregated domains back to the original mixed composition to favour a lower Gibbs free energy. Furthermore, Elmelund et al. observed that the recovery time is reduced from 14 hours to just 20 mins after increasing temperature from room temperature to 80°C. Since the threshold of the excitation intensity for photo-induced segregation is enhanced with increasing temperature, evidencing the interplay between thermal entropy (promotes mixing) and photo-excitation (promotes demixing) [39, 61]. Overall, both the entropy and thermal activation of the mixing process are two initial driving forces for a homogeneity of halide mixing. As a result phase segregation can occur when the demixing force overcomes the mixing force. This section examines the literature's proposed mechanisms

for photoinduced phase separation, which are classified as thermodynamic, polaron/strain, carrier gradient/carrier entrapment, and redox models.

2.4.1 Miscibility Gap

The thermodynamic model can help interpret the miscibility and stability of the mixed-halide phase by determining the Gibbs free energy ΔG changes with various halide mixing compositions at specific temperatures. When ΔG is negative, the homogeneous phase in perovskite systems tends to be stable. A thermodynamic model for such phenomena was first proposed by Walsh et al. using density functional theory (DFT) to calculate the Helmholtz free energy variation for $MAPb(Br_xI_{1-x})_3$ at different temperatures from 200 to 500 K. As shown in Figure 2.6, the perovskite phase in the $0.2 < x < 0.7$ range of compositions is metastable at room temperature, whilst the thermodynamically stable phase can only be achieved outside this range. Once the mixed halide perovskites are subject to sufficient energy (e.g. photo-excitation intensity) to kinetically overcome their metastable mixed-halide state, the material is more likely to segregate phase into I-rich and Br-rich domains [46]. In other words, poor miscibility of mixed halides leads to a high compositional disorder system indicated by thermodynamics. Therefore, it is energetically unfavourable for a mixed-halide phase, and ΔG is more likely to act as the driving force for halide segregation [46]. The spinodal decomposition hypothesis predicts that after the separation of the I-rich and Br-rich phases, two phases will be closer to thermodynamic equilibrium. However, this model is unable to explain the reversibility upon the removal of light-excitation, as observed in previous studies [40, 46, 54, 62].

Based on this model, Elmelund et al. suggested a bi-directional movement of halide ions governed by the competition between mixing and de-mixing activation energies. The lower activation energy of light-induced segregation (E_a = 28.9 kJ/mol) will overcome a larger activation barrier of the homogeneous mixing phase in the dark (53.5 kJ/mol), leading to halide ion migration under photoexcitation [46]. Elmelund et al. also suggested the segregation process can compete with entropically driven remixing under illumination, in which the excitation intensity threshold for photo-induced halide segregation increase with higher temperature. In addition, thermal energy assists the defect-mediated hopping

process, which lead to faster segregation kinetics by increasing the temperatures. The continuous growth of halide-rich domains can be explained by the energy band offset model as the kinetic energy barrier is overcome and the system favours a segregated phase. Draguta et al. also observed a non-linear intensity dependency of phase segregation process [40, 63]. The conduction band edges become isoenergetic after mixed halide films are segregated into I-rich and Br-rich phases. At the same time, valance band edges shift to a lower energy level (for I-rich phases) and a higher energy level (for Br-rich phases). Hence, this energy offset provides a driving force for demixing halides to balance the entropic tendency for halide mixing.

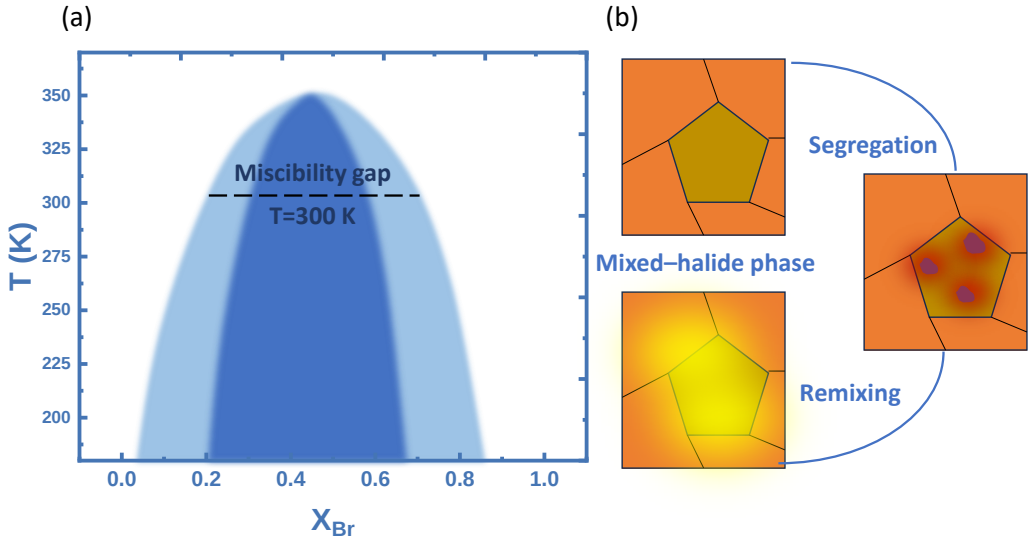

Figure 2.6: Schematic illustration of the thermodynamic model for phase segregation. (a) Predicted phase diagram of the mixed halide perovskites. The blue and dark blue lines are the binodal (coexistence) and spinodal (segregation) lines, respectively. The dashed line represents the miscibility gap at room temperature. The remaining region shows a thermodynamically stable solid solution. (b) Diagram illustrating the relationship between the processes of segregation and remixing under thermal energy and radiation, respectively.

2.4.2 Polaron-Mediated Lattice Strain

Due to the soft and ionic lattice of halide perovskites between cation and the PbI_6 octahedra, a polaron-induced lattice strain model was proposed to explain the driving force of ion migration and halide demixing phases as shown in Figure2.7. Bischak et al. have proposed that localized strain can be formed once a single photoexcited charge

carrier is coupled with such soft lattices, inducing halide ion migration[62]. In other words, both local lattice strain and deformation originating from the interaction between localized charge carrier with surrounding lattice by electron-phonon coupling can play an essential role as the driving force for ion migration and halide demixing [62]. According to thermodynamic calculations, polaron formation driven by optical illumination increases the total free energy compared to the counterpart ground state in the dark, resulting in an increase in external lattice strain energy. Thus, a thermodynamic explanation based upon the increased local lattice strain energy as a result of the polaron suggested that ion migration and the halide ion segregation to form Br-rich and I-rich domains occur to release the excessive strain energy. However, this model does consider charge carrier concentration, minimum threshold excitation intensity, and the concentration halide ion defects. This is taken into consideration in theories that rely on the discrepancy between the band-gap of the initial mixed phase and the light-induced I-rich regions [62, 64].

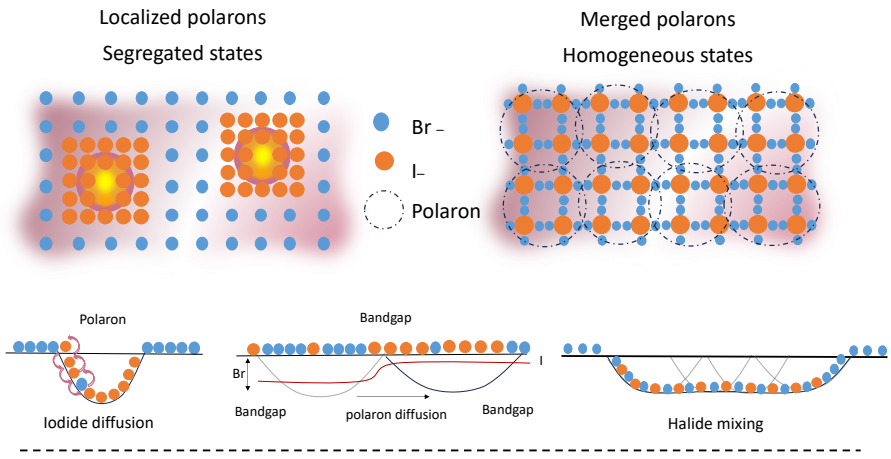

Figure 2.7: A schematic illustration depicts the halide ion distributions in a mixed halide perovskite lattice in response to low (left) and high carrier densities (right). The suggested lattice model relies on three driving mechanisms: Iodide diffusion along polaron strain gradients.Polaron diffusion along iodide concentration gradients. Halide mixing in the absence of significant strain gradients [65]

2.4.3 Photocarrier Energy Model (Band Gap Difference)

As previously mentioned, ion migration happens due to point defects in perovskites [50, 66–70]. The internal gradient in carrier concentration can act as the driving force for directional migration, potentially contributing to phase segregation. In other words, the photoexcited charge carrier can rearrange ion distribution within perovskites. The phase segregation process includes generating charge carriers, diffusion, accumulation, and carrier recombination at the I-rich domain. Specifically, the bandgap difference between mixed and segregated phases that depends on the carrier concentration caused the driving force of halide segregation, enhancing the free energy in the excited states of the mixed halide. Like strain models, the increased free energy resulting from the bandgap energy offset minimises halide ion segregation. In particular, the bandgap difference mainly resulted from the difference between the isoenergetic conduction band edge in the Pb 6p orbitals and the valence band edge difference, indicating the role of holes. In addition, the energy gradient in the segregated phase can drive the demixing of halides by funnelling and accumulating the photoexcited hole to the I-rich phase (the narrowest bandgap). Kuno et al [69] indicated the vital role of incident light intensity threshold in the photocarrier concentration in the halide ion segregation. They further confirmed that photo-induced phase segregation requires minimal photon energy to overcome the activation barrier of segregation. According to a unified thermodynamic theory suggested for light-induced halide segregation, the free energy of mixed halides is more likely to be reduced through a photocarrier funnelling to I-rich phases when subjected to continuous illumination.

2.4.4 Redox Model

Recently, Samu et al. have illustrated the crucial role that holes play in the instability of iodide in the mixed halide phases, which in turn leads to halide ion segregation [71]. They also confirm that the halide ion segregation is caused by hole trapping and accumulation within the mixed halide phase. Ultrafast pump-probe transient spectroscopic measurements also confirm that halide ion migration is caused by photooxidation of (I^- to I^*). These instabilities of iodide can migrate into interstitial defects by creating halide vacancies. Similarly, Herz and colleagues also have revealed the electron trapping and

hole localization in the mixed halide phases are responsible for the segregation [58]. Kerner and co-workers highlighted the role of photo electrochemistry mechanism in halide phase segregation in which iodide oxidation induced by photogenerated holes can initiate the halide demixing process [72]. They suggested that any factor causing iodide oxidation rate discrepancy, such as defects, heterogeneity, film thickness, promote halide segregation by creating local gradients in the concentration of oxidised halide species. Furthermore, all oxidised halide species are much more mobile than halide ions at the lattice sites. For example, Figure 2.8 represents their electrochemical viewpoint, showing how iodide's preferred redox causes halide segregation in MHPs and the routes used by the oxidised species during their travel through perovskite films. In this case, the valence band maximum (VBM) of the perovskites have to be sufficiently deep for the photogenerated holes, to consequently activate iodide oxidation processes. This means that it requires a threshold bromide concentration for the perovskite compositions, which could explain why the halide segregation only occur within particular x value ranges [73–75]. Furthermore, it is believed that vapour phase (I_2 vapour) transport is a significant mass transport form of the oxidised iodine species in the perovskites. This helps to explain why, under vacuum conditions, the reversibility of halide segregation is compromised, possibly as a result of the loss of an iodide component [76, 77]. Taken together, the oxidation of I^- to neutral I^* species is triggered by the localization of holes in the mixed halide lattice. These species are easily captured into iodide interstitial sites, promoting further the formation of iodide vacancies. According to the photo-carrier model, halide ion segregation results from hole accumulation at the I-rich domain caused by a favourable energy gradient in the segregated phases. To fully understand the halide segregation all factors including the lattice strain (after distortion), iodide oxidation by holes and its migration to interstitial, halide vacancy creation, halide ion (or halide vacancy) migration, and final segregation are need to be considered [78–80].

2.5 Mitigation methods

In mixed halide perovskites, phase segregation can be suppressed using three general methods. It is shown that compositional adjustment stabilises the perovskite lattice [81].

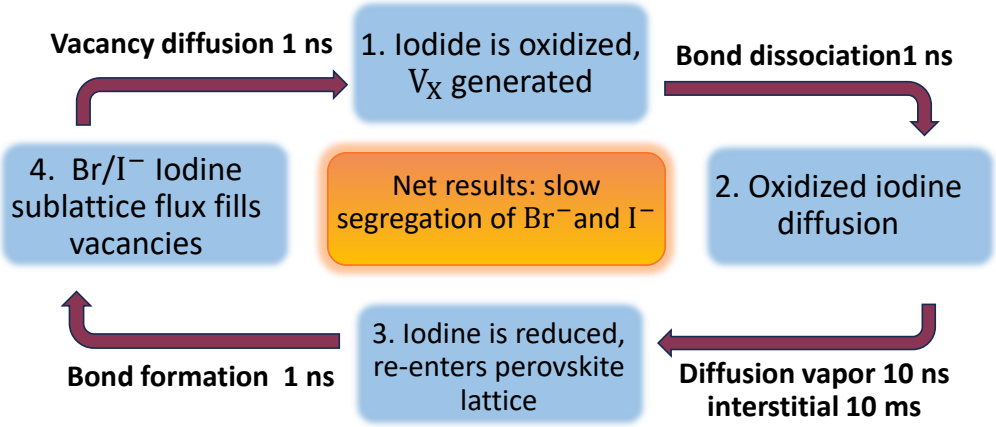

Figure 2.8: A schematic representation of the sequence of microscopic occurrences, encompassing time intervals, that a halide ion goes through while undergoing its redistribution driven by oxidation

The enhanced crystallinity through morphological engineering has shown also to be more promising by suppressing grain boundaries [82]. Moreover, the passivation of trap states inhibits phase segregation through eliminating ion vacancies [68, 83]. Although these strategies have been reported in hybrid perovskites, they are also applicable in the case of inorganic perovskites. It is also worth noting that replacing organic cation with inorganic cation has been considered as one strategy for inhibiting the phase segregation. Therefore, mitigation strategies ought to focus on the increase of the energy barrier for ion migration, limiting lattice distortion and electron-phonon coupling (polaron formation) and reducing the trap states densities. The affinity of mixed-halide ions is increased with temperature, leading to better photostability at a higher temperature [62]. However, Barker et al. demonstrated that high temperatures can trigger a fast halide segregation process [73, 84]. It is evident that the controversy surrounding temperature-dependent entropy mixing and ionic transport is still open and requires further investigation. Since the more solid lattice structure of inorganic perovskites lowers the lattice distortion, Ginsberg and colleagues discovered restricted electron-phonon interaction when the MA is substituted by Cs [85]. When MA is largely substituted by Cs, other researchers similarly found that the bromide concentrations unstable phase segregation range narrowed [42, 57]. Enhancing

crystallinity is an additional strategy for inhibiting phase segregation in mixed-halide perovskites. Several groups have demonstrated that perovskite films with bigger grains have superior durability against phase segregation. The stability enhancement results from lower grain boundary densities, known to be the sites of halide ion accumulation. The ionic mobility of halide perovskite is comparatively larger along the grain boundaries than inside the bulk crystal [86]. Since the grain boundaries are filled with trap states, which in turn facilitates the segregation of halide ions. Therefore, the amount of strain centers for halide segregation can be efficiently inhibited by reducing the grain boundary density. The suppression of photo-induced phase segregation in all-inorganic perovskites can also be achieved by shrinking of the perovskite crystals to NCs. It is indicated the threshold grain size for induced phase separation is 46.7 nm, which corresponds to the diffusion length of perovskite [87]. Therefore, if the perovskite grain size was greater than the threshold, the charge would diffuse with its diffusion length, and the electron/hole mobility would not be contained in the grain. Wang et al. also examined the impact of crystal size, reporting that when implanted in non- perovskite $Cs_4Pb(Br_x I_{1-x})_6$ endotaxial matrices, photo-induced phase separation was significantly inhibited for $CsPb(Br_xI_{1-x})_3$ NCs [88]. They showed that NCs with a 7.5 nm crystal diameter exhibited better photostability than NCs with a 35 nm crystal diameter. This finding is attributed to the Gibbs free energy equation, which states that an NCs size must reach a critical value for phase segregation to predominate and the volume proportional term to dominate. The charge traps in perovskite material are also attributed to phase segregation, resulting in an effective trap state passivation technique to improve perovskite photostability. For instance, Yuan et al. performed a series of experiments aimed at passivating deep trap states in $CsPbI_2Br$ perovskite films by introducing a solution of $Pb(NO_3)_2$ methyl acetate to the film [89].They observed that the trap state density of the perovskite decreased from 8×10^{16} to 6.64×10^{16} cm^{-3} after passivation of trap states. Several research groups have also introduced a variety of passivation agents, including potassium bromide, polymethyl methacrylate (PMMA), triiodine molecules, and trioctylphosphine oxide [68, 83, 90, 91]. After adding PMMA to the $CsPbI_{3-x}Br_x$ microplatelet, Wang et al. also reported decreased phase segregation, which is attributed to vacancy passivation at the perovskite

surface [91]. Similarly, Yang et al. found that PL shift was reduced in all-inorganic $CsPb_{3-x}Br_x$ NCs after passivation with KBr, while the pristine counterpart exhibited phase segregation with the PL peak shifting from 638 nm to 661 nm [90].

3
Experimental Techniques

Contents

3.1 Introduction

This chapter introduces the techniques I employed to investigate the properties of $CsPbBrI_2$ thin films, $CsPbBrI_2$ nanocrystals and $CsPbBr_3$ quantum dots. Most measurements were optical, using a laser to excite the samples and then passing the photoluminescence emission into several detection instruments. Section 2 lists the excitation sources that were used in this thesis. Section 3 describes the most common measurement method, micro-photoluminescence spectroscopy, which involves sending the emitted light through a spectrometer and capturing the spectrum with a CCD camera. Section 4 covers time-resolved micro-photoluminescence, another essential measuring technique that records

optical processes with sub-nanosecond time resolution using a photo-multiplying detector and time-correlated photon counting card. Finally, Micro-photoluminescence maps over regular grids of points in a 2D plane are reported in Section 5.

3.2 Excitation sources

3.2.1 Continuous Wave Lasers

All of the micro-photoluminescence measurements were made using above-bandgap excitation. For the $CsPbBrI_2$ films samples, the band gap was more than 1.90 eV, with a wavelength emission of 562.5 nm , so a 532 nm Nd:YAG diode laser with a maximum output power of approximately 1.7 mW was used as well as a 632.8 nm HeNe laser. The band gap of the $CsPbBrI_2$ nanocrystal and $CsPbBr_3$ quantum dot samples was 2.01 and 2.33 eV, with a wavelength emission of 615 and 532 nm, respectively. Therefore, a 405 nm InGaN diode laser with a maximum output power of approximately 1.7 mW was used. For the 532 nm neodymium-doped yttrium aluminum garnet (Nd:YAG) laser, the internal component is an III-V diode that pumps the Nd:YAG crystal at 808 nm, producing emission at 1064 nm [92]. This 1064 nm light is then focused through a crystal of KTP which doubles the frequency of the light through a nonlinear optical process [93]. For some applications, adding a filter to the optical path is necessary because, depending on laser quality, the pump beam can leak into the output beam. For this experiment, two distinct Nd: YAG lasers were used: one that showed the 808 nm emission and one that did not. The power of each laser's output was about 60 mW. A continuous wave laser with a blue 405 nm diode laser with an output power of 10 mW was also used for $CsPbBrI_2$ nanocrystals, as detailed in Chapter 5.

3.2.2 Pulsed Lasers

The work in this thesis required fast excitation sources with a high peak power needed for time-dependent measurements and nonlinear excitation. A frequency-doubled mode-locked Ti:Sapphire laser tuneable near 400 nm and a 450 nm PicoQuant pulsed diode laser were the two lasers employed for time-resolved micro-photoluminescence studies of the perovskite samples.

Ti:Sapphire Laser

The Ti:Sapphire laser is named after the Al_2O_3 crystal, which is doped with Ti^{3+} ions and works as the gain medium [65]. This is driven by a 532 nm diode laser with a Nd:YVO_4 gain medium, resulting in 1064 nm light that is subsequently frequency doubled. Modelocking is accomplished through the optical Kerr effect, a non-linear optical process in which the refractive index of the medium increases as the optical power density increases [94]. The Ti:Al_2O_3 crystal exhibits this effect, which induces the self-focus of light of sufficient intensity. The Kerr effect results in the two modes having distinct beam diameters and divergences, as the optical power density in the pulsed mode of operation is orders of magnitude greater than in the continuous wave (CW) mode. Consequently, it is feasible to develop cavities that prioritise pulsed operation over continuous wave (CW) operation [95]. The Spectra-Physics Mai Tai Ti:Sapphire laser employed in this study was capable of emitting at a wavelength of 800 nm with a power of 0.75 W, a repetition frequency of 80 MHz, and a pulse duration of 100 fs. This results in a maximal power of at least 94 kW and a pulse energy of 9.4 nJ.

450nm Diode Laser

In order to perform time-resolved measurements on the perovskites, it was imperative to use a laser with a shorter wavelength to induce excitation above the band gap. The laser source was a PicoQuant LDH-P-C 450B InGaN laser diode head driven by a PicoQuant PDL 808 "Sepia" controller. Unlike the Ti:Sapphire laser, which relied on physical mode-locking within the laser cavity to create pulses, this laser-generated pulses by the controller delivering power pulses to the laser diode [96]. This provided a substantial improvement in controlling the timing of the laser pulses. The controller allows for adjusting the pulse rate within the range of 5 MHz to 80 MHz, with a pulse length of less than 70 ps. In addition, the controller offered a secondary output from the crystal oscillator that could be linked to the "sync" input of the time-correlated single photon counting card. The laser's greatest average power was around 8.3 mW. However, decreasing the repetition rate led to a corresponding decrease in the average power while the energy per pulse remained constant.

3.3 Micro-Photoluminescence spectroscopy

Micro-Photoluminescence (μ-PL) is an optical technique used to characterize material properties through confocal illumination and collection of light emitted in order to spatially-resolve the emission from materials. Generally, PL processes comprise three essential phases, including excitation, thermalization and recombination. This technique involves a collimated monochromatic light source, typically a laser, with photon energy higher than the bandgap energy in the measured materials, which is focused tightly by a high power microscope objective. In the case of a dye molecule, as illustrated in Figure 3.1(b), when the photons interact with the sample, the electrons in a ground vibrational state will be excited and promoted to an excited vibrational state creating electron-hole pairs. The excitons (electron-hole pairs) can undergo to relax towards a quasi thermal equilibrium distribution. The recombination between electron and hole thus will transform partly into radiative and non-radiative recombination emission energy when the electron returns to the original ground states.

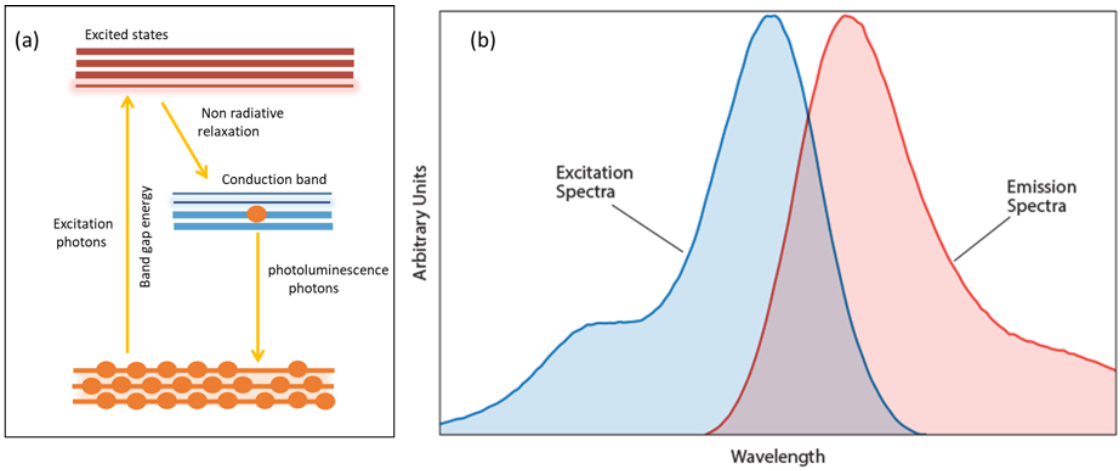

Figure 3.1: (a) A pictorial representation of the processes underlying PL.(b) Generic excitation and emission spectra for a fluorescent dye

Figure 3.2 displays a comprehensive representation of the entire μ-PL system applied in this thesis. A Thorlabs cage system was used to mount optical components. The fundamental cage system comprises four parallel metal shafts that serve as mounting points for additional components. Using junction cubes and 45° mirror units enables the interconnection of cage sections. However, it is essential to note that the connected

sections are limited to a fixed angle of 90° in relation to one another. It is worth noting that all optical paths running along three axes (east-west, north-south, up-down) make the system easier to design and maintain, as well as less likely to make beam distortion due to misaligned optical components. In the case of vertical sections, this feature enhances the safety of the system by ensuring that all laser beams are either aligned parallel to the optical bench, remaining below eye level or are obstructed by a stationary mirror positioned at the top.

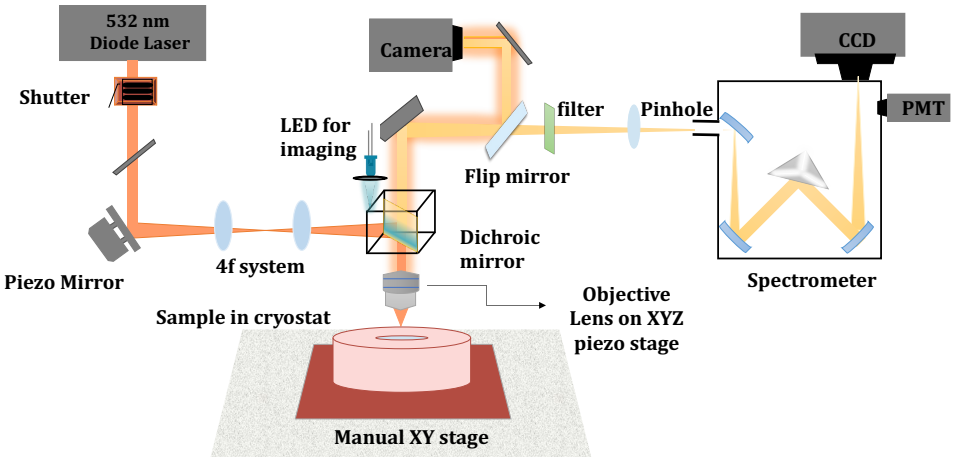

Figure 3.2: A diagram of the entire micro-photoluminescence spectroscopy system. Multiple different lasers with different wavelengths were used as excitation sources, but these have been omitted for simplicity.

In this research, various laser sources that produced light above the band gap were used as excitation sources for both single and lead mixed halide perovskites. Usually an objective lens was employed to focus the laser light onto the sample's surface, and the emitted light was subsequently collected along the identical path using the identical lens. Throughout all μ-PL measurements, excitation occurred above the band gap, resulting in light emission that consistently surpassed the wavelength of the laser. Therefore, by employing a dichroic filter positioned at a 45° angle to reflect the laser while allowing the emission to pass through, it was consistently possible to distinguish the collected light from the laser light.

he majority of the measurements were conducted using a Mitutoyo-manufactured objective lens. The instrument was designed to operate specifically at visible wavelengths and featured a 100× magnification and 0.5 numerical aperture (NA). In some scenarios, it is advisable to limit each μ-PL measurement to a small area (or volume) on the sample. Confocal microscopy is the method employed to accomplish this. A focal point with a diameter of approximately 1 μm can be achieved by spatially filtering the input beam with a single-mode optical fibre or pinhole. The collection path can be restricted by applying the same principle to the volume from which light is collected. However, the intensity of the collected light is inevitably reduced by a significant amount, typically at least 50%, because of spatial filtering. In certain cases, the increase in collection efficiency is more valuable than the loss in spatial resolution, and it is not always necessary to employ strong spatial filtering on the output, depending on the precise nature of the sample being studied. To eliminate any unwanted laser light that had been reflected by the sample, the captured light was directed through a long-pass filter before reaching the spectrometer. This is crucial because the high intensity laser light can disperse within the spectrometer and generate incorrect signals on the detector in the absence of the filter.

To obtain non-confocal collection, a 5× magnification lens was used to concentrate light into the input aperture of the spectrometer. Although the aperture restricted the width of the focused light that could penetrate the spectrometer, it still maintained confocality in one dimension. This was required to obtain high spectral resolution, as the spectrometer directly imaged the input aperture onto the CCD. A loss of resolution would result if the input aperture was set too wide, as any given spectral line would be equally dispersed on the detector. Even though this configuration was strictly only confocal in one dimension, it was able to obtain a relatively high spatial resolution on certain samples due to the small size of the excitation laser spot.

In this research, two spectrometers were used: an Andor Shamrock 0.3 m imaging spectrograph in a Czerny-Turner configuration and a 0.5 m focal length Light Field spectrograph from Princeton Instruments. They were equipped with three distinct diffraction gratings that spanned the range of wavelengths in the visible and near-infrared regions of the electromagnetic spectrum. To get insights into the characteristics of

diffraction gratings and, consequently, the capabilities of the spectroscopy system, it is imperative to delve into the theoretical aspects of diffraction gratings.

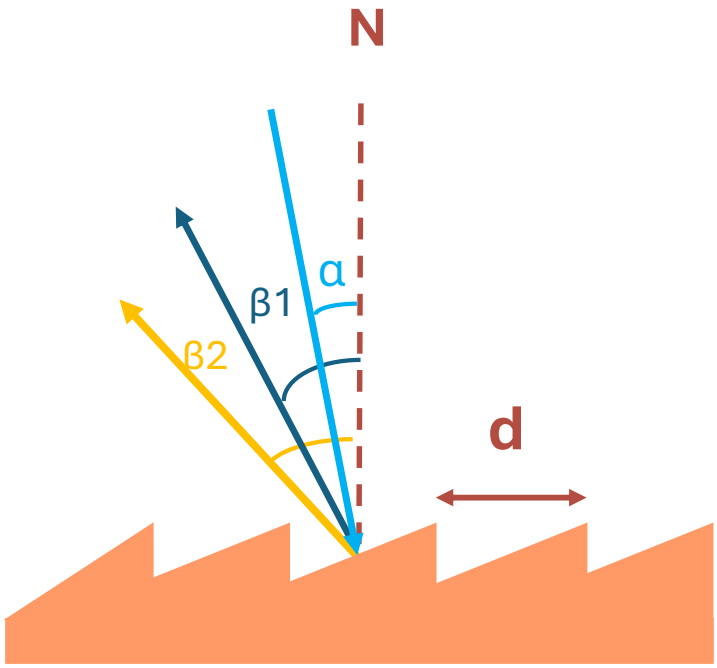

Figure 3.3: The function of a diffraction grating that reflects light. Two dispersion angles, denoted as β_1 and β_2 , are illustrated in the schematic to represent outgoing beams of constructive interference.

Figure 3.3illustrates that when light is incident at an angle α relative to the normal, a grating reflects light of wavelength λ most effectively at a blaze angle θ, as described by the generalized grating equation [97].

$$d(\sin\alpha + \sin\theta) = m\lambda \qquad (3.1)$$

by which d represents the distance between adjacent lines on the surface of the grating, while the variable m is an integer denoting the order of the reflection . In practical systems, the angular width of the diffracted beams is finite and is determined by the size of the illuminated region on the grating. The finite size of the illuminated region functions as a finite aperture, thereby limiting the contribution of Fourier components to the outgoing beam and necessitating a divergence greater than zero. From the

quantum physics perspective, the presence of a finite aperture results in the extraction of some information regarding the position of a photon, thereby leading to an inherent uncertainty in its velocity.

Eq. (3.1) shows that the zeroth order ($m = 0$) dispersed beam contains all wavelengths and reflects at the plane mirror angle. The spectrometer uses the first-order ($m = 1$) diffraction peak. In the process of measuring various wavelengths, the grating is adjusted in rotation to focus the specific range of wavelengths on the detector.

Additionally, each grating is blazed, indicating that instead of possessing a uniformly flat surface with regularly spaced grooves, the structure consists of angled reflecting parts resembling a saw-tooth pattern. The purpose is to maximize the incident light that reaches the first-order reflection. Due to the wavelength dependence of the angle of first-order reflection, the optimal operation of a blazed grating is limited to a specific wavelength. Beyond that wavelength, the light collection efficiency gradually decreases, with the reflectance falling to half its maximum value at wavelengths of $2\lambda_{\text{Blaze}}$ and $2\lambda_{\text{Blaze}}/3$. Also, the detector will register an incorrect signal when the second-order diffraction peak from 600 nm light occurs at the same angle as the first-order diffraction peak from 1200 nm light. For this reason, a long-pass filter is usually placed in the optical path before recording the signal through the spectrometer.

In our work, the spectra were recorded using two different types of detectors. An Andor-iDus InGaAs diode array was used for the near-IR samples. The device features a linear array consisting of 1024 pixels, with each pixel measuring $25\,\mu\text{m} \times 500\mu\text{m}$ in size. For the samples that emitted in the visible a front-illuminated Andor Newton EM silicon CCD camera was used. This camera features a 2D array consisting of 1600×200 pixels, with each pixel measuring $16\,\mu\text{m} \times 16\,\mu\text{m}$. To mitigate the dark count, both detectors were cooled using integrated thermoelectric coolers to a temperature of about -120°C and -50°C, respectively.

In this work, the size of CCD pixel was the primary factor limiting the spectral resolution for the spectrometer configuration employed. In other words, the spectrometer resolution is determined by the length of the optical route inside the spectrometer, which establishes the ratio between the angular dispersion from the grating and the spatial

Line density (Lines/mm)	Blaze wavelength (nm)
600	1200
1200	1100
1200	500

Table 3.1: presents a comprehensive list of the spectrometer gratings utilized in the conducted experiments in this research

dispersion on the CCD. As the distance between the grating and the CCD and the focal length of the internal focusing mirror increase, the wavelengths spread out in space and become farther apart on the detector. Thus, this for longer focal length spectrometers we get higher resolution for the same grating period. In general, the resolution of an array of sensor pixels is defined as the smallest distance, $\Delta\lambda$, that allows for the differentiation of two narrow peaks at their centres. In order to resolve the distance between two peaks, a local minimum must exist between them; in the worst case, this entails a minimum centre-to-centre separation of three-pixel widths. Table 3.1 shows the properties of the various gratings that were employed in this research. When paired with the InGaAs diode array detector, a resolution limit of 0.33 nm and 0.084 nm for the 600 lines/mm and 1200 lines/mm gratings respectively when measuring emission at a wavelength of 1300 nm. The last grating was blazed for the visible spectrum and was used with the silicon CCD detector for studying the perovskite samples. Its effective resolution at a wavelength of 600 nm was 0.055 nm.

3.4 Micro-Photoluminescence Mapping

Micro-Photoluminescence Mapping is a technique that can record an image of the PL spectra as a function of position on the sample instead of registering the PL spectrum from a single point on the sample. It is also capable of precisely relocating excitation or collection spots on the sample with sub-μm precision. The movements around the samples can be executed by affixing the cryostat to an *xy* stage and adjusting its position with manual micrometers. In addition, piezoelectric actuators were used to adjust the optical path in order to achieve precise positioning and computer control. Two distinct approaches were employed for the μ-PL map, known as the standard and excitation mapping.

3.4.1 Standard Mapping

The easiest positioning method is moving the collection and excitation spots concurrently, similar to moving the sample under a stationary μ-PL system. Since the cryostat was too heavy for a piezo-actuated stage, the objective lens was mounted on a piezo-driven *xyz* stage. The paraxial approximation was applied because the maximum deviation from the central axis was only $70\,\mu$m. Due to the angle of the collimated beam remaining constant, an ideal lens can constantly focus the light in the same place as itself. As the objective lens was moved, the position of the focal spot correspondingly shifted. The same concept can be applied to collected light; therefore, shifting the objective with small distances can be considered as moving the sample. A PI P-611.3S Nano-Cube *xyz* Piezo Stage with a range of $100\,\mu$m in all three directions and a PI P-733.3CD *xyz* Piezo Nano-positioning Stage with a range of $100\,\mu$m in *xy* and $10\,\mu$m in *z* were used throughout this research. The sample surfaces were excited using a 450 nm pulsed diode laser operating at a power of 0.88 mW or a wavelength of 405 nm CW at $100\,\mu$W . The dichroic mirror was also sometimes substituted by a 50:50 broad-band beam splitter to ensure the excited light could be tuned without realignment. For this reason, one 500 nm to 580 nm band-pass filter was employed to block reflected laser light. This enabled the sample emission to pass through, producing a good signal when integrated across the entire CCD. In order to reduce the period to complete the μ-PL map, the exposure time can be varied from 1 to 0.1 seconds. As illustrated in Fig. 3.4 (a), the μ-PL map was taken across a $20\,\mu\text{m} \times 20\,\mu$m region, employing a $0.5\,\mu$m step size along both axes. Although the sample's uniform grid pattern is readily apparent, close examination reveals a slight degree of deformation. To trace the source of this distortion, our former PhD student, Luke P. Nuttall, developed quantitative analytic algorithms and code in 2019. Guanhua Ying then modified the code in 2021 to accommodate all circumstances examined in this thesis.

3.4.2 Excitation Mapping

Instead of moving both excitation and collection synchronously, another mapping method can be implemented by employing the scanning mirror, allowing to decoupling between the excitation and collection approach. The scanning mirror used in this study is a

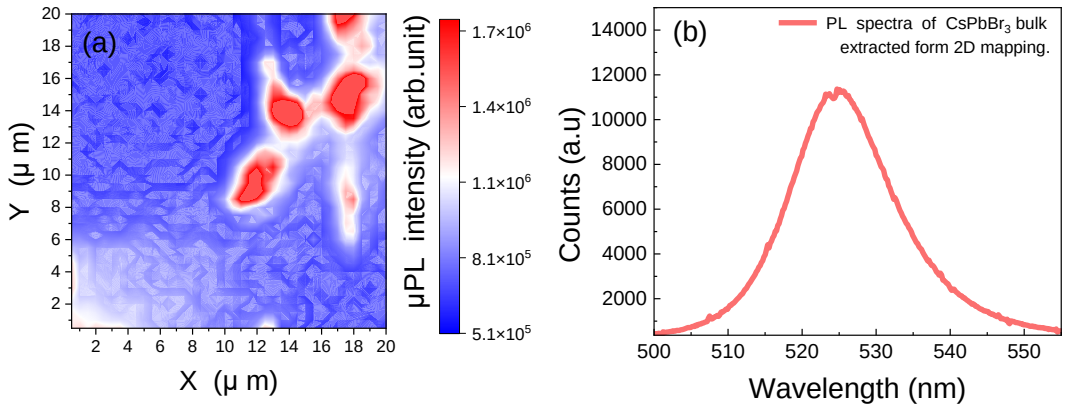

Figure 3.4: Room temperature μ-PL map of a $20\,\mu\text{m} \times 20\,\mu\text{m}$ area of a perovskite sample

Connex AG-M100D mirror, which is driven by a piezo-actuator. This mirror is capable of deflecting the incident beam by tiny angles. Nevertheless, this will cause the beam to deviate from the central point of the objective lens. In order to address this issue, a telecentric $4f$ configuration was employed, utilizing a pair of lenses with identical focal lengths f, positioned between the scanning mirror and the objective. According to the illustration presented in Figure 3.5, the $4f$ system had two lenses with identical focal lengths, positioned at $2f$ from each other. The lens situated on the left side, functioned as an image-space telecentric lens. The process of this lens involves the collection of collimated light that is reflected from the piezo mirror and subsequently focused to a specific spot inside the plane located at the midpoint of the system. The position of the focal point at the center was contingent upon the angle, θ, at which light underwent reflection from the mirror. The second lens, situated on the right side, functioned as an object-space telecentric lens. The purpose of this lens is to collect the focused light from the intermediate plane and re-collimate it before to its entry into the objective lens. Due to the inherent symmetry of the system, the collimated beam that entered the objective has the same dimensions as the beam that was reflected from the mirror, while their respective angles remained consistent. Furthermore, the position of the output beam at the objective lens remained consistently centered along the optical axis, even as the angle of the beam changed. Furthermore, the size of the collimated beam will be

reproduced upon striking the scanning mirror, indicating that only the incident angle has been altered. Under the assumption of the small angle approximation, such variation in the incident angle will result in a corresponding position displacement on the sample surface. In addition to full mapping at small steps, these two fine position procedures can be combined with cryostat coarse position control using a micrometer stage for sample surface searches and output signal optimization.

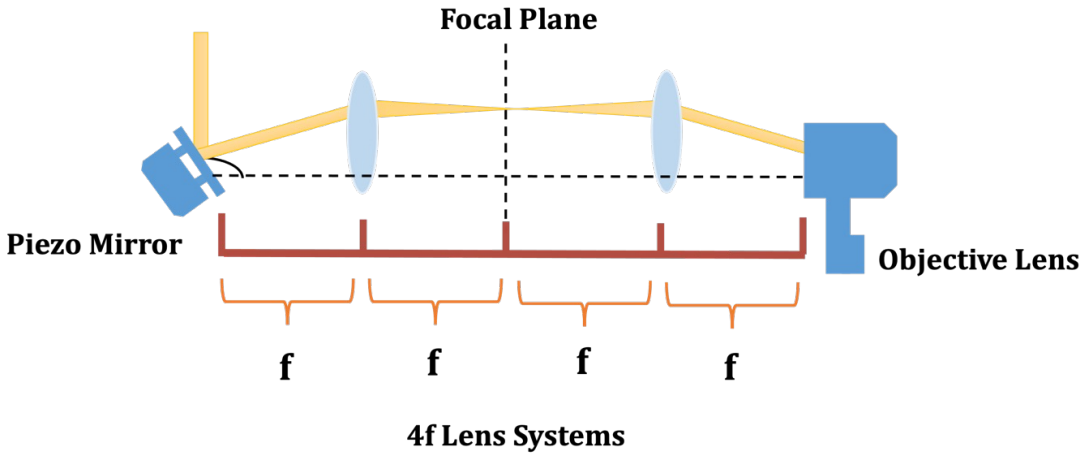

Figure 3.5: A schematic representation of the $4f$ system employed for accurate manipulation of the excitation laser spot's position on the sample. The variable f represents the focal length of both lenses. The collimated beam consistently enters the center of the objective at the same angle, regardless of the angle at which it is reflected off the scanning mirror.

3.5 Time-Resolved Micro-Photoluminescence

In contrast to μ-PL spectroscopy, which involves the integration of photon counts across time, time-resolved photoluminescence (TRPL) studies focus on analyzing time intervals between photon occurrences, achieving a high resolution on the scale of nanoseconds or even picoseconds. The TRPL system consists of two primary components: the photodetector, responsible for converting photons into electrical pulses, and the time-correlated single photon counting card, which records the temporal arrival of these pulses relative to pulses recorded at a synchronization input as depicted in Figure 3.6.

In this study, two different photodetectors were employed for the TRPL (time-resolved photoluminescence) measurements. The principal detector used was a Hamamatsu

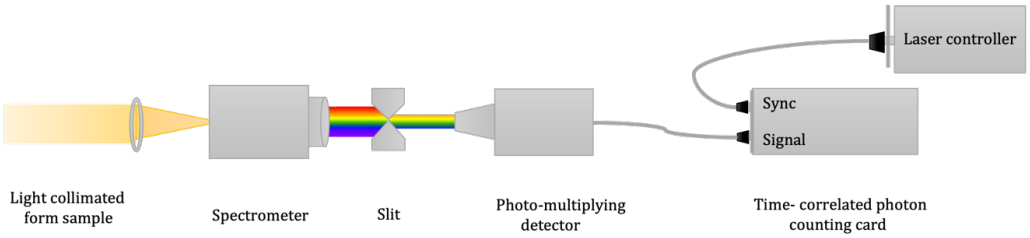

Figure 3.6: Schematic illustrates the essential optical components of Time-Resolved Micro-Photoluminescence spectroscopy.

H7422P-50 photomultiplier tube (PMT). This detector exhibits sensitivity covering the entire spectral range of 380 nm to 890 nm, thereby encompassing the emission wavelengths of the perovskite samples. A PicoQuant TimeHarp 260P time-correlated photon counting (TCPC) card was connected to a computer, while the synchronization input was supplied by the controller for the 450 nm diode laser. The second detector was an MPD Si avalance photodiode (APD) with 50 ps time resolution, coupled to the spectrometer output by a 100 μm multimode fibre. This worked well for measuring fast emission and bluer samples.

The TCPC card function is based on registering the arrival time for every voltage pulse it receives from a detector. An internal timer is initiated once a pulse arrives on the synchronization input. This timer records the precise arrival time of every sequential pulse on the input signal to within 25 ps with a maximum duration of 819 ns. The timer is reset when another synchronization pulse is recorded; therefore, all recorded times are related to the last synchronization plus. By iteratively executing this procedure across a vast number of synchronization pulses, it is possible to construct a histogram that represents the distribution of arrival times in relation to a reference point. At a sufficient rate, the TRPL system enables the observation of the decay process of excited carriers resulting from the absorption of a laser pulse. Analyzing the decay curve properties can yield a profound understanding of a given sample's energy levels and carrier dynamics.

One of the most important features of this TimeHarp 260P TCPC card is that can offer multi-stop modes, while the old version of TCPC hardware records the arrival time of a single pulse for each sync pulse. For instance, in old version cards, the timer is initiated by the sync pulse and then terminated by the signal pulse. Subsequent signal pulses cannot

be recorded until the next sync pulse is received. Nevertheless, the multi-stop modes provided by the TimeHarp 260 TCPC card enables the recording of numerous signal pulses subsequent to a single sync pulse. However, two factors influence the efficiency of these systems, namely, the TCPC card's dead time and the PMT response to incident photons. For example, there is a latency of up to 25 ns between detecting an electrical pulse from the PMT on the input channel and completing the recording operation; at this point, the electronics become prepared to receive another pulse. During this dead time, the pulses that were received were lost. Although high photon flux on PMT can shorten the time it takes to build a histogram, this dead time implies that a high-count rate may exclude some data points and influence the decay curve, thus favoring earlier times. This means that the count rate should always be kept to less than 10^5 counts/s.

It is noteworthy that the ideal detector would output a single electrical pulse when a photon arrives. However, the real detectors can have faults due to electrical reflections inside the processing circuitry, causing random delays and secondary peaks, namely the instrument response function (IRF). Also, it refers to the time-domain signal recorded by the TCPC card upon exposure of the PMT to a short light pulse. For instance, the instrument response function (IRF) shown in Figure 3.7 was plotted by using pulses from the 450 nm diode laser as the input to the PMT. When conducting measurements using the TRPL system, the recorded signal is the result of convolving the real-time response of the sample with the IRF of the detector. Consequently, it becomes imperative to carry out deconvolution in order to analyze the data effectively if the lifetimes are short.

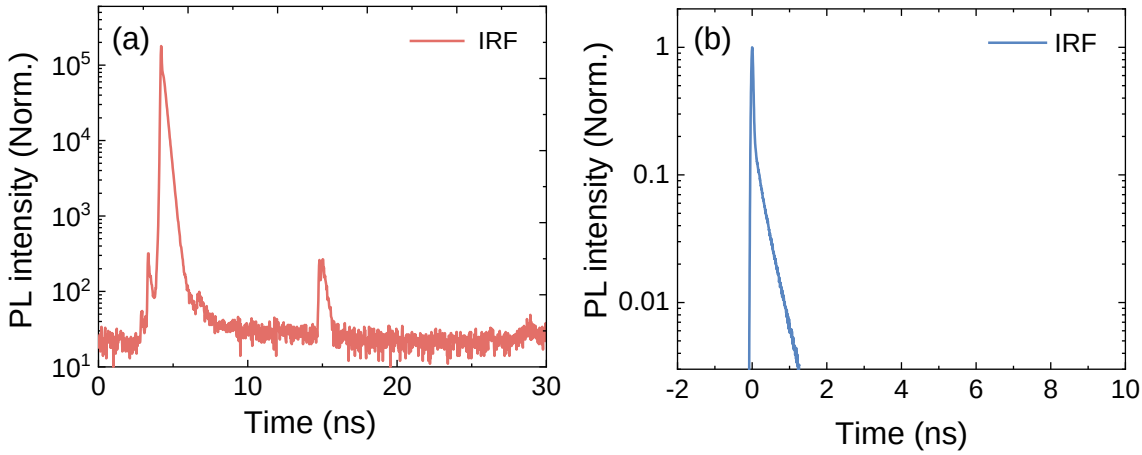

Figure 3.7: An instrument response function (IRF) of the TRPL measurements (a) 450 nm Pulsed laser detected by the PMT in which the main peak related to the first detection of the laser pulse, while the smaller peaks are usually caused by electrical reflection effects (b) Ti:sapphire laser at 800 nm used for this thesis detected by the APD.

4

Stability of Mixed Lead Halide Perovskite Films Encapsulated in Cyclic Olefin Copolymer at Room and Cryogenic Temperatures

Contents

4.1 Introduction

Recently, all-inorganic perovskites $CsPbX_3$ (X = I, Br, Cl) have attained extensive attention due to their optical properties and thermal stability, making them promising candidates for practical applications when compared to their organic-inorganic perovskite counterparts [98–100]. However, the $CsPbI_3$ perovskite can readily convert from the cubic phase α, β, γ-black phase to the orthorhombic phase δ-yellow phase under ambient conditions reducing photovoltaic performance given its large bandgap, high energy loss, and high defect density. Although $CsPbBr_3$ shows excellent thermal stability [101], it has a band gap of 2.3 eV restricting its further development [102, 103]. Mixed halide perovskites $CsPbI_{3-x}Br_x$ enable the bandgap to be tuned across the entire visible spectrum [27, 104]. Furthermore, halide mixing can address phase transitions and produce stable α-perovskites at working temperatures, and the bandgap makes them appropriate for high-performance tandem solar cell top cells [104]. $CsPbBrI_2$ in particular has reasonable bandgaps in the range of (1.82 – 1.92 eV) with a wide light absorption range exhibiting great potential in tandem and semi-transparent photovoltaic applications [98, 102, 103, 105]. In [38] it was shown that $CsPbBrI_2$ is stable in the cubic phase at room temperature even for bulk materials. However, upon continuous illumination, iodide and bromide ions migrate in the $CsPbBrI_2$ crystal lattice after obtaining sufficient energy and eventually accumulate at grain boundaries [73, 105] such that the ion accumulation leads to the formation of an I-rich phase (1.55 eV) and a Br-rich phase (2.3 eV), resulting in phase segregation deviating from the desired bandgap with red and blue shifts, respectively [106]. This can negatively impact devices. Along with ion migration, current density-voltage (I-V) hysteresis, and trap states can result in significant charge recombination, lower open circuit voltage, and lower fill factors (FF) values in devices based on mixed halide perovskite materials. Several theoretical models have attributed the driving force for phase segregation/separation to (i) internal lattice strain [107], (ii) polaron-induced lattice strain [85, 108], (iii) photocarrier energies [109–112] and (iv) the kinetics of halide vacancies. These are all discussed comprehensively in various reviews [101, 111]. The driving forces based on strain models are associated with an increase in shear strain

in the perovskite lattice originating from either an internal lattice mismatch between halide ions or an external polaron-induced structural deformation [69, 85, 99, 113]. Consequently, halide ion segregation is more likely to occur to release the lattice strains, leading to photoinstability. Also, the relaxation and deformation of the structural lattice of the perovskite relieve the free energy, further promoting halide ion segregation [100, 113]. However, the strain-based consideration fails to consider the role of defects and photoexcited charge carriers in phase segregation [85]. The photocarrier energy model involves the photogenerated charge carriers' role in the rearrangement of halide ions within the perovskite lattice and their kinetic processes, including carriers' generation, diffusion, and accumulation and recombination at I-rich domains [110, 111, 114]. A bandgap difference between the initial and segregated phases can also drive halide segregation, increasing the free energy of the mixed halide in excited states [69, 76, 77, 112]. As in strain models, such an increase in free energy needs to be minimized through halide segregation. The formation of halide vacancies inside the perovskite lattice can also be responsible for driving halide ion migration through defect-mediated movement. The migration is more likely to occur through halide Schottky defects or vacancies in the mixed halide perovskite lattice, which ultimately forms two stable Br-rich and I-rich phases under continuous illumination [69, 109, 111, 114]. More importantly, the lower activation energy for halide ion migration (0.17 – 0.43 eV for Br and I) than for cations (0.46 – 1.20 eV for Cs and 0.80 – 2.31 eV for Pb) and the resulting low formation of energy halide defects are mainly responsible for ion migration and generating a significant contribution to the ionic properties of MHPs [77, 107, 109]. Thus, it is essential to take into consideration all of these processes simultaneously, including halide defect generation, halide ion migration, polaron formation and any resulting phase segregation, as illustrated in Figure 4.1 (a,b) [98–100].

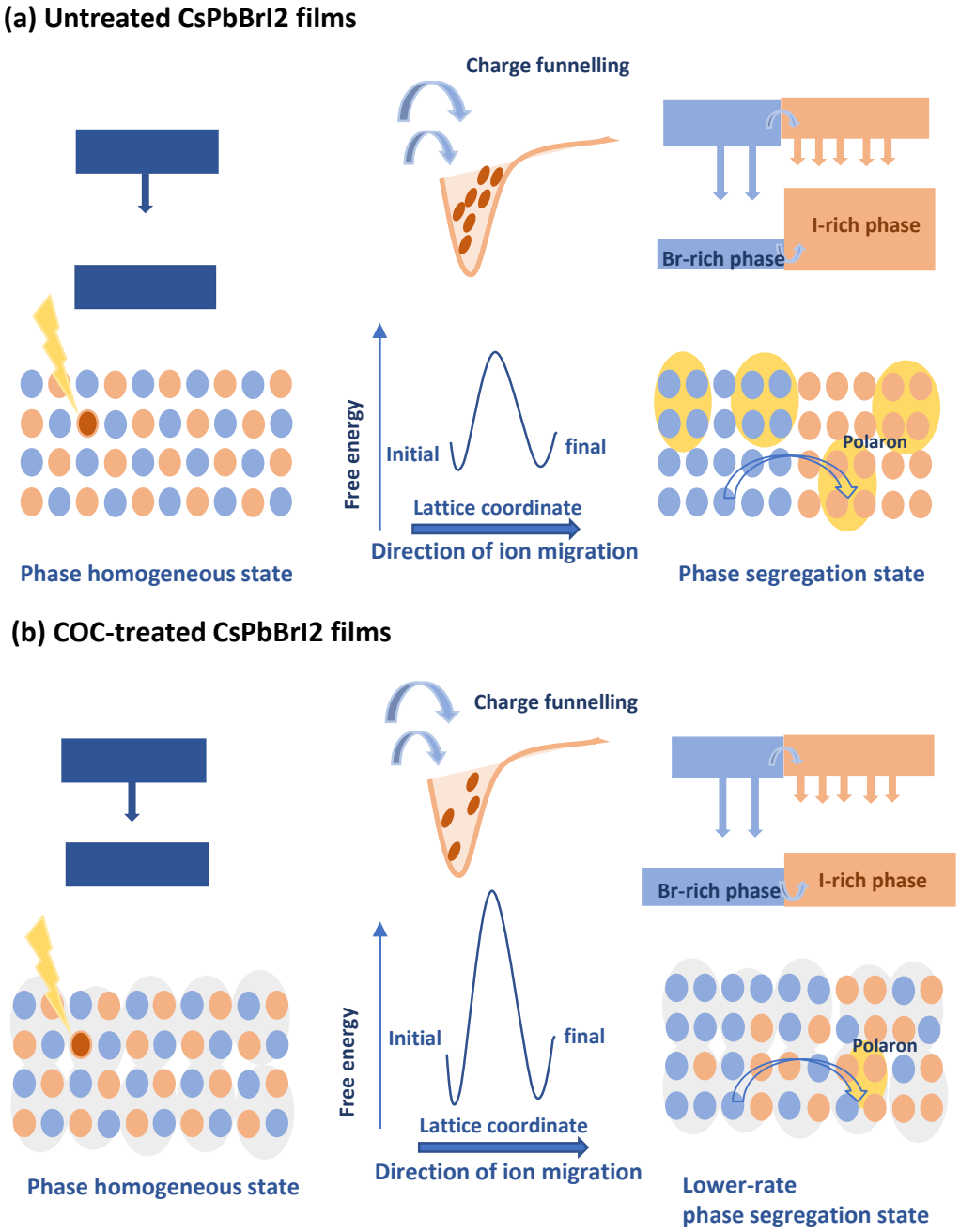

Figure 4.1: Schematics contrasting carrier and ion-migration dynamics in (a) untreated $CsPbBrI_2$ films and (b) COC-treated $CsPbBrI_2$ films.

4.2 Structure and Growth

4.2.1 Materials

The chemicals used for the sample growth were Caesium Iodide (CsI, 99.9% trace metals basis, Sigma Aldrich); lead bromide ($PbBr_2$, 99.998% metals basis, Alfa Aesar); lead iodide (PbI_2, 99.99%, TCI); dimethyl sulfoxide (DMSO, anhydrous, Sigma Aldrich); dimethylformamide (DMF, anhydrous, Sigma Aldrich); diethyl ether (DEE, anhydrous, Sigma Aldrich); isopropyl alcohol (IPA, technical grade, Sigma Aldrich); acetone (technical grade, Sigma Aldrich). All materials were used as-received without any further purifications and all precursors were stored and used in a N_2-filled glove box in the laboratory of Professor Henry Snaith at the University of Oxford.

4.2.2 Thin Film Deposition

Lead Mixed-halide perovskite $CsPbBrI_2$ films were fabricated through a spin-coating process by collaborators Ashley Marshall and Shaoni Kar, who work with Professor Henry Snaith's lab at the University of Oxford. The processes were conducted within a glove box filled with nitrogen gas, a controlled environment to prevent unwanted reactions, using anhydrous solvents that were meticulously prepared to be completely free of water. A 1 M solution of $CsPbBrI_2$ was prepared by dissolving 1 mmol of CsI, 0.5 mmol of PbI_2, and 0.5 mmol of $PbBr_2$ in 1 mL of DMF:DMSO mixture (3:1 volume ratio). The mixture was vortex mixed until no visible crystals remained in the solution and then it was left to stir until use. Glass substrates cut to 25 mm $\times$ 25 mm were cleaned using IPA and acetone, followed by 10 minutes of UV-ozone exposure. The cleaning process was done in air and the substrates were transferred to the N_2-filled glove box where they were spin-coating at the end of the UV-ozone treatment. 70 μL of $CsPbI_2$ solution was deposited on the center of the glass slide, then the spin-coating process was begun. The spin-coater was programmed to spin at 1000 rpm for 10 seconds, then 5000 rpm for 50 seconds. A timer was started along with the spin program and 350 μL of DEE was pipetted onto the center of the glass substrate when the timer reached 37 seconds. The substrate was then transferred to a hotplate pre-heated to 32 °C and dried for 10 minutes or

until dark brown. The films were annealed at 250 °C for 10 minutes following the drying. Samples were cut down to 5 mm × 5 mm for loading into the cryostat for measurements.

4.3 Room-temperature X-ray Characterization (XRD) for untreated and COC-treated $CsPbBrI_2$ films

The crystal structure was characterised by Shaoni Kar, DPhil students in Professor Henry Snaith's lab at the University of Oxford, using a Panalytical X'Pert Pro X-ray diffractometer equipped with a Cu-alpha source (wavelength $\lambda = 1.54$ Å). The X-ray diffraction (XRD) characterization was first performed on the untreated $CsPbBrI_2$ and the COC-treated $CsPbBrI_2$ films to examine the crystal structure and calculate the grain size, as shown in Figures 1a-1b. The position of diffraction peaks of 2θ at 15° and 30° remained unchanged, signifying the crystal structure of untreated $CsPbBrI_2$ remains in the cubic phase after being treated with COC. However, the gradual narrowing of the diffraction peaks was observed in the untreated $CsPbBrI_2$ films, indicating the enlarged grain size compared with the COC-treated $CsPbBrI_2$ films. Such gradual narrowing has been attributed threshold size of phase segregation which was equal or larger than 43 nm. Here we implemented the Rietveld refinement XRD method to calculate the accurate average grain size. This allows us to compare our experimental findings with a calculated diffraction pattern based on an initial structural model. We then fitted the peak positions and narrowing/broadening to generate the Williamson-Hall plots to correctly estimate the average grain size and the effect of micro-strain of untreated $CsPbBrI_2$ films and the COC-treated $CsPbBrI_2$ films. The average grain size calculated empirically by the Debye-Scherrer equation was 168 nm for untreated $CsPbBrI_2$ films, and 47.33 nm for the COC-treated $CsPbBrI_2$ as shown in Figures 1c-1d. This trend is consistent with tabulated values in a previous study [115]. This is supporting evidence that above a threshold size of segregation which has been reported to be 43-46 nm in the literature [87, 115], the diffusion length will be determined by the carrier's natural diffusion lengths rather than by the grain size. We revisit this below with time-resolved studies to confirm this result empirically.

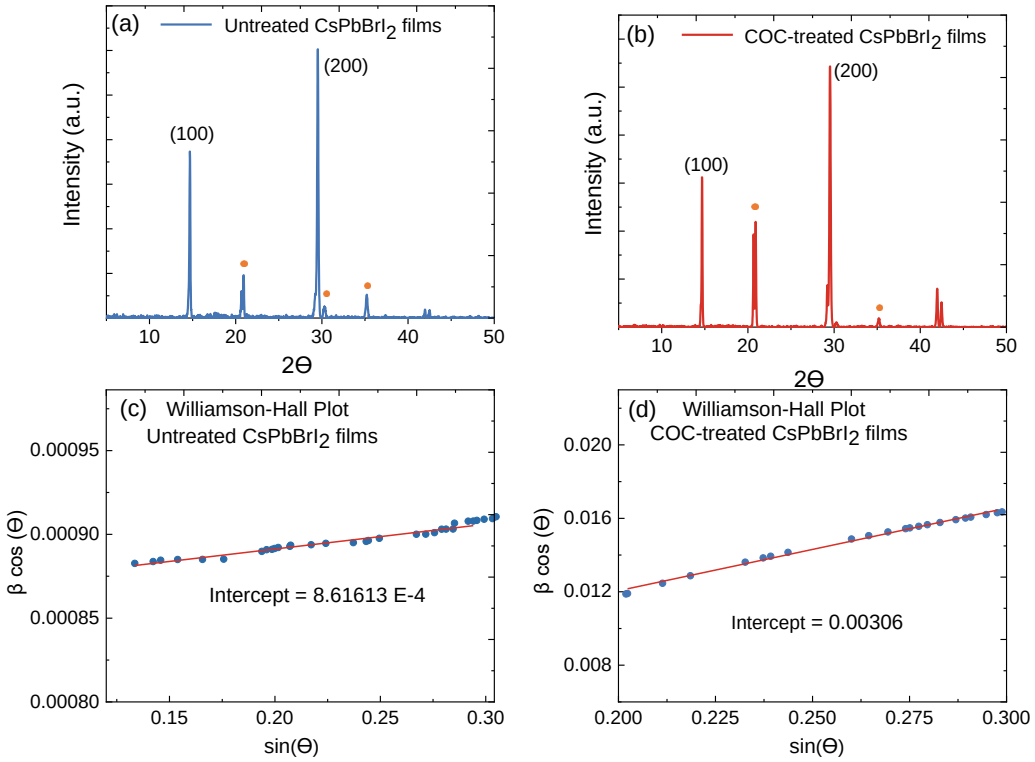

Figure 4.2: Room temperature X-ray diffraction (XRD) patterns of (a) the untreated $CsPbBrI_2$ films (b) the COC-treated $CsPbBrI_2$ films. Williamson-Hall Plot of the XRD data using the Rietveld refinement method where the slope is a macrostrain and the intercept is a crystallite size after using the Debye-Scherrer Equation (c) untreated $CsPbBrI_2$ films (d) COC-treated $CsPbBrI_2$ films.

4.4 Room-temperature PL time-series for untreated and COC-treated $CsPbBrI_2$films

To confirm the correlation between the grain size and phase segregation, a time dependent PL profile was implemented on both films. Figures 4.3(a) to (d)represent the evolution of the PL spectra for untreated $CsPbBrI_2$ films and COC-treated $CsPbBrI_2$ films at room temperature after being exposed to low and high excitation intensities of the green light irradiation (CW 532 nm) for 30 minutes. In Figures 4.3(a-b), the time dependence of the PL spectra in the untreated $CsPbBrI_2$ films was monitored at 400 μW, and 800 μW, respectively. In Figures 4.3(c-d), the time dependence of the PL spectra for COC-treated $CsPbBrI_2$ films was tracked at 60 μW, and 800 μW, respectively. Note that COC-treated

films were exposed to lower excitation power than untreated films. Specifically, in figures 4.3(a-c), although the excitation intensity used for the COC-treated $CsPbBrI_2$ films was four times less than that for untreated $CsPbBrI_2$ films, the final count rate for the PL emission was twice as high.

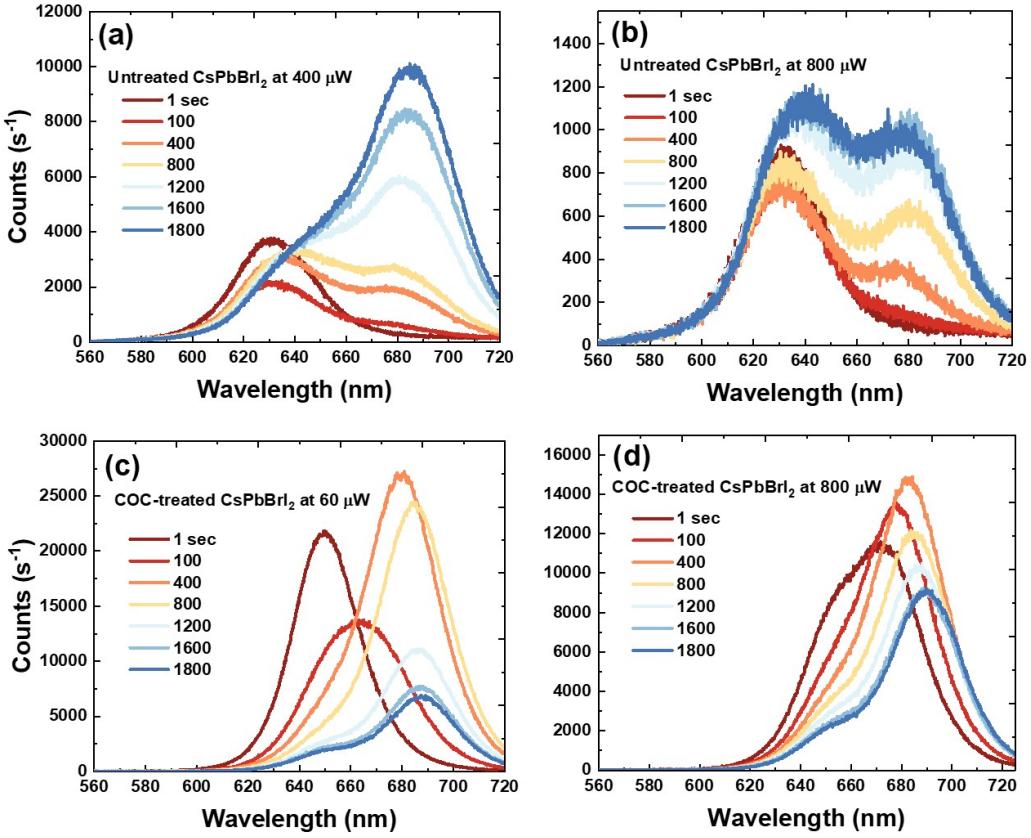

Figure 4.3: Room-temperature PL time-series for $CsPbBrI_2$ films without COC and with COC treatment at low and high excitation powers. (a) Untreated $CsPbBrI_2$ films at 400 μW, (b) untreated $CsPbBrI_2$ films at 800 μW, (c) COC-Treated $CsPbBrI_2$ films at 60 μW and (d) COC-Treated $CsPbBrI_2$ films at 800 μW films.

Figures4.3(b-d) the final count rate for PL spectra in the COC-treated $CsPbBrI_2$ films was five times higher as compared with untreated $CsPbBrI_2$ films even after being subjected to the same excitation intensity at 800 μW. This has been linked to asymmetric kinetic ion migration dependent non-linearly on the excitation intensity [110]. Thus, it is possible that excitation intensity threshold induced halide segregation is reduced, which in turn leads to the high emission intensity of COC-treated $CsPbBrI_2$ films. Such a reduction

was also attributed to the average grain size which tends to increase the energy associated with exchanging Br with I within phase-segregated domains, an increase in the carrier lifetime or an expansion of the geometrical volume linked to carrier diffusion lengths in the COC-treated films, which will be discussed in the time-resolved photoluminescence (TRPL) section [109, 110, 116, 117].

4.4.1 The band gap difference within 30 minutes of prolonged green illumination.

Firstly, the initial emission peak of untreated $CsPbBrI_2$ films was centered at 630 nm at 400 μW and 800 μW, in Figures 4.3(a)-(b) and 4.4(a)-(b). However, the initial emission peak of COC-treated $CsPbBrI_2$ films at 60 μW exhibited redshifts at 645 nm, in Figures 4.3(c) and 4.4(c), attributed to the energy changes due to the interface effect between the film and COC. This also possibly occurred due to the ligands removed from the $CsPbBrI_2$ film after COC treatment, which might increase the dielectric constant of the surrounding medium, consequently increasing the absorbance and giving slight redshifts [118–120]. In addition, the initial emission peak of COC-treated $CsPbBrI_2$ films at 800 μW exhibited a higher redshift of 670 nm, in Figures 4.3(d) and 4.4(d), suggesting a strong coupling involving energy transfer by the interface effect between the $CsPbBrI_2$ and the COC polymer [120].

Secondly, the final emission peak of untreated $CsPbBrI_2$ films at both excitation intensities exhibited a redshift of 55 nm at 685 nm with peaks at 630 nm emerging in Figures 4.3(a)-4.3(b) and 4.4(a) 4.4(b), indicating I- rich and Br-rich domains, respectively [65, 80, 108, 121, 122]. Although the COC-treated $CsPbBrI_2$ films showed similar behaviours, the final PL time series exhibited reduced redshifts of 40 nm at 60 μW and 15 nm at 800 μW at 658 nm in Figures 4.3(c) -4.3(d) and 4.4(c)-4.4(d) respectively. Also, I-rich domain nucleation was slowed down within 800 s at 60 μW, and 800 μW compared to the untreated $CsPbBrI_2$ films, suggesting a minimizing of the funnelled energy from ion migration along grain boundaries or a surface defect due to a blocking effect via COC [103, 123].

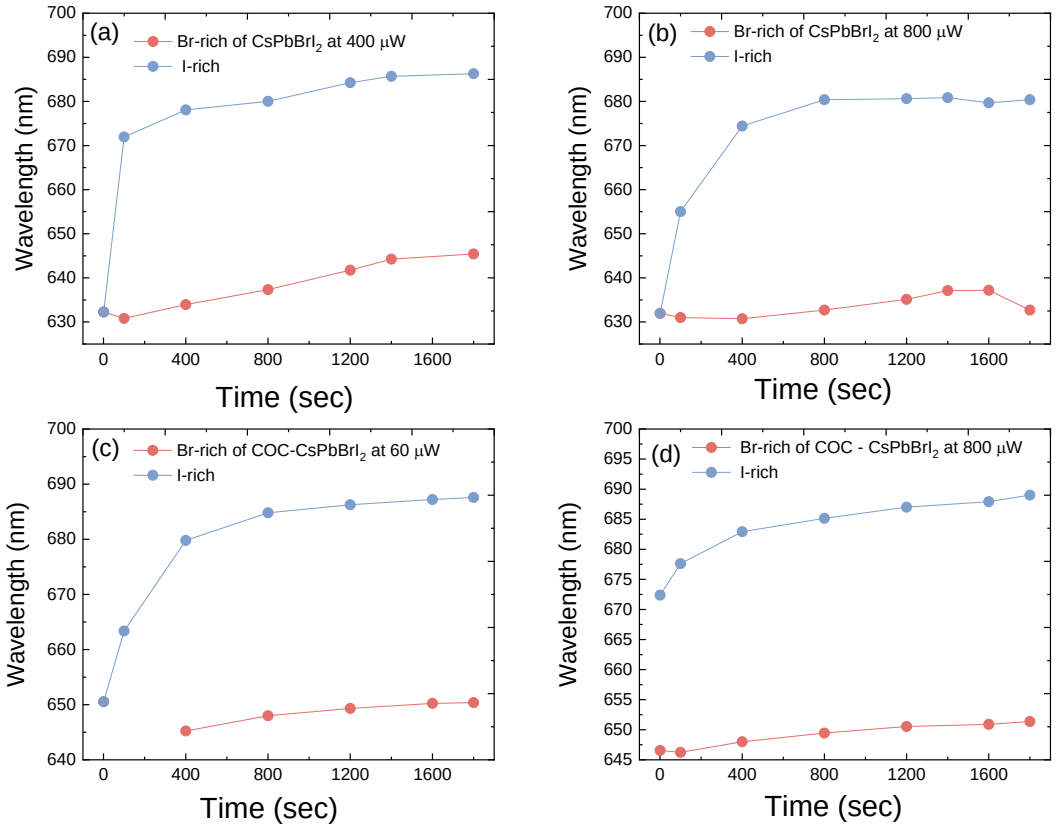

Figure 4.4: The rate of wavelength changes (the band gap difference from the initial mixed to final segregation states) for both untreated $CsPbBrI_2$ films and COC-treated $CsPbBrI_2$ films at room temperature after being exposed to low and high excitation intensities of the green light irradiation (CW - 532 nm) in 8000 seconds (a)(b) untreated $CsPbBrI_2$ films and (c)(d) in COC-treated $CsPbBrI_2$ films.

4.4.2 Kinetics of halide vacancy and polaron accumulation

In Figures 4.3(b) -4.3(d), the increase in the excitation intensity showed a positive correlation with the halide demixing and the reduction of PL count rates, indicating a significant valance band edge difference. Prominent halide demixing was observed in $CsPbBrI_2$ films at 800 μW. In contrast, the COC-treated $CsPbBrI_2$ exhibited less of a halide demixing effect, signifying higher entropic stabilization. To get a deeper insight, temperature-dependent PL spectra were measured for both films to calculate the activation energy using the Arrhenius model illustrated in Figures 4.5 (a-d). The activation energy for the COC-treated $CsPbBrI_2$ was found to be higher at 28 meV, while that of the

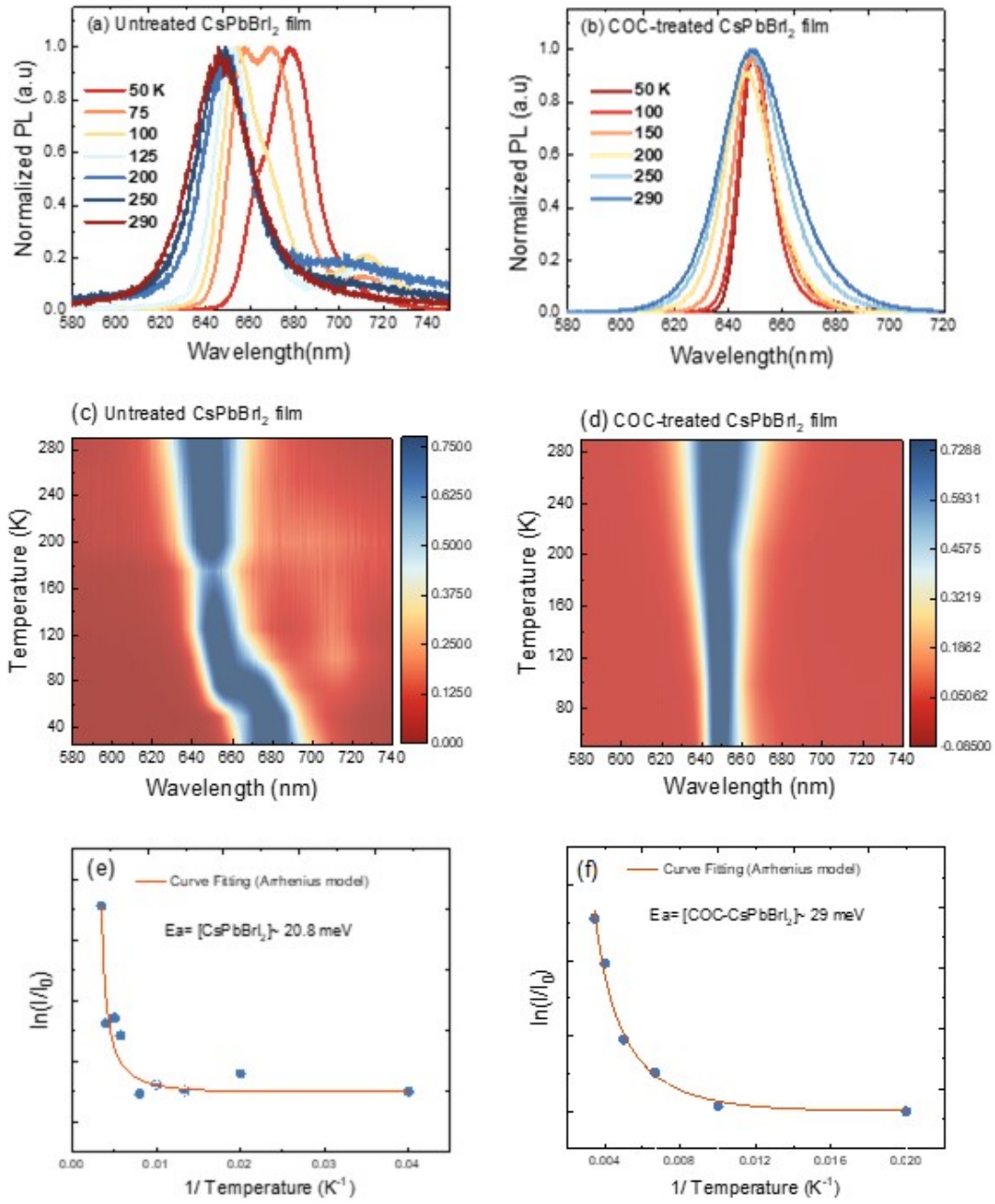

Figure 4.5: Temperature-dependent PL spectra and a 2D pseudo-color plot in the temperature region (4.2 K to 290 K) of (a) (c) untreated $CsPbBrI_2$ films (b)(d) COC-treated $CsPbBrI_2$ films, respectively. (e)(f) The PL intensity's natural logarithm as a temperature function for both untreated $CsPbBrI_2$ films and COC-treated $CsPbBrI_2$ films, respectively. The blue dots denote experimental data, and the solid lines fit the data using the Arrhenius model. The activation energy of untreated $CsPbBrI_2$ films is estimated to be 20 meV and the acctivation energy of the COC-treated $CsPbBrI_2$ films is approximately 29 meV.

$CsPbBrI_2$ film was estimated to be lower at 20 meV. In this regard, the lower activation energy of charge carriers can overcome the larger activation barrier of thermal mixed halides under high excitation intensity. The activation energy for the halide ion migration in COC-treated $CsPbBrI_2$ films is higher than in COC-treated $CsPbBrI_2$ films, reflecting the fact that halide ions exhibit fewer contributions to ionic conductivities according to the reverse order of the activation energies. This also suggests that the number of vacancies for halide ions in COC-$CsPbBrI_2$ films is relatively lower than in $CsPbBrI_2$ films because of the low formation energy, inevitably showing the fastest ion migration upon continuous illumination. This can in turn increase the concentration of charge carriers and halide vacancies accumulating and funnelling into the I-rich domain, leading to an increase in lattice distortion and more polaron formation [65, 69, 85, 109, 111, 112]. Note that the COC-treated film segregated faster within one second than the untreated film. It is hypothesized that more photo-excited carriers are generated at higher excitation intensity, strongly coupled to the perovskite lattice, forming a larger polaron size. Thus, the accumulation of strain energy might be higher or exceed the strain tolerance threshold of the COC-treated $CsPbBrI_2$ lattice [80, 121, 123].

4.5 Cryogenic (4.2 K) PL time-series for untreated and COC-treated $CsPbBrI_2$ films

In order to investigate these effects further, time-dependent PL at cryogenic temperatures was undertaken, where we expect less thermal lattice distortion, thereby lower polaron formation, as seen in Figures 4.6(a) to 4.6(d). In comparison to both films at room temperature in Figures 4.3(a) to 4.3(d), under prolonged illumination, a native broad peak stemming from bromide and iodide domains was observed at 685 nm in the untreated $CsPbBrI_2$ films at 20 μW and 80 μW in Figures 4.6(a)-4.6(b). Similarly, the predominant PL emission appeared at 675 nm in the COC-treated $CsPbBrI_2$ films 0.1 μW and 0.6 μW in Figures 4.6(c)-4.6(d), indicating the absence of a difference in the bandgap and a photocarrier funneling effect. Thereby, entropy remixing of halide ions dominates the enthalpy (lattice strain) due to entropic stabilization. The COC-treated $CsPbBrI_2$ films exhibited a narrower PL peak and blue shift of 5 nm compared to untreated $CsPbBrI_2$ films

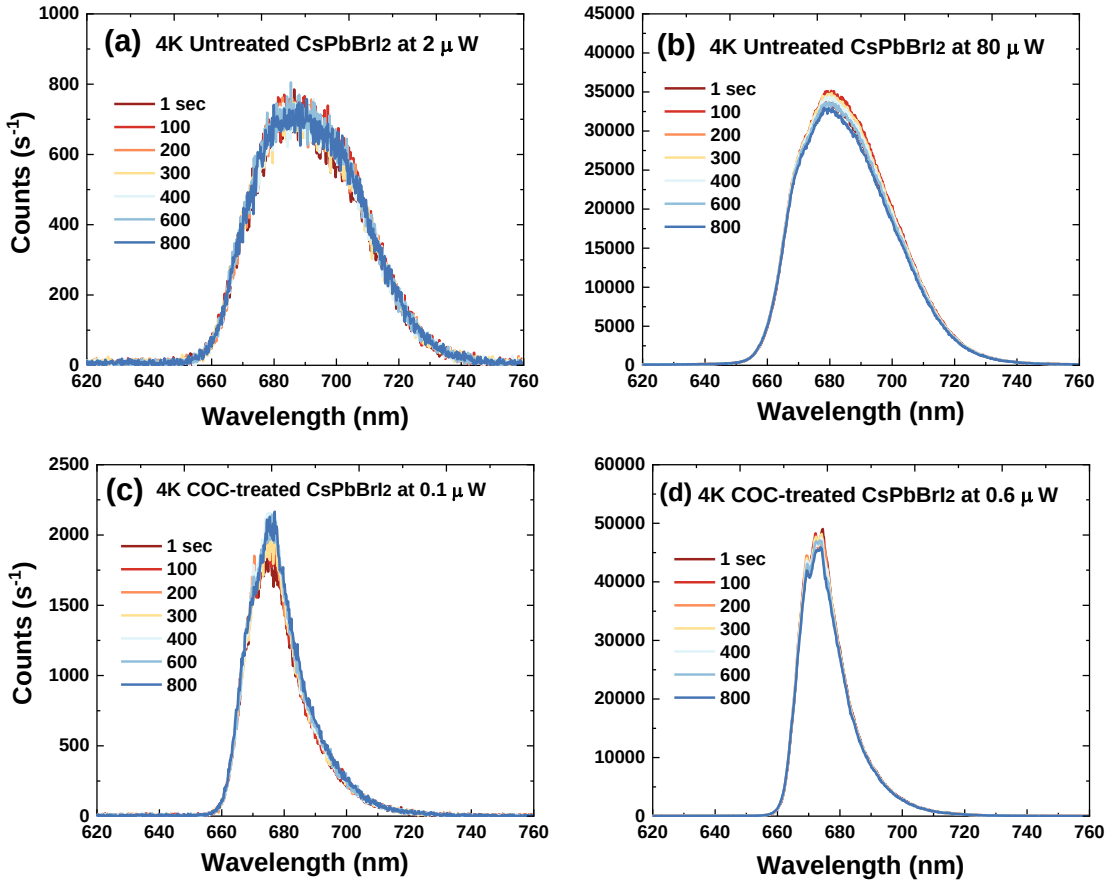

Figure 4.6: Cryogenic (4.2 K) PL time-series for $CsPbBrI_2$ films without COC and with COC treatment at low and high excitation powers of (a) untreated $CsPbBrI_2$ films at 52 μW, (b) pure $CsPbBrI_2$ films at 80 μW, (c) COC -treated $CsPbBrI_2$ films at 0.1 μW and (d) COC-treated $CsPbBrI_2$ films at 0.6 μW.

for both excitation intensities. This suggests that COC leads to increased halide mixing and electronic transition homogeneity whilst the electron-phonon coupling strength becomes weaker compared to untreated films [124]. With regards to the PL peak centre, the untreated $CsPbBrI_2$ films showed a redshift of 55 nm from 630 nm at RT to 685 nm at 4.2 K, while COC-treated $CsPbBrI_2$ films exhibit a smaller redshift of 30 nm from 645 nm at RT to 675 nm at 4.2 K. Unlike traditional II-VI chalcogenides, the all-inorganic perovskite materials exhibit a blue shift in PL emission with increasing temperature to 290 K [124, 125].This might refer to the fact that the interplay between the electron-phonon renormalization and the thermal expansion has a reverse impact on the band-gap energy. It is not expected to have any impact on phase segregation [125, 126].

Interestingly, the intensity of PL emission was increased without showing halide demixing with increasing the excitation intensity for untreated and the COC-treated films in Figures 4.6(b) to 4.6(d), confirming the entropic preference for halide mixing.

4.6 Time resolved photoluminescence measurements for untreated and COC-treated $CsPbBrI_2$ films

It has been suggested that when the grain size is equal to or larger than 46 ± 7 nm [115], the grain size can exceed the diffusion length. However, if the grain size is smaller than the threshold value, the electron and hole are confined and recombine radiatively [87, 115]. To support the comparability between the grain size and charge diffusion length (L), TRPL measurements were used for both films at room and cryogenic temperatures. Figures 4.7(a) and 4.7 (b) represent the TRPL spectra fitted by two and three exponential decay functions for samples at RT and 4.2 K, respectively, corrected for the instrument response function of our detection system to evaluate the excitation and recombination processes.

$$f(t) = A_1 \exp(-t/\tau_1) + A_2 \exp(-t/\tau_2) + A_3 \exp(-t/\tau_3) + y_0 \tag{4.1}$$

where τ_1 refers to short-lived PL emission contributing to band-edge exciton recombination, and τ_2 and τ_3, represent the long-lived lifetime attributed to trapping states arising from recombination in $CsPbBrI_2$ films with a photoinduced trapped pathway [124]. The fitted TRPL decay parameters are summarised in Table 4.1. The PL lifetime was found to be short in the untreated $CsPbBrI_2$ with $\tau_1 = 0.49$ ns and $\tau_2 = 2.8$ ns resulting from fast charge funnelling into I-rich phases [127] as also confirmed as will be revisited and discussed in Figures 4.8 (a) - 4.8(b) in the following section. In contrast, COC-treated $CsPbBrI_2$ exhibited a longer lifetime within $\tau_1 = 4.28$ ns and $\tau_2 = 10.67$ ns, indicating COC-limiting charge funnelling into I-rich phases and defect-filling effects [116]. This means that the electrons/holes diffuse with their diffusion length in the untreated film (180 nm) while they are confined in grains in the COC-treated films (61 nm), which was also observed by Hu and Gualdrón-Reyes [87, 115]. In light of observations based on thermodynamics in [128] and strain models in [65, 109] the initial ion distribution of $CsPbBrI_2$ films seems relatively homogeneous under prolonged illumination, generating

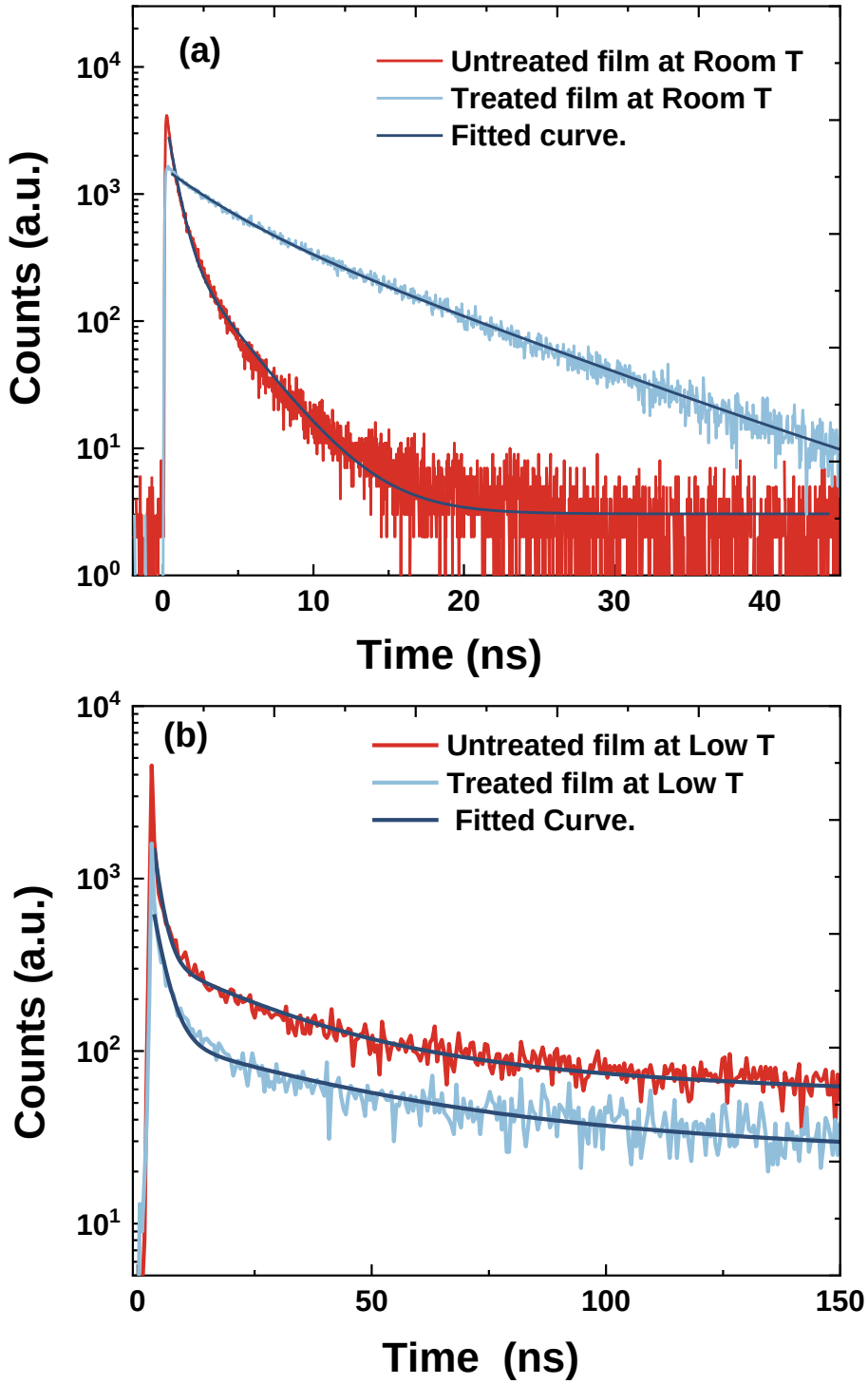

Figure 4.7: Time-resolved PL spectroscopy for $CsPbBrI_2$ thin films at an excitation wavelength of 400 nm and laser power intensity 20 μW (a) RT untreated and COC-treated $CsPbBrI_2$ films and (b) 4.2 K untreated and COC-treated $CsPbBrI_2$films.

holes and electrons, which quickly recombine, leading to PL emission. However, it is conjectured that the weakly bound electron and hole might dissociate, travelling with a long lifetime, causing lattice deformation through phonon coupling (polaron) and inducing halide anion redistribution. In other words, the imbalance of the Pb/I ratios on the $CsPbBrI_2$ film surface generates halide vacancies or undercoordinated Pb^{2+}, Cs^{+}, and I^{-} ions, increasing the chance of redox reactions. In this regard, the COC polymer matrix strongly interacts with Pb^{2+} to cover the perovskite surface/grain boundaries, improving the stability of $CsPbBrI_2$ films and, therefore, reducing the iodine vacancies and suppressing the halide ion mobility in $CsPbBrI_2$ films. Thus, the passivation process involving COC not only resulted in interaction with unliganded Pb^{2+} ions, leading to a reduction in surface defect density but also exerted control over the mobility of I^{-} ions on the surface of $CsPbBrI_2$. As a result, the I/Pb ratio on the surface approached the stoichiometric ratio [129].

Our finding is in agreement with the previous report that observed that the trapped state density decreased from 8×10^{16} to $6.64 \times 10^{16}\,cm^{-3}$ after adding a $Pb(NO_3)_2$ methyl acetate solution to $CsPbBrI_2$ films [130]. Similarly, the PL lifetime in $CsPbI_xBr_{3-x}$ increased from 7.5 to 12.1 ns after 6TIC-4F treatment confirming that non-radiative recombination was significantly suppressed [131]. Moreover, lifetime decay in BaI_2:$CsPbBrI_2$ was prolonged from 2.01 to 16 ns, due to the suppression of non-radiative recombination pathways [132]. It is also worth noticing that the grain boundaries (GBs) are sensitive places with higher defect concentration and non-radiative recombination, which disturb charge carrier movements (carrier mobility) by creating scattering centres and barriers. However, the increase in the number of GBs due to a reduction in the grain size after passivation with COC can improve $CsPbBrI_2$ film charge carrier separation, free carrier density, collection, and then, ultimately, the flow enhancement of the local current. The increased number of GBs can also dissociate exciton states (electron-hole pairs) and then generate more free-charge carriers, which in turn strongly influence the performance of perovskite-based optoelectronic devices. Yang et al. found that GBs have equivalent or slightly longer PL lifetimes than perovskite film interiors/surfaces, suggesting that GBs are not dominating non-radiative recombination centres [133]. In perovskite films,

Yun et al. identified increased current collection in the vicinity of GBs, which they ascribed to enhanced carrier transport and separation along the GBs as well as downward band bending [134]. In a similar trend, Ciesielski et al. discovered that PL lifetime decay was delayed in regions adjacent to the GBs due to carrier reflection in the areas close to the GBs [135].

Interestingly, however, both the excitonic state lifetimes τ_1 and the charge trapping state lifetimes τ_2 for both films become much longer at 4.2 K than at room temperature, possibly due to suppression of polaron formation [136]. It is also worth noting that both the short- and long-lived lifetimes of COC-treated $CsPbBrI_2$ films increased by a factor of ~ 3 over untreated $CsPbBrI_2$ films, where COC can decelerate ion migration by increasing the activation energy barrier, reducing non-radiative relaxation processes and passivating trapped states [109, 117, 137], taking into account that at lower temperatures the overall free energy is low due to the entropic stabilization. In contrast, at higher temperatures, the enthalpy of electronic states tends to change, leading to increases in the polaron formation density [124, 138, 139]. The reduction of the lattice distortion at 4.2 K tends to lower strain energy and produce fewer halide vacancies, leading to charge carrier localization into the self-trapped states and enhanced PL intensity, as shown in Figure 4.6(a)-3.6(d). The increase in the total free energy that stems from band gap differences, a funnelling and accumulation of photo-excited holes into the I-rich phase, a gradient strain accumulation caused by ion migration and lattice distortion were sufficiently inhibited in the COC-treated $CsPbBrI_2$ films at both temperatures as seen in figures 4.3(c)- 3.6(d) and figure 4.6(c)-3.6(d). For this reason, we expect that COC can improve the thermodynamic and kinetic stabilization by filling the surface defects in the $CsPbBrI_2$ films, optimizing grain size, lowering halide vacancy density, and reducing trap states, which help to minimize the rapid recombination of charge carriers with efficient charge transport in perovskite solar cells application [102, 103]. Therefore, the increase in lifetime decay and the PL intensity improvement for the COC-treated $CsPbBrI_2$ films at both temperatures indicates that COC can effectively inhibit non-radiative recombination induced by trapped states in the untreated $CsPbBrI_2$ films [123].

Film	τ_1 (ns)	A_1	τ_2 (ns)	A_2	τ_3 (ns)	A_3
RT $CsPbBrI_2$	0.49 ± 0.02	3.48 ± 0.06	2.84 ± 0.08	0.57 ± 0.04	-	-
RT $CsPbBrI_2$ with COC	4.28 ± 0.33	0.69 ± 0.05	10.67 ± 0.28	0.57 ± 0.05	-	-
4.2 K $CsPbBrI_2$	23.3 ± 8.0	2.72 ± 0.39	5420 ± 750	0.055 ± 0.007	384 ± 160	0.38 ± 0.12
4.2 K $CsPbBrI_2$ with COC	74 ± 5.7	3.86 ± 0.25	8000 ± 900	0.097 ± 0.011	734 ± 77	0.372 ± 0.06

Table 4.1: Time decay of a $CsPbBrI_2$ thin film and COC-treated $CsPbBrI_2$ films fitted by three exponential decay functions corrected for the instrument response function of our detection system to evaluate the excitation and recombination processes.

4.6.1 Time-resolved PL spectroscopy before and after phase segregation

To understand the effect of bandgap difference between the initial and segregated phase, we study room temperature time-resolved PL measurements for untreated $CsPbBrI_2$ films and COC-treated $CsPbBrI_2$ films after being exposed to continuous illumination of 532 nm with 40 minutes as illustrated in Figures 4.8 (a)- 4.8(b). It is apparent in the table 4.2 that lifetime decay of the COC-treated $CsPbBrI_2$ films exhibited a longer lifetime decay compared to untreated $CsPbBrI_2$ films due to the blocking effect of charged carriers' movements through COC treatments. Therefore, after films were treated , the COC treatment can inhibit charge funnelling and decrease charge carrier density within I-rich domains on the recombination dynamics [127].

Sample name	τ_1 (ns)	redA_1
Untreated $CsPbBrI_2$ film at 648 nm within 0 minutes	0.423	9281
Untreated $CsPbBrI_2$ film at 648 nm within 40 minutes	0.39	9989
Untreated $CsPbBrI_2$ film at 690 nm within 40 minutes	0.41	2574
COC-treated $CsPbBrI_2$ film at 645 nm within an initial minute	9.45	161
COC-treated $CsPbBrI_2$ film at 648 nm within 40 minutes	11.15	630.1
COC-treated $CsPbBrI_2$ film at 675 nm within 40 minutes	10.76	414

Table 4.2: TRPL spectra fitted by single exponential decay functions of untreated $CsPbBrI_2$ films and COC-treated $CsPbBrI_2$ films before and after phase segregation at room temperature.

4.7 Temperature dependence of TRPL for COC-treated $CsPbBrI_2$ films

To investigate the temperature-dependent PL decay dynamics of COC-treated $CsPbBrI_2$ films, TRPL spectra at temperatures from 10 to 290 K were measured, as shown in

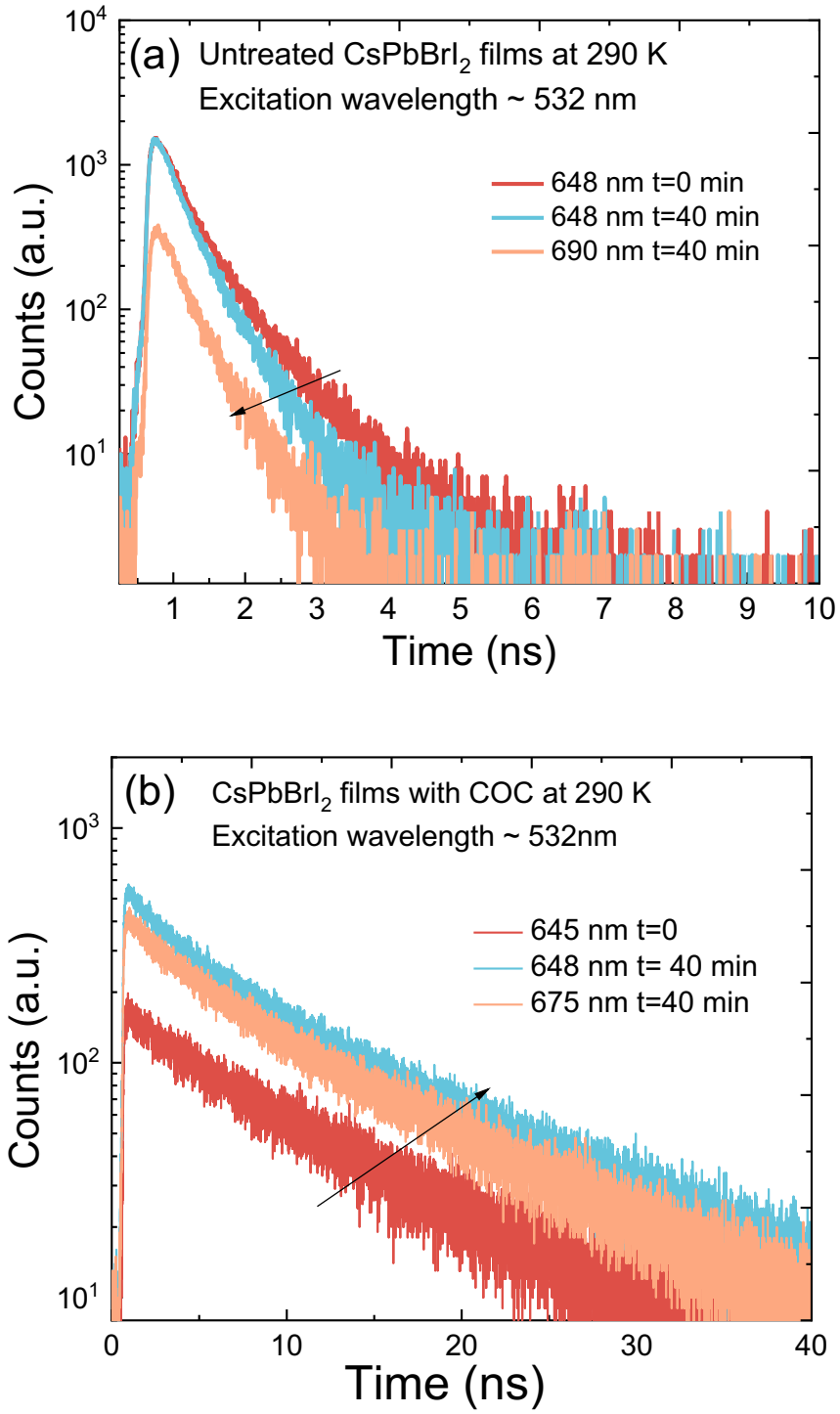

Figure 4.8: Room temperature time-resolved PL spectroscopy before and after phase segregation for a $CsPbBrI_2$ thin film at an excitation wavelength of 532 nm (a) TRPL of the untreated $CsPbBrI_2$ films with laser power intensity 90 μW and 11 MHz leaser repetition rate (b) TRPL of the COC-treated $CsPbBrI_2$ films with laser power intensity 10 μW and 11 MHz laser repetition rate.

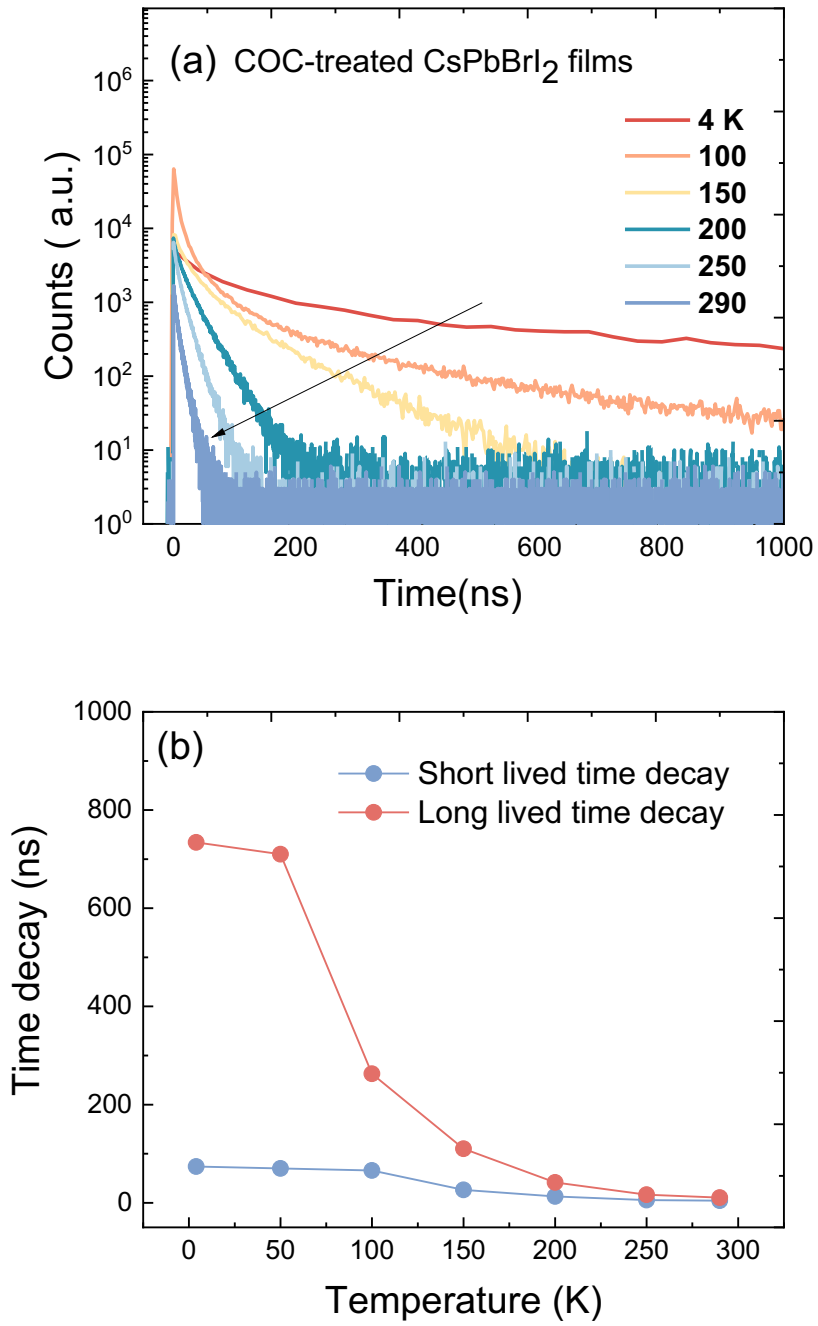

Figure 4.9: Temperature dependent time resolved photoluminescence spectra of the COC-treated $CsPbBrI_2$ films at 200 μW under excitation with a 400 nm laser.

Figures 4.9(a)-4.9(b). A multiexponential decay function, as described in equation (4-1), is used for fitting parameters of the decay times of COC-treated $CsPbBrI_2$ films as a function of the temperature using a pulsed laser operating at 405 nm with the excitation intensity of 2 μW was shown in Table 4.3. The weights of the fast and slow decay components are represented by A_1 and A_2, respectively, while the times of the components are represented by τ_1, τ_2 and τ_3. The fast decay components are more likely to derive from the direct recombination of excitons. In contrast, the slow decay components can arise from trap-assisted recombination, usually affected by exciton-phonon interaction and defect state density. It worth noticing that when the temperature was close to room temperature 290 K, the lifetime of the excitonic state τ_1 slightly decreased. In contrast, the charge trapping state τ_2 and τ_3 and dramatically reduced due to the enhancement of exciton- phonon coupling.

Sample name	τ_1 (ns)	A_1	τ_2(ns)	A_2	τ_3(ns)	A_3
COC-Treated $CsPbBrI_2$ 4.2 K	74 $\pm$ 5.7	3.86 $\pm$ 0.25	8000 $\pm$ 900	0.10 $\pm$ 0.01	734 $\pm$ 77	0.73 $\pm$ 0.60
COC-Treated $CsPbBrI_2$ 100 K	7.3 $\pm$ 2.3	33 $\pm$ 5.7	50.6 $\pm$ 9.5	5.7 $\pm$ 1.4	395 $\pm$ 30	0.35 $\pm$ 0.05
COC-Treated $CsPbBrI_2$ 150 K	26 $\pm$ 1.3	4.77 $\pm$ 0.11	110.1 $\pm$ 1.8	1.20 $\pm$ 0.05	-	-
COC-Treated $CsPbBrI_2$ 200 K	10.32 $\pm$ 0.44	2.61 $\pm$ 0.07	29.90 $\pm$ 0.25	2.97 $\pm$ 0.07	-	-
COC-Treated $CsPbBrI_2$ 250 K	5.50 $\pm$ 0.13	3. 03 $\pm$ 0.07	16.50 $\pm$ 0.20	2.66 $\pm$ 0.07	-	-
COC-Treated $CsPbBrI_2$ 290 K	4.28 $\pm$ 0.33	0.68 $\pm$ 0.05	10.68 $\pm$ 0.28	0.58 $\pm$ 0.05	-	-

Table 4.3: Fitting parameters of the decay times of COC-Treated $CsPbBrI_2$ films as a function of the temperature using a pulsed laser operating at 405 nm and fixed excitation intensity of 2 μW.

It has been indicated that the PL of inorganic mixed halide perovskites is produced by the emission resulting from excitonic and trapping states [124]. Since the short-lived excitonic state at high energy depends on temperature and probe wavelength, on the other hand, the long-lived trapping state at lower energy can be attributed to the defects originating from lattice distortion or mismatching and energy transfer because of the size distribution. For this reason, it is imperative to measure the temperature-dependent PL of COC-treated $CsPbBrI_2$ films at different temperatures, which can help understand the effect of passivation methods on the charge carrier dynamics for designing all-inorganic perovskite solar cells and more advanced optoelectronic applications.

4.8 Conclusion

Surface passivation is an essential method employed in mixed halide perovskites to reduce grain boundary recombination and surface defects. Through the efficient passivation of surfaces, it is possible to decrease the recombination rates of charge carriers, thereby resulting in enhanced optoelectronic properties and device efficacy. This chapter examined the validity of such passivation strategies and the extent to which they can mitigate instability through the passivation of trap states using cyclic olefin copolymer (COC) treatment. Based on thermodynamic and kinetics models, the results clarified the main different contributions that induce phase segregation in the untreated thin films and COC-treated thin films of $CsPbBrI_2$ mixed halide perovskites. The microscopic processes occurring during halide segregation in $CsPbBrI_2$ films using combined spectroscopic measurements at room and cryogenic temperatures was investigated. The passivation strategy for mitigating the halide migration of Br/I ions in the films by overcoating with cyclic olefin copolymer (COC) was Put forward. The study probed experimentally the role of the energy barrier on halide migration, limiting lattice strain and polaron formation and mitigating trap states. Room- temperature X-ray Characterization (XRD) showed that COC treatment films optimized the grain size in the threshold size range between 168 to 47.33 nm. Temperature-dependent micro-photoluminescence (PL) spectroscopy confirmed that the activation energy barrier of ion migration increased from 20 to 28 meV. Besides, room temperature time-dependent PL profiles for increasing excitation intensities exhibited that the excitation threshold intensity induced phase-segregation was decreased from 400 μW to 60 μW. Furthermore, the band gap difference between the initial and final halide phases was decreased in which the charge carrier density that is funnelled and accumulates at the I-rich phase is slowed down. In addition, the dominance of the entropy demixing halide ions driven by the kinetics of halide vacancy and polaron accumulation was reduced after $CsPbBrI_2$ thin film being coating with COC.

Furthermore, cryogenic- temperature (4.2 K) time-dependent PL profiles for increasing excitation intensities was tracked, where less thermal lattice distortion was expected to be occurred, thereby lower polaron formation. The results showed that the entropy

remixing halide ions and higher photostability against phase segregation was dominant at cryogenic temperatures (4.2 K) compared to room temperature results. Interestingly, the intensity of PL emission was increased without showing halide demixing with increasing the excitation intensity for untreated and the COC-treated films, confirming the entropic preference for halide mixing. In addition, the $CsPbBrI_2$ films treated with COC demonstrated a reduced electron-phonon coupling strength and a blue shift of 5 nm at both excitation intensities. This was attributed to the enhanced halide mixing and electronic transition homogeneity resulted by the COC, which contrasted with the untreated films. The results were further supported by time-resolved PL spectroscopy for $CsPbBrI_2$ thin films, and the effects of the passivation method on the charge carrier dynamic were investigated. At room temperature, the PL lifetime of untreated $CsPbBrI_2$ films was shorter due to the rapid charge funnelling into I-rich phases. On the contrary, COC-treated $CsPbBrI_2$ exhibited a longer lifetime, indicating COC-limiting charge funnelling into I-rich phases and defect-filling effects.

On the other hand, at 4.2 K, the excitonic state lifetimes (τ_1) and the charge trapping state lifetimes (τ_2) of both films are significantly extended compared to room temperature, because of the inhibition of polaron formation. Furthermore, in comparison to untreated $CsPbBrI_2$ films, both the short-lived and long-lived lifetimes of COC-treated films increased by a factor of approximately 3. This was because COC inhibited ion migration by increasing the barrier to activation, decreasing non-radiative relaxation processes, and passivating trapped states. The findings demonstrated a comprehensive analysis and clarified observation regarding how COC enhanced the thermodynamic and kinetic stabilization of $CsPbBrI_2$ films through various means: grain size optimization, halide vacancy density reduction, trap state reduction, and surface defect filling. These improvements contributed to the mitigation of rapid charge carrier recombination, thereby facilitating efficient charge transport and free carriers in the application of perovskite solar cells.

5

Inhibiting the Appearance of a Green Glow in Mixed Lead Halide Perovskite Nanocrystals for Pure Red Emission

Contents

5.1 Introduction

Recently, metal halide perovskites have emerged as promising candidates for light-emitting diodes (PeLEDs). The current record efficiencies of perovskite LEDs (PeLEDs) exceed 30% for green emission [140], 25% for red emission [141, 142] and 10% for blue emission [143]. Among the different types of perovskite emitters, all- inorganic lead halide perovskites show unique advantages such as tunable emission wavelengths through halide mixing [144], narrow line widths[145], high brightness[146] and high color purity [147], that can be excellent candidates for next generation (PeLEDs).

Mixed-halide perovskites with a composition such as $CsPbI_2Br$ can easily attain a pure red emission by adjusting the halide ratio of (Br/I). However, a major caveat of these materials is halide separation whereby compositional instability is induced on the excitation of charge carriers through photoabsorption or current injection [148]. This results in spatial separation of the halide species into distinct domains of different bandgaps and a corresponding shift in the emission wavelength. Particularly in bulk films, iodide-rich regions form low-bandgap domains where the excited charge carriers funnel and collect, leading to red-shifted emission. This is often observed to be taking place at the grain boundaries. On the contrary, in PNCs, this emission peak shift is towards the blue implying predominance of the bromine-rich emissive regions instead. This is because the bond-breaking and subsequent escape of iodide ions from within the PNC is energetically favourable with the Pb-Br bond being shorter and having much higher ionization energy than the Pb-I bond. It has been shown that much like in bulk films, the iodide ion in PNCs migrates away from the point of illumination/injection to adjacent sites due to Coulombic repulsion [149].

Several theoretical models have been suggested to understand such phenomena based on thermodynamic and kinetic perspectives [150]. Amongst these models, the role of halide oxidation can rationally explain the observed halide segregation in nanocrystal and thin-film perovskites [78]. Upon illumination, I/Br mixed perovskites undergo preferential iodide oxidation, resulting in local concentration gradients of oxidized products (e.g., I_2 and I_3^-) and driving halide migration [78, 79, 151]. Moreover, under continuous

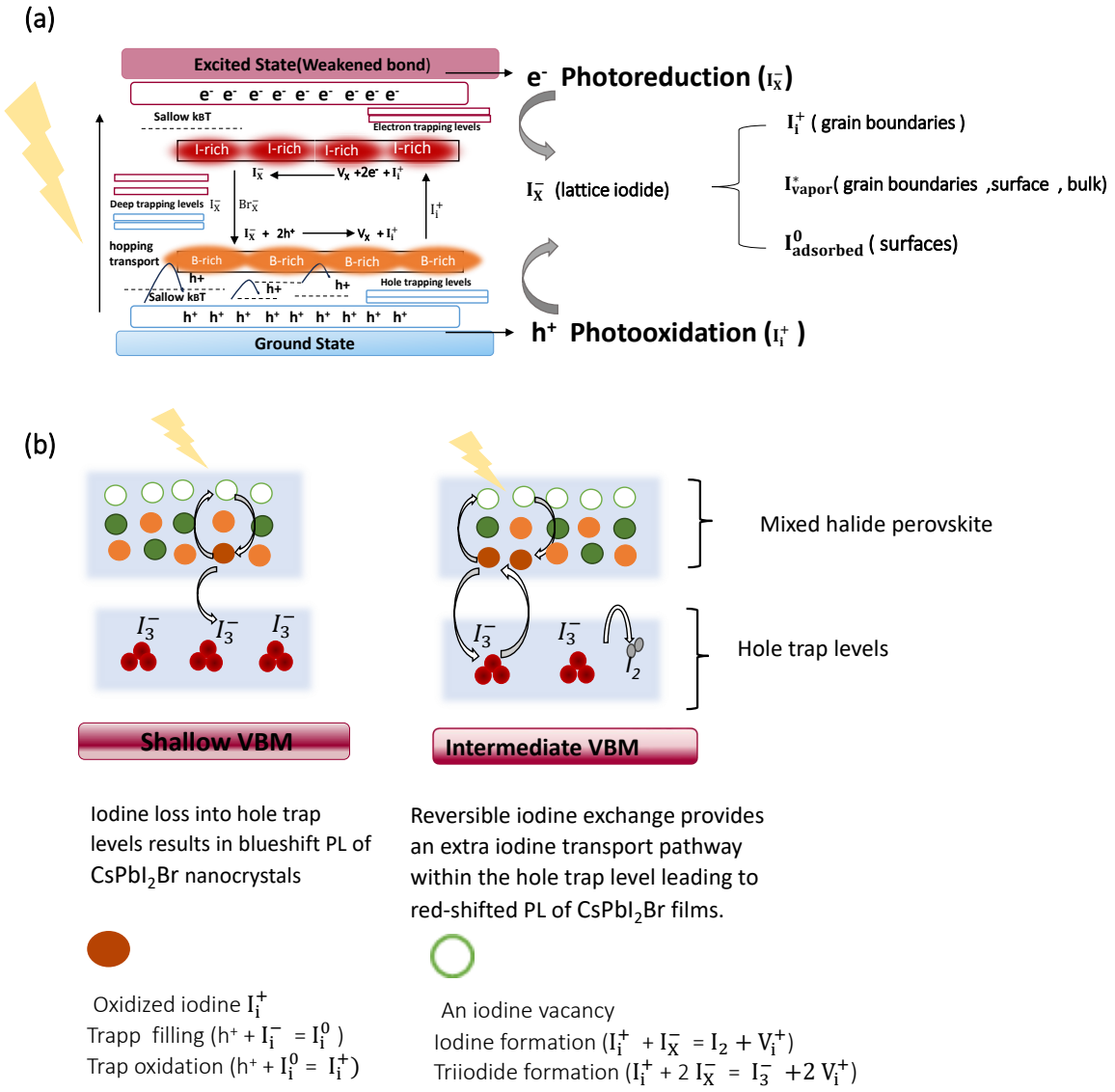

Figure 5.1: (a) Schematic illustrating the photoinduced halide oxidation mechanism for mixed halide perovskites in the form of $CsPbI_2Br$ nanocrystals and thin films. The photogenerated holes ($2\ h^+$) oxidize the lattice iodide ions (I_x^-), leading to the formation of iodine (I_2) and/or triiodide (I_3^-), either in the bulk (I^*) or at surfaces (I^0) [78]. If it forms in bulk, the (I_2) migrate faster and are then expelled from the lattice, where uncoordinated Pb^{2+} and Cs^+ ions accumulate at the nanocrystal surface. Meanwhile, the lattice bromine ions (Br_x^-) drift or diffuse into the Br-rich region and reconstruct the $CsPbBr_3$ instead of photo-decomposition due to a higher oxidation potential than for the lattice iodide (I_x^-).(b) Schematic illustrating the photoinduced halide oxidation mechanism of mixed halide perovskites in the form of $CsPbI_2Br$ nanocrystals and $CsPbI_2Br$ thin films.

illumination as shown in figures 5.1 (a)-(b), Pb^{2+} ions in perovskites are likely to be reduced to metallic Pb^0, lowering the efficiency of the devices.

5.2 Structure and Growth

5.2.1 Nanocrystal Synthesis

Growth of nanocrystals and film fabrication were undertaken by collaborators Ashley Marshall and Shaoni Kar in the University of Oxford in Professor Henry Snaith's lab. PbX_2 powder (0.2 mmol), CsX powder (0.2 mmol), OA (0.5 mL), OAm (0.25 mL) and DMAI (for the A-site modified NCs) were added to 5 mL of dimethylacetamide (DMAc) and stirred to dissolve for 60 mins at room temperature. A portion (3 mL) of the obtained mixture was swiftly injected into 30 mL chlorobenzene or chloroform under vigorous stirring. After stirring, the resulting solution was mixed with methyl acetate in a 1:2 ratio (v/v) and centrifuged for 5 min at 7500 revolutions per minute (rpm). After centrifugation, the supernatant was discarded, and the precipitate was dispersed in hexane. Stable CsPbI2Br NC ink ($\sim$10 mg mL^{-1}) was obtained by removing larger particles after centrifuging the crude dispersion for 5 min at 3000 rpm. Further washing (repetition of fast and slow centrifugation steps) can be done for device application.

5.2.2 Film Fabrication (solution processing)

The ITO substrates underwent a cleaning process involving sequential sonication in DECON-90, DI water, acetone, and IPA for a duration of 15 minutes each. Following that, the substrates were subjected to UV-ozone treatment for a further 15 minutes. The films utilized for fundamental characterisation and devices were fabricated using the spin-coating technique on ITO/PEDOT:PSS substrates. The PEDOT:PSS solution was subjected to a spin-coating process in ambient conditions, with a rotation speed of 5000 rpm for a duration of 40 seconds. Subsequently, the coated film was subjected to annealing at a temperature of 150 C° for a period of 12 minutes. Afterwards, the specimen was transferred to the glovebox antechamber and left to undergo a drying process for a duration of 20 minutes. Then, NC ink was spin-coated for 40 seconds at 1500 rpm in the glovebox. Any residual solvent was evaporated at 50 C° for a duration of 10 minutes.

5.3 The Optical Characterisation $CsPbI_2Br$ nanocrystals and $CsPbI_2Br$ thin films

We synthesized the $CsPbI_2Br$ PNCs and $CsPbI_2Br$ thin films and encapsulated them with COC by depositing perovskite precursors on glass substrates using spin-coating; all synthesis details and characterization methods are described in experimental section. The absorption and PL spectra of pristine $CsPbI_2Br$ PNCs and $CsPbI_2Br$ thin films are presented in Figure 5.2(a) and 5.2(d). The exciton absorption and PL emission peaks of $CsPbI_2Br$ PNCs showed a slight blue shift compared to $CsPbI_2Br$ thin films. In comparison to thin films, the exciton absorption and PL emission peaks of $CsPbI_2Br$ PNCs exhibited a marginal blue shift. The HRTEM images in Figures 5.2(b) - 5.2(c) revealed a homogeneous distribution with an average particle size of 11.3 nm for $CsPbI_2Br$ PNCs. The SEM image in Figures 5.2(e) - 5.2(f) also confirmed homogeneous distribution with an average particle size of 450 nm for $CsPbI_2Br$ thin films.

5.4 X-ray diffraction (XRD)

To understand the link between the properties of the nanocrystals and thin films regarding their inhomogeneous charge-carrier distribution and structural/compositional rearrangement, X-ray diffraction (XRD) was implemented utilizing a Panalytical X'Pert Pro X-ray diffractometer that was equipped with a Cu-alpha source at a wavelength of 1.54 Å. The (XRD) data of the pristine and COC-encapsulated $CsPbI_2Br$ nanocrystals and thin films before and after 50 minutes of 400 nm illumination were undertaken by a collaboration with Shaoni Kar from the laboratory of the University of Oxford Professor Henry Snaith as shown in Figures 5.3(a) to 5.3(c).

As mentioned in previous reports [78, 152], iodide ions (I^-) exhibit photosensitivity and can readily oxidized to form I_2 in the precursor solution. These factors form non-stoichiometric and iodide-vacancy defects (V_I) in the synthesized perovskites. In order to assess the efficacy of COC in inhibiting iodide oxidation without any potential issues related to the creation of colloidal PbI_2 particles, we examined the durability of $CsPbI_2Br$ PNCs and thin films, as well as their encapsulated counterparts. Figures 5.3(a) - 5.3(c)

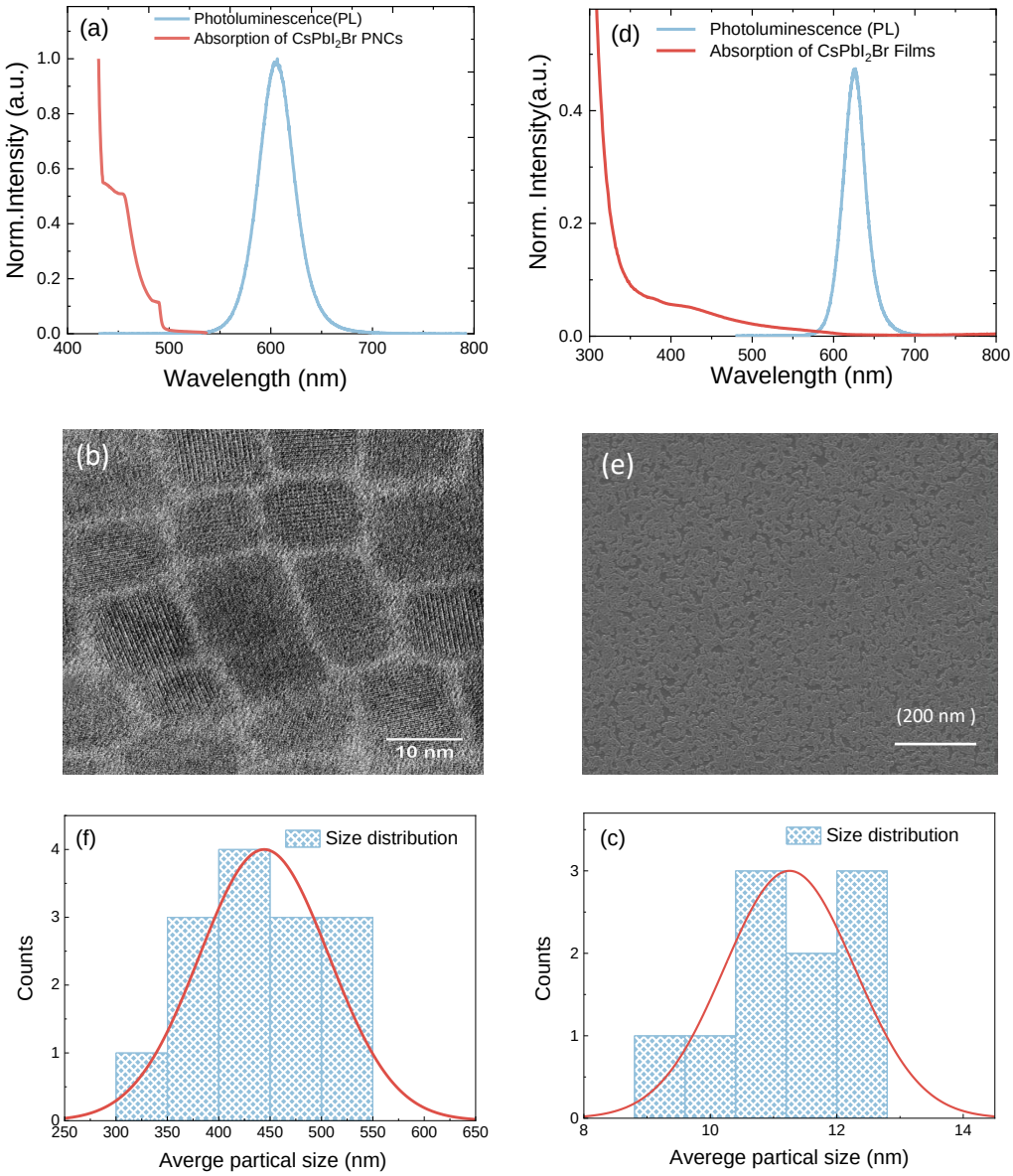

Figure 5.2: (a) UV-vis absorption spectra and PL spectra of $CsPbI_2Br$ PNCs, (b) Transmission Electron Microscope (TEM) images of $CsPbI_2Br$ PNCs, (c) Size distribution of $CsPbI_2Br$ PNCs from TEM images (the size = 11.30 nm), (d) UV-vis absorption spectra and PL spectra of $CsPbI_2Br$ thin films, (e) Scanning Electron Microscope (SEM) images from $CsPbI_2Br$ thin films with (f) A grain size distribution with around 450 nm. Growth of nanocrystals and film fabrication were undertaken by collaborators Ashley Marshall and Shaoni Kar in the University of Oxford in Professor Henry Snaith's lab.

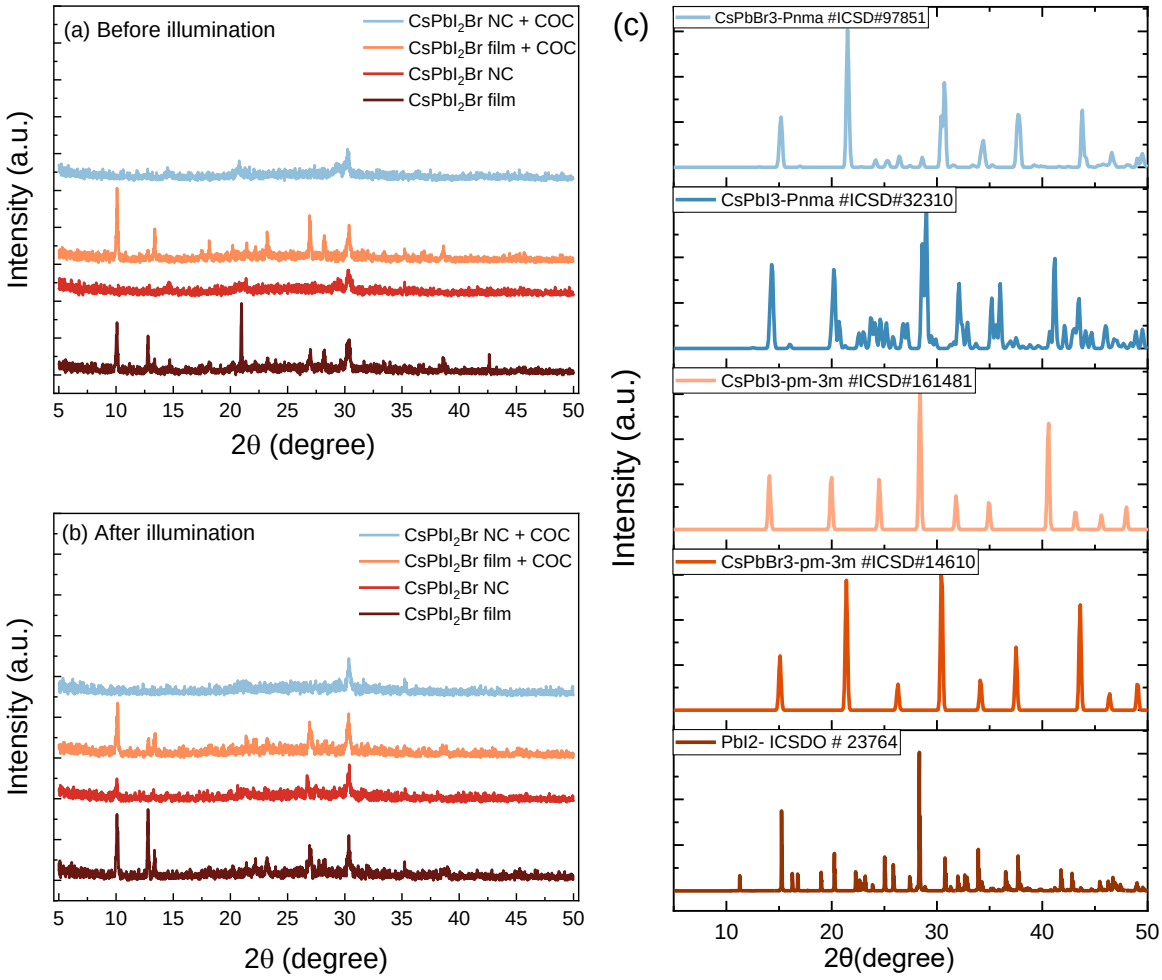

Figure 5.3: (a) XRD patterns of the $CsPbI_2Br$ PNCs and film counterparts before 50 minutes of 405 nm illumination with an average power density of 3180 Wcm^{-2} (b) XRD patterns after samples being encapsulated with COC. (c) The reference patterns of the orthorhombic, cubic, and tetragonal phases of $CsPbBr_3$ and $CsPbI_3$ obtained in the Inorganic Crystal Structure Database (ICSD).

represented the X-ray diffraction (XRD) patterns the fresh and aged $CsPbI_2Br$ PNCs and thin films with encapsulated samples at 405 nm excitation wavelength and 3180 Wcm^{-2} CW laser optical power density. From XRD measurements, no peaks associated with PbI_2 or other impurities were observed from the $CsPbI_2Br$ PNCs (without / with COC), indicating that the crystal quality is conserved. On the other hand, the $CsPbI_2Br$ thin films (without / with COC) showed that the predominated $CsPbI_3$ and $CsPbBr_3$ phases, with a significant amount of PbI_2, which is indicative of the decomposition of CsI into Pb^0

and I_2. The highest XRD peak intensity and narrowest full width at half maximum in thin films were observed after the film was encapsulated with COC. Despite increased intensity, these films indicate that (COC) does not fully inhibit the formation of PbI_2 byproducts, such as $CsPbI_3$ and $CsPbBr_3$, as previously reported [153].

In the case of aged samples in Figure 5.3(b)- 5.3(c), the PNCs without COC were decomposed with a negligible amount of PbI_2. At the same time, the PNCs with COC were unchanged, indicating that the COC effectively inhibited the halide oxidation in air. In contrast, both thin films (without / with COC) exhibited a strong presence of $CsPbI_3$ with less amount of PbI_2 compared with the initial condition, indicating the 3D phase of I-rich domains. Thus, encapsulated $CsPbI_2Br$ PNCs with COC suppressed the impurity phase PbI_2 and promoted pseudo cubic perovskite structures, improving nanocrystal quality more than thin films.

5.5 Photoluminescence time series for pristine nanocrystals and thin films

The selective oxidation of halides with lower oxidation potentials ($I^- < Br^- < Cl^-$) is the crucial process for the movement of halide ions, which ultimately leads to the separation of different phases in perovskite materials 5.1 [78]. Accordingly, time-dependent photoluminescence was implemented to investigate the effect of COC on halide separation and purity of emission colour. Figures 5.4(a) - 5.4(b) show PL emission over 50 minutes of continuous illumination on $CsPbI_2Br$ PNCs and thin films at 405 nm excitation wavelength and an average power density of 3180 Wcm^{-2} CW laser. A uniform phase with an initial emission peak at 605 nm of $CsPbI_2Br$ PNCs was observed in Figure 5.4(a), indicating entropic stabilization of the mixed halide Br/I ions [40]. Following a 10-minute illumination, the green glow at 510 nm and red emission at 606 nm, along with decreasing PL intensity were emerged due to halide oxidation (eg. iodine) and ion migration [78, 79].

After 20-30 minutes, the intensity of red emission decreased, and green emission increased, with a slight blue shift of 2-3 nm. This indicates the gradual photochemical decomposition of iodine ions and iodine oxidation triggered by the loss of iodine from the lattice, leaving CsI and Pb behind [154, 155]. After 40 minutes, a distinct green emission

with a slight blue shift to 508 nm appeared, while the red emission decreased with a blue shift to 575 nm accompanied by a red emission at 685 nm. This trend confirms that $CsPbBr_3$ is less susceptible to oxidation compared to $CsPbI_2Br$ and $CsPbBI_3$, which is also a sign of iodine sublimation and tribromide phase formation. [79, 154]. Accordingly, the excess iodine (I^0) building up under prolonged illumination, which in turn sublimates as gas from the outermost to the innermost layer nanocrystals, enriching the surface with uncoordinated ions (Pb^{2+}/ Cs^+/ I^-). Under intense light illumination, a surface enriched with uncoordinated ions can continuously decompose as a green glow or reconstruct as a red emission by either photolysis or thermolysis [156] following the chemical path.

$$CsPbI_3 \rightleftharpoons I_2 + Pb + CsI \qquad (1)$$

In contrast,$CsPbI_2Br$ thin films in Figure 5.4(b) exhibited an initial redder emission peak at 625 nm due to a lower binding energy and weaker quantum confinement with an enlarged crystal size. Following a 10-minute illumination, the halide ions start migrating, and films separated into pure red emission at 625 nm and deep red (I-rich) emission at 700 nm regions, resulting in an inefficient energy transfer process. Unlike PNCs, the intensity of pure red emission decreased and deep red emission slightly increased, indicating that grain boundaries (GBs) in thin films impair the escape of iodine molecules as triiodide $I_2 + I^- = I_3^-$ and, thereby, affect the contribution of the hole trap states [151]. This can be also a sign of the reversible redox (I^-/ I_3^-) and (Pb^{2+}/ Pb^0) process followed by recombination of photogenerated carries at low energy to form the $CsPbI_3$ phase as represented in the chemical paths from (3) to (7), respectively. After a 50-minute illumination, the red emission intensity (I-rich) peaked and pure red emission intensity dropped, signifying the gradual depletion of I^- and spatial variation in iodide oxidation at grains, leading to the formation of $CsPbI_3$ phase [151, 157–159]. Note that photo-brightening of deep red emission can be attributed to higher photochemical reactions or photon energy above (a critical wavelength) $\sim$ 520 nm, while photodarkening occurs below this wavelength. Thus, thin films exhibit different halide oxidation processes, with Pb^0 and I_3^- defects migrating more vertically from the bulk to grain surfaces and grain boundaries than $CsPbI_2Br$ PNCs 5.1.

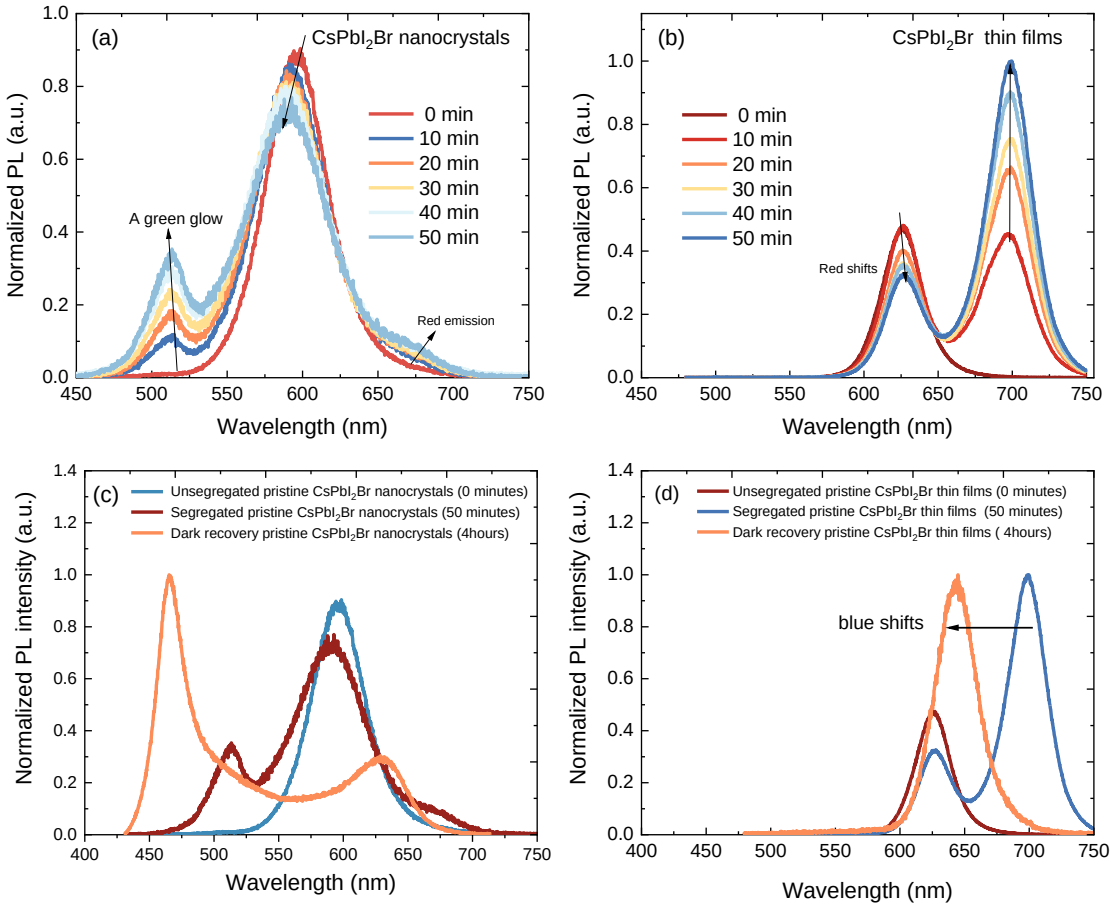

Figure 5.4: Light-induced phase separation of $CsPbI_2Br$ PNCs and thin films continuously excited by CW light at 405 nm with a laser power density of 3180 Wcm^{-2} within 0, 10, 20, 30, 40 and 50 minutes of illumination. (a) The evolution of PL for $CsPbI_2Br$ PNCs and (b) The evolution of PL for $CsPbI_2Br$ thin films. (c) and (d) The PL spectra for the initial, light-induced, and dark recovery states of both the pristine PNCs and the thin films, respectively. The initial spectrum is represented by the dark green line, the spectrum after 50 minutes of illumination is depicted by the brown line, and the spectrum after four hours of illumination and subsequent dark recovery is illustrated by the turquoise line.

$$3\,CsPbI_2Br \xrightarrow{light} CsPbBr_3 + 2\,Cs^+ + 2\,PbI_2 + I_2 + 2\,e^- \quad (2)$$

$$2\,PbI_2 \xrightarrow{light} 2\,Pb^{2+} + 4\,I^- \quad (3)$$

$$2\,Pb^{2+} + 4\,e^- \xrightarrow{light} 2\,Pb^0 \quad (4)$$

$$6\,I^- \xrightarrow{light} 4\,e^- + 2\,I_3^- \quad (5)$$

$$2\,Pb^0 + 2\,I_3^- \xrightarrow{light} 2\,PbI_2 + 2\,I^- + Heat \quad (6)$$

$$2\,Cs^+ + 2\,PbI_2 + 2\,I^- \xrightarrow{light} 2\,CsPbI_3 \quad (7)$$

The absence of a green glow in pristine thin films is due to the accumulation of Pb^0

and I_3^- defects, which increase the lattice energy of pristine thin films, and then diffuse to grain boundaries, forming an I-rich phase due to the presence of multiple surface defects in the thin film compared to nanocrystals (e.g. dangling bonds and uncoordinated (Pb^{2+} ions). This can further refer to the fact that the diffusion of both Pb^0 and I_3^- defects in thin films has a higher propensity to migrate from the bulk to the surfaces of grains and grain boundaries along a vertical pathway than pristine nanocrystals. The inter-diffusion rates for this migration range approximately between 10^{19} to $10^{20}\,m^2s^{-1}$ [160]. Specifically, upon prolonged illumination, the thin films decompose into CsI,PbI_2, and $PbBr_2$ which can passivate defects and grain boundaries to suppress the non-radiative recombination [158]. Mobile interstitial iodine (I_i) is attracted by charge carriers accumulated at low energy regions (I-rich domains), whereas the (Br_x^-) and (I^0/ I^-) interdiffuse to reduce lattice strain. In this regard, we deduce that the band gap difference between I-rich and Br-rich areas determines the threshold size or the intensity that causes phase segregation. In addition, the lattice strain determines the preferential direction for inter-diffusion of both charge carriers and the iodine mobility, which are responsible for final halide distribution.

To uncover the underlying mechanism leading to photo-oxidation and the imbalance of (Br/ I) ion migrations, we further traced the PL emission of PNCs and thin films after four hours of restoration in the dark. Figure 5.4(c) confirmed that $CsPbI_2Br$ PNCs subjected to an irreversible process of blue-shifted emission and increased green glow with iodine agglomeration, confirming I^- photooxidation and sublimation as I_2. In contrast, the reverse process was observed for $CsPbI_2Br$ thin films in Figure 5.4(d), resulting in a restored emission spectrum and complete bleaching of the low-energy band at 645 nm due to intermixing Br-rich and I-rich domains driven by entropy stabilization [151]. This can further prove that the total Gibbs free energy, ΔG_{total}, in the $CsPbI_2Br$ thin film is equally attributed to the bulk, ΔG_{bulk}, and the surface, ΔG_{surf}. In contrast, the surface free energy ΔG_{surf} dominates in ΔG_{total} the $CsPbI_2Br$ PNCs due to higher surface energy [161, 162].

$$\Delta G_{total} = \Delta G_{bulk} + \Delta G_{surf} \tag{11}$$

$$\Delta G_{total} = \frac{4}{3}\pi r^3 \Delta G_v + 4\pi r^2 \gamma \tag{12}$$

in which r represents the particle radius, ΔG_v is the crystal's free energy and γ is the surface tension.

5.6 Photoluminescence time series for encapsulated nanocrystals and thin films

To verify the effectiveness of passivation in inhibiting halide oxidation, we further performed measurements on the same samples after being encapsulated with COC. In Figures 5.5(a) - 5.5(b), the PL intensity increased with a slight redshift of 10-12 nm after PNCs being encapsulated. This can ascribed to a strong coupling involving energy transfer due to the interface effect between PNCs and COC [163]. Unlike pristine PNCs, COC-passivation massively inhibited phase separation in the $CsPbI_2Br$ PNCs and exhibited pure red emission at 615 nm under continuous illumination. The inhibiting of halide segregation here can be ascribed to the selective reduction of iodine (I^0) and oxidizes metallic (Pb^0) in a gradual manner [78, 153, 164]. Based on the XRD data presented in Figure 5.3(a) - 5.3(b), we suggest that COC inhibits the oxidation of iodide ions of PNCs, thereby decreasing the density of iodine-relevant defects, including iodine vacancies (V_I) and metallic Pb^0 [165, 166]. Similar to PMMA polymers, COC may passivate these defects, form an equilibrium with surface-bound ions and maintain charge neutrality instead of oxidization. It may also suppress the nearest neighbour hopping mechanism in mixed halide (Br/I) ions [167–170], which more likely occurs between adjacent lattice sites and halide vacancies (V_X) that serve as the pathway for halide migration [168, 170].

In contrast, Figure 5.5-(c) shows that $CsPbI_2Br$ films still showed phase separation after encapsulation, where an initial emission peak at 625 nm red-shifted with PL intensity reduction within 10-30 min. This can be attributed to an entropic destabilization where lattice strain energy in thin films is still higher due to the presence of multi-surface defects compared to PNCs [151] ; therefore, the Gibbs free energies (ΔG) for the half-reaction ΔG ($I^0 \rightarrow I^-$) and ΔG ($Pb^0 \rightarrow Pb^{2+}$) are not sufficiently reduced [151, 153, 164]. Although all perovskites have similar defects, reducing the grain size of perovskites to few nanometer can limit excited charge carrier spatial freedom, inhibiting the diffusion of halide ions into halide vacancies (V_X) in mixed halide perovskites [168, 171]. Moreover,

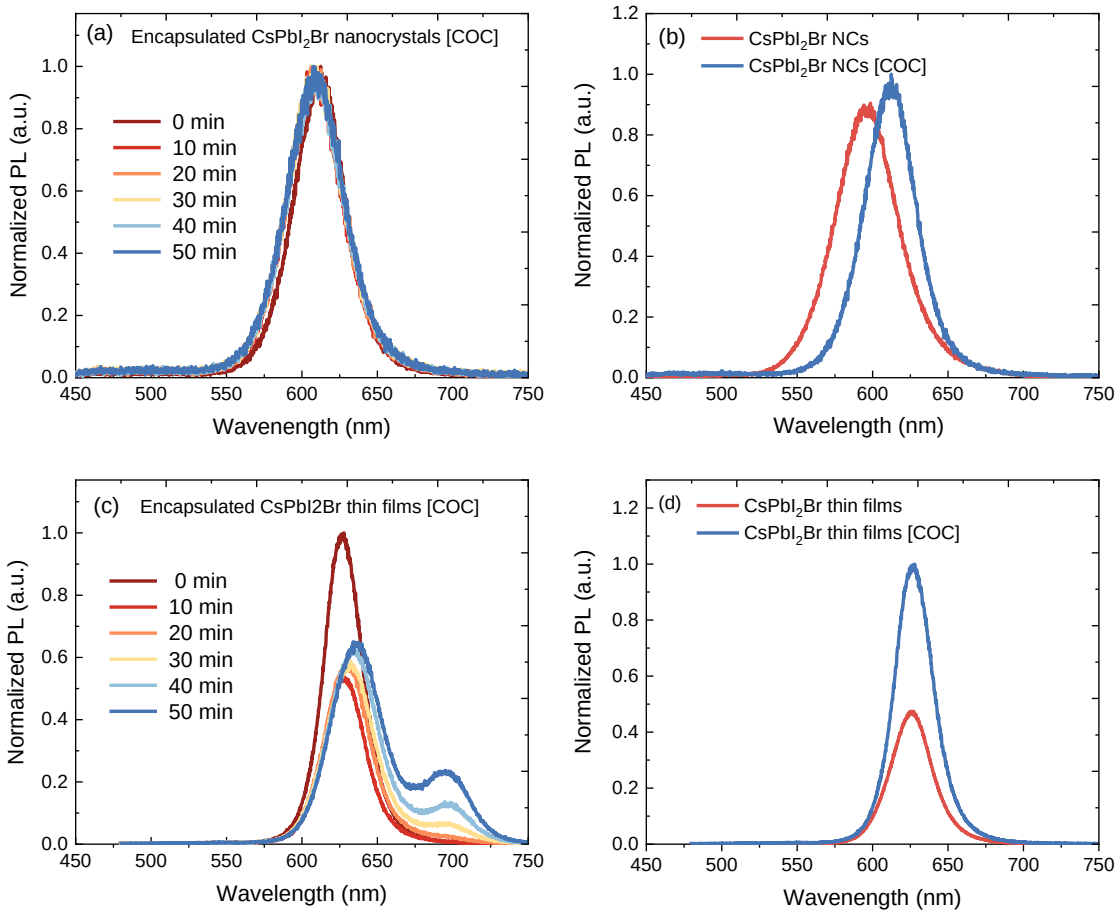

Figure 5.5: Light-induced phase separation of COC-Encapsulated $CsPbI_2Br$ PNCs and thin films continuously excited by CW light at 405 nm with a laser power intensity of 3180 Wcm^{-2} within 0, 10, 20, 30, 40 and 50 minutes of illumination. (a) The evolution of PL for COC-Encapsulated $CsPbI_2Br$ PNCs and (b) The evolution of PL for COC-Encapsulated $CsPbI_2Br$ thin films (c) Steady state PL spectra of the pristine (a green line) and the encapsulated COC (an orange line) $CsPbI_2Br$ PNCs (d) Steady state of the initial PL spectra of the pristine (a green line) and encapsulated COC (an orange line) $CsPbI_2Br$ thin films.

above 50 minutes of illumination, halide ion migration accelerated phase separation into (Br-rich domain) and (I-rich domain) with redshifts from 625 to 650 nm and 700 to 705 nm, respectively. Unlike pristine thin films 5.5(d), COC enhanced the brightness in both Br-rich and I-rich domains due to the reduced charge carriers funnelling from mixed to separated phases 5.1. [163].

5.7 Temperature dependence of the PL emission from nanocrystals without and with COC

The instability of mixed halide perovskites has been attributed to the low activation energy of halide ion migration, which facilitates more halide vacancy defects. To better understand, temperature-dependent PL emission was implemented to determine the ion migration activation energy (E_a) as shown in Figures 5.6 (a) - 5.6 (h). It is clear that the Arrhenius curve of the pristine and encapsulated PNCs consisted of two linear regions in Figure 5.6(d)-5.6(h). The pristine PNCs showed a lower E_a of 0.50 meV above 160 K and 0.060 meV below 160 K, respectively. These values are close to those from the provided measurements in Table 5-1. In case of encapsulated PNCs, the low-temperature linear region below 200 K showed the E_a of 0.47 meV due to electron/hole transport from photo-conductivity under illumination. However, the high-temperature linear region above 200 K exhibited a higher E_a of 1.3 meV, corresponding to active ion migration which helped increase conductivity exponentially [172]. A similar trend was also found in thin films where the E_a increased from 20 to 29 meV after being encapsulated with COC [163]. Based on the above results, we confirm that the encapsulation can effectively increase the E_a of halide ions, which is linked to inhibiting or reducing its migration.

It is clear that the PNCs with COC exhibited a negative activation at a critical point between cryogenic temperatures and 200 K which is often referred to as anti-Arrhenius behaviour[173–175]. From a chemical kinetics perspective, normal Arrhenius behaviour refers to reaction rates that increase with temperature whereas anti-Arrhenius behaviour describes a rate of a chemical reaction that increases with decreasing temperature. This phenomenon usually occurs in chemical reactions of molecules that have a high degree of internal energy such as excited states and radicals [175]. Two possible reasons can be considered to explain this anti-Arrhenius behaviour. Reactants require specific energy levels for collision and reaction. High kinetic energy at elevated temperatures leads to frequent collisions, while low temperatures reduce kinetic energy, increasing the likelihood of collisions. Additionally, reactants need specific orientations for collisions. High kinetic energy results in frequent collisions in unfavourable orientations, while

low energy increases the likelihood of favourable collisions. As a result, we suggest two possible reasons that might induce negative activation energy in our PNC samples. Firstly the activation energy might be negative if the reaction involves transition states that are more stable than the reactants. This implies that the reaction requires energy to decrease its rate and facilitate its occurrence. Secondly, the reaction might involve a barrierless pathway in which the reaction may occur without a need for activation energy, consequently the rate constant is more likely increase with decreasing the temperatures.

The activation energy (Ea) measured in this work		
	$CsPbBrI_2$ nanocrystals	$CsPbBrI_2$ thin films
Pristine Without COC	20.6 meV	20.8 meV [163]
Encapsulated With COC	39.3 meV	29.0 meV [163]
The activation energy (Ea) of various lead Halide Material		
	Process	The activation energy (Ea)
$CsPb(I_{0.5}Br_{0.5})_3$ Colloidal NCs	Photo-decomposition	62 kJ/mol [79]
$CsPb(Cl_{(1-x)}Br_x)_3$ Colloidal NCs	Halide Exchange	63 kJ/mol [176]
PbI_2 thin film	Photo-decomposition	16 kJ/mol [177]

Table 5.1: The activation energy of pristine $CsPbI_2Br$ and encapsulated $CsPbI_2Br$ nanocrystals and films compared to the previous activation energy for various mixed halide compositions.

5.8 TRPL of nanocrystals and thin films without and with COC

Time-resolved PL (TRPL) measurements were also employed to uncover the charge transport in these materials as shown in Figures 5.7 - 5.8. TRPL spectra of all samples showed a biexponential decay. The short-lived components of the PL decay curves arise from surface recombination in films [178, 179] and to excitons in nanocrystals [180], respectively, while the longer-lived components are usually ascribed to emission from bulk recombination in the case of films [178, 179], and to shallow surface traps in the case of nanocrystals [180, 181]. The fast decay lifetime (τ_1) and slow decay lifetime (τ_2) were 1.07 and 5.48 ns for the pristine $CsPbI_2Br$ PNCs, and 1.29 and 8.70 ns for the pristine $CsPbI_2Br$ thin films, respectively. The fast decay lifetime (τ_1) and slow decay lifetime (τ_2) were 1.30 and 13.88 ns for the encapsulated $CsPbI_2Br$ PNCs, and 2.93 and

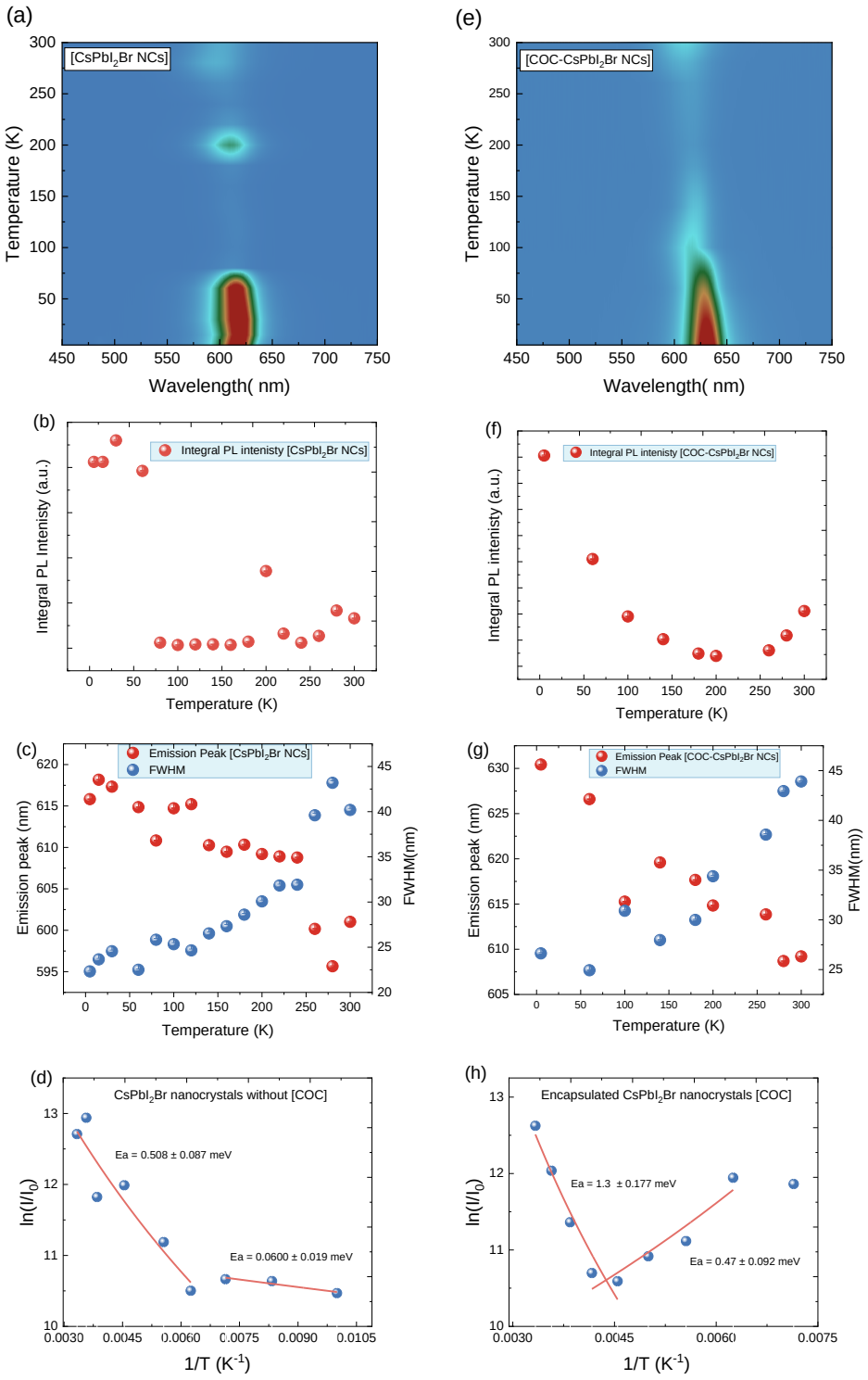

Figure 5.6: Temperature dependent photoluminescence of $CsPbI_2Br$ nanocrystals and their COC-encapsulated counterparts (a) and (d) The PL spectra of a 2D -colour plot of the $CsPbI_2Br$ PNCs and encapsulated counterparts at temperatures ranging from 5 to 297 K. (b) and (f) The integrated PL intensity as a function of temperature for $CsPbI_2Br$ nanocrystals and COC-encapsulated $CsPbI_2Br$, respectively (c) and (g) The emission peak and FWHM as a function of temperature for nanocrystals and COC-encapsulated $CsPbI_2Br$(d) and (h) Ion migration activation energy extracted from Arrhenius plot of the PL of $CsPbI_2Br$ PNCs and COC-Encapsulated $CsPbI_2Br$ PNCs, respectively.

18.64 ns for the encapsulated $CsPbI_2Br$ thin films, respectively. The prolonged lifetime of the encapsulated PNCs and thin films are associated with the decrease of electronic trap density and increased radiative recombination rates [164, 182].

Notably, the average carrier lifetime (τ_{avg} at 600 and 612 nm) was increased from 2.19 to 3.93 ns before light soaking 5.9(a) - 5.9(b), and from 1.32 to 10.51 ns after light soaking when PNCs being encapsulated 5.9(c) - 5.9(d), respectively. Similarly, the average carrier lifetime (τ_{avg} at 645 nm) was increased from 3.68 to 16.50 ns before light soaking 5.9(a) 5.9(b), and from 2.73 to 23 ns after light soaking after thin film being encapsulated 5.9(c) - 5.9(d), respectively. The increase can be attributed to inhibiting highly mobile ions (I^-) resulting from internal iodine migration after hole-induced iodine oxidation [70, 71, 166, 183, 184].

5.8.1 Time-resolved photoluminescence measurements of PNCs and thin films before 50 minutes of illumination

Before 50 minutes illumination in Figures 5.7 - 5.8 and 5.9, PNCs exhibited shorter PL lifetime than the thin film due to a larger degree of quantum and dielectric confinement and higher exciton binding energies [117, 185]. Due to the electrons and holes in $CsPbI_2Br$ PNCs are typically tightly bonded, resulting in faster lifetime recombination and shorter diffusion lengths than thin films. After encapsulation, the PL lifetime prolonged due to reduced defect density inside or on the surface of PNCs and thin films, which increases halide vacancy formation energy and suppresses non-radiative recombination, in agreement with results in Figure 5.6(d)-5.6(h). The inhibition of highly mobile surface ions (I^-), which originate from internal iodine migration caused by hole-induced iodine oxidation is responsible for the increase in the long-lived lifetime of COC-encapsulated PNCs and thin films. In particular, halide ions (e.g., I^-) capture holes, rendering them highly mobile as the oxidized halide ($I^{\cdot}$) is ejected from pristine PNCs and thin films [70, 71, 183, 184]. Thus, COC can strongly binds and localizes excitons, making hole trapping at halide sites less probable [166].

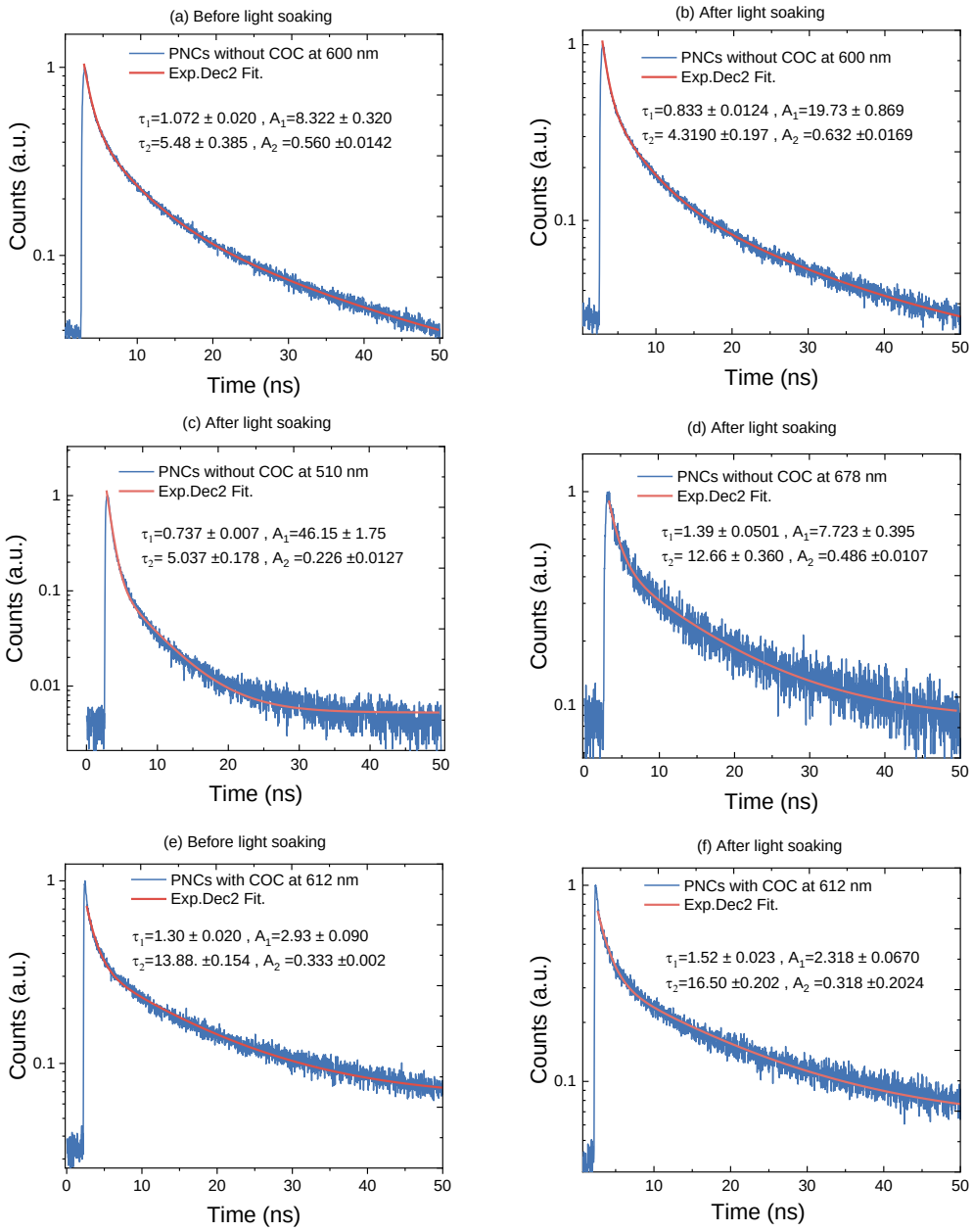

Figure 5.7: Time decay parameters of $CsPbI_2Br$ nanocrystals and their COC-encapsulated counterparts before and after 50 minutes of a blue light illumination at a wavelength of 450 nm at a laser repetition rate of 7.8 MHz for PNC with COC and 16 MHz for PNCs without COC, respectively. The fitted TRPL decay parameters were extracted using the equation: $f(t) = A_1 \exp(-t/\tau_1) + A_2 \exp(-t/\tau_2) + y_0$, where τ_1 refers to short-lived PL emission, and τ_2 represents the long-lived lifetime.

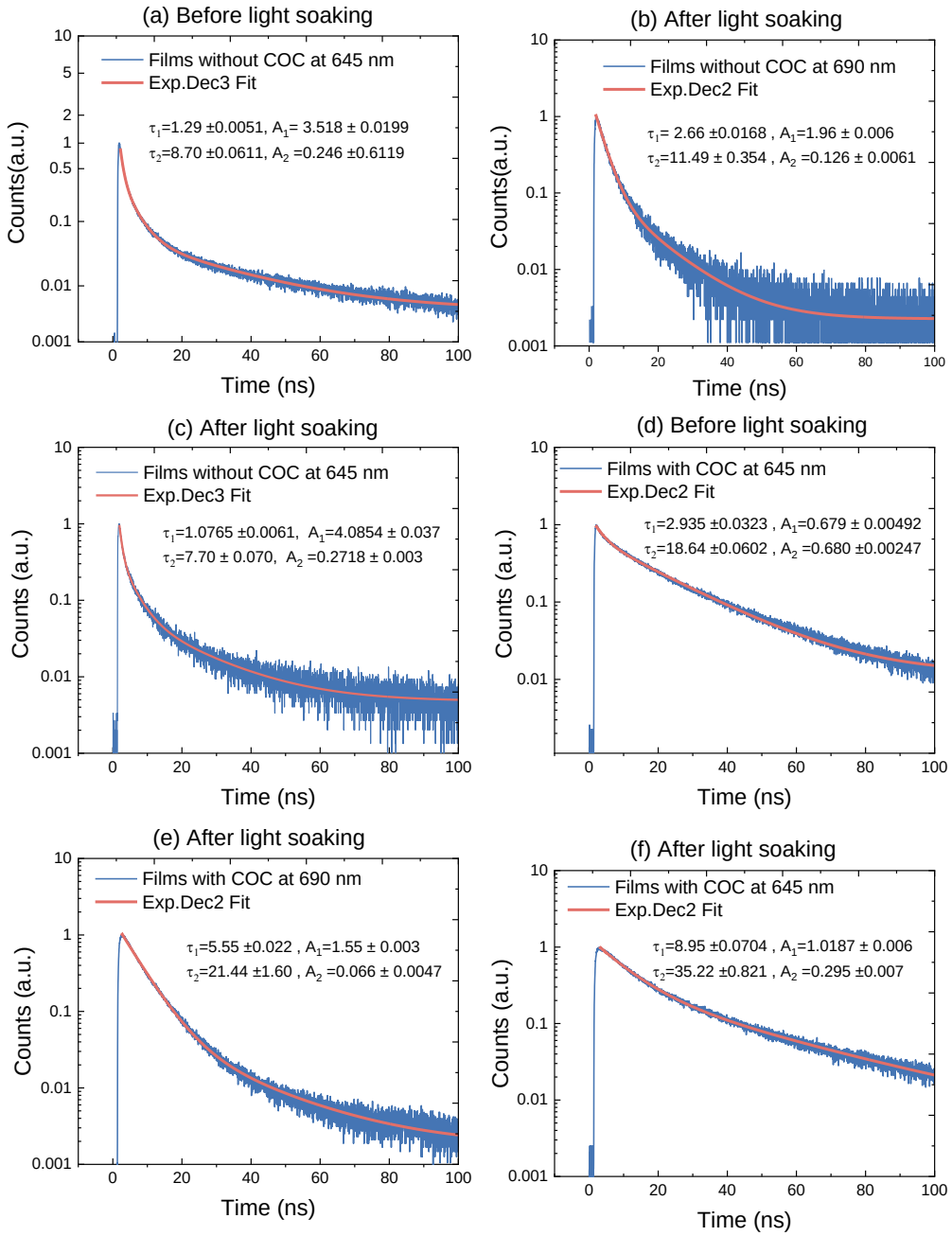

Figure 5.8: Time decay parameters of $CsPbI_2Br$ thin films and their COC-encapsulated counterparts before and after 50 minutes of a blue light of illumination at a wavelength of 450 nm and a 8.3 MHz laser repetition rate. The fitted TRPL decay parameters were extracted using the equation: $f(t) = A_1 \exp(-t/\tau_1) + A_2 \exp(-t/\tau_2) + y_0$, where τ_1 refers to short-lived PL emission, and τ_2 represents the long-lived lifetime.

5.8.2 Time-resolved photoluminescence measurements of PNCs and thin films after 50 minutes of illumination

After 50 minutes illumination in Figures 5.7(c), both short and long-lived lifetimes at a green glow emission of PNCs were faster compared to the mixed halides and red emission Figures 5.7(b) - 5.7(d). This refers to the continuous illumination that may increase photogenerated holes, halide oxidation products, and thereby increase the electron and hole mobility. Such complex dynamics mirror the iodine sublimation I_2 level and perovskites lattice contraction after light soaking [79, 154]. For thin films, the situation differs due to lower surface-to-volume and higher concentration of multi-surface defects in Figures 5.8(b) - 5.7(c) and 5.7(d). It is worth noting that both the short and long-lived lifetimes of encapsulated PNcs and thin films were increased compared to their pristine counterparts. This can be evident that the COC matrix passivated surface dangling bonds and halide vacancies and prevented the leakage of volatile decomposition products over an extended period of illumination. Based on the law of mass action at a constant temperature, encapsulation using a COC matrix may ensure that PNCs and thin films are inside a thermodynamically closed system, allowing only energy exchange and chemical equilibrium concentrations of solid and gas products.

5.9 Conclusion

This chapter focused on the core reasons for photo-induced halide oxidation upon the redox model framework and photochemical stability at room temperature. The results exhibited a comprehensive comparison of $CsPbI_2Br$ PNCs and $CsPbI_2Br$ thin films before and after encapsulation using cyclic olefin copolymer in the context of their stability under 50 minutes of continuous blue-light illumination. Before encapsulation and within 50 minutes of illumination, pristine $CsPbI_2Br$ PNCs showed halide sublimation and developed a green glow, and the emission shifted towards the blue end of the spectrum, with iodine ion agglomeration at deep red regions. On the other hand, pristine $CsPbI_2Br$ thin films underwent a reversible iodine exchange that provided an extra iodine transport pathway within the hole trap level, leading to a red-shifted spectrum.

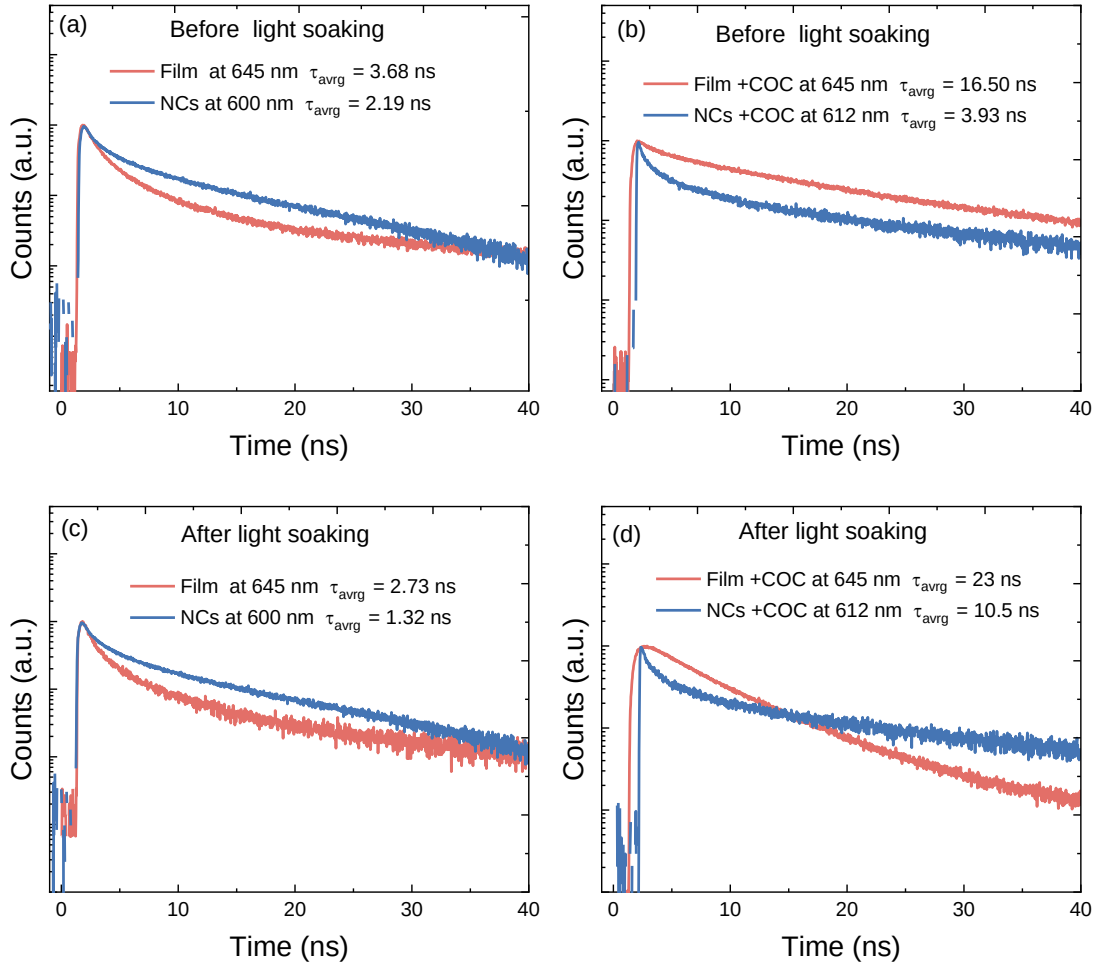

Figure 5.9: Time-resolved photoluminescence (TRPL) (a) The pristine $CsPbI_2Br$ PNCs and $CsPbI_2Br$ thin films before 50 minutes illumination, (b) COC-encapsulated $CsPbI_2Br$ PNCs and $CsPbI_2Br$ thin films before 50 minutes illumination, (c) The pristine $CsPbI_2Br$ PNCs and $CsPbI_2Br$ thin films after 50 minutes illumination and (d) The COC-encapsulated $CsPbI_2Br$ PNCs and $CsPbI_2Br$ thin films after 50 minutes illumination.

Furthermore, pristine $CsPbI_2Br$ thin films demonstrated a reversible recovery process after a four-hour dark restoration period, whereas pristine $CsPbI_2Br$ PNCs exhibited an irreversible process due to halide oxidation. The formation energy of defects was estimated through temperature-dependent micro photo-luminescence (PL) spectroscopy, which was approximately 0.50 meV at high low temperatures and 0.06 meV at low temperatures for pristine PNCs, and 20 meV for pristine thin films at high and low temperatures, respectively. The average PL lifetime at 0 minutes was calculated to be 2.19 ns at 600 nm for pristine PNCs and 3.70 ns at 645 for thin films. At 50 minutes, the average PL lifetime for pristine PNCs was determined to be 0.66 ns for green glow

emission at 510 nm, 1.23 ns for mixed halide emission at 600 nm and 1.40 ns for iodine agglomeration emission at 678 nm, respectively. However, the average PL lifetime for pristine thin film was determined to be 2.73 ns for mixed halide emission at 645 nm and 4 ns for iodine-rich phase emission at 690 nm, respectively.

After COC- encapsulation and within 50 minutes of illumination, COCO-$CsPbI_2Br$ PNCs showed a stable spectral emission at 615 nm, hindering iodine oxidation or aggregation and thereby preventing iodine gas leakage and impeding iodine oxidation or aggregation. On the contrary, the photochemical stability of COC-$CsPbI_2Br$ thin films was comparatively lower than that of the COC-$CsPbI_2Br$ PNCs. This discrepancy arose from the increased spatial freedom of excited charge carriers and the reduced quantum confinement, which resulted in prolonged interdiffusion at low-energy regions. In addition, the formation energy of defects increased after COC-encapsulation to be 1.3 meV at high low temperatures and 0.47 meV at low temperatures for PNCs and 29 $\pm$ 20 meV for thin films, respectively. Following encapsulation, the average PL lifetime at 0 minutes was extended by 3.93 ns at 612 nm for PNCs and by 16.50 ns at 645 nm for thin films. After 50 minutes of illumination, the average PL lifetime for COC-PNCs increased by 10.5 ns at 612 nm, and by 23 ns at 645 nm and 6.30 ns at 690 nm for COC- thin films compared to the first illumination minute.

According to the findings presented in this chapter, the level of halide vacancies(V_X) was an essential factor in the instability of iodide ions in $CsPbI_2Br$ PNCs and $CsPbI_2Br$ thin films. Halide ion migration was caused by the photooxidation of I^- to I^* (iodide instability), which favourably migrates into interstitial defects by simultaneously creating halide vacancies. The encapsulation increased the ion migration activation energy of the $CsPbI_2Br$ PNCs compared to their thin film counterparts (remaining low), reflecting that halide ions in $CsPbI_2Br$ films exhibit the largest contribution to ionic conductivities. This also implies that the number of vacancies for halide ions in $CsPbI_2Br$ films is higher than in the $CsPbI_2Br$ PNCs because of the low formation energy. These results assist an understanding of the nanoscopic performance and degradation landscape in all complex lead halide perovskites and offer a promising technical route for fabricating highly efficient and long-term stability of pure red LEDs using NCs and polymer matrices.

6

Dramatic Photoluminescence Enhancement of Graphene Covered $CsPbBr_3$ Quantum Dots

6.1 Introduction

All inorganic lead halide perovskites (LHP) $CsPbX_3$ (X = Cl, Br or I) have emerged as promising materials for a wide range of optoelectronic applications such as solar cells [186, 187] light-emitting diodes,[188] and photodetectors [189] due to their higher stability compared to their organic-inorganic counterparts [190, 191]. The $CsPbBr_3$ has excellent optoelectronic properties, including an extremely high photoluminescence (PL) quantum yield, narrow emission bandwidth, and long carrier diffusion length and lifetime [192, 193]. Furthermore, the emission energy of $CsPbBr_3$ can be tuned from 2.29 eV to 2.53 eV by synthesizing it in various structures such as bulk single crystals, thin films, nanocrystals (NCs), nanowires, and quantum dots (QDs) [194, 195]. $CsPbBr_3$ nanostructures emission could originate from various sources, including a single exciton, lasing due to biexcitonic emission [196], cavity lasing from micro/nanowire [197], triplet excitonic emission [198] and superfluorescence [199].

Using LHPs in heterojunctions is an effective way to improve their optoelectronic properties. In particular, a graphene (Gr) sheet with ultrahigh carrier mobility [200] and

wavelength independent light absorption [201] has been hybridized with $CsPbBr_3$ to enhance its optoelectronic performance [189, 202, 203]. Namely, enhanced visible light absorption was observed in the $CsPbBr_3$-NCs/Gr heterostructure [202, 203]. Interfacial energy level alignment of $CsPbBr_3$-NCs/Gr junction facilitated electron transfer from the $CsPbBr_3$ light absorber to the Gr electron transport layer, resulting in strong PL quenching and improved photo response [189, 202]. In addition, it is well-known that surface defects can introduce non-radiative trap states in LHPs electronic structure [204, 205]. Thus, the passivation of surface defects can significantly affect the PL properties of these materials. Research has been conducted on applying a variety of molecules with different functional groups to passivate structural defects in LHPs [206]. Notably, it was shown that by encapsulating $MAPbBr_3$ NCs with Gr, surface defect states generated by Pb vacancies were passivated, and the photoluminescence intensity was enhanced by a factor of seven [207]. Another effective method to improve the quantum efficiency of optoelectronic heterojunctions is PL enhancement by surface plasmons [208, 209]. In particular, it has been reported that for Gr/semiconductor interfaces, Gr plasmon was resonantly activated by radiative recombination of electron-hole pairs from a semiconductor photo absorber. Consequently, Gr plasmon transformed into propagating photons through interaction with interface corrugations explaining the observed enhancement in PL [210, 211].

6.2 Plasmon

The term “plasmon” was first proposed by Pines in 1956 during his investigation of energy dissipation in materials [212]. He noticed in his research that solids could exhibit a cloud of collective electron oscillations at particular excitation conditions. As a result, he identified the plasmon as a “quantum of elementary excitation linked to this collective motion at high frequencies.” Although the term’s meaning has changed since it was first introduced, the plasmon is generally understood as the quantum quasi-particle representing the energy excitations caused by the oscillating charge densities in a plasma. It is worth mentioning that there are certain similarities and distinctions comparable to the photon, which is more widely recognized as a quantum particle. Plasmons are quantum quasi-particles that govern charge density oscillations, while

photons are quantum particles that govern free electromagnetic fields. Moreover, the ability of a photon to continuously propagate in free space is a significant distinction from the lossy nature of charge density oscillations in a plasmon, which will consequently vanish in the absence of continuous excitation. This attribute distinguishes a quantum particle from a quantum quasi-particle. Despite the fact that plasmons are quantum constructs, classical interpretations of plasmas and their interactions can provide deep insight into their properties as illustrated in Appendix-B [213, 214].

6.3 Exciton-plasmon coupling interactions

Exciton-plasmon coupling and the conversion of exciton-plasmon-photon interactions have been extensively studied [215]. There are two distinct types of exciton-plasmon coupling, each exhibiting unique optical characteristics. First, the strong exciton-plasmon coupling generates two new mixed states of matter and lights energetically separated by a Rabi splitting, demonstrating the anticrossing behaviour of the exciton-LSP energy tuning. Second, the weak exciton-plasmon coupling, including surface-enhanced Raman scattering, surface plasmon (SP)-enhanced absorption, enhanced fluorescence, and fluorescence quenching, which represent no perturbation between wave functions [216]. SP resonance (SPR) is a phenomenon that can be utilized to examine the interaction between light and matter beyond the diffraction limit. It is produced by the collective oscillation induced by the electromagnetic field of light. Since its discovery, the relationship between Surface Plasmon Resonance (SPR) and excitation has drawn significant interest.This is because of its contributions to the application of (SPR) in light-emitting diodes, solar cells, low-threshold lasers, biological detection, and quantum information processing, in addition to its expanding and broader understanding of the technology [215].

6.4 Structure and Growth

The fabrication of $CsPbBr_3$ rods was undertaken in collaboration with Professor Atanu Jana, Sangeun Cho, and Hyunsik Im from the Division of Physics and Semiconductor at Dongguk University, Seoul 04620, Korea. First, in a 100 ml glass bottle, Cs_2CO_3

(0.0325 g, 0.01 mmol) was placed into a 15 mL glass vial with 2 mL 1-octadecene (ODE) and 1 mL oleic acid (OA), then dried at 120° for 1 hour until all Cs_2CO_3 had reacted with OA and kept it for 3 hr. In another glass vial, $PbBr_2$ (0.073 g, 0.02 mmol) and n-octylammonium bromide (OAmBr) (0.042 g, 0.2 mmol) were dissolved in 1 mL DMF and 2 mL of ODE at 120° and kept for 3 hr. Subsequently, 3 mL Cs-oleate solution was injected into the lead precursor solution, resulting in a change of solution color to greenish yellow. The crude solution was centrifuged for 5 minutes at 5000 rpm after cooling to room temperature. The residue was redispersed in toluene by sonication and again centrifuged at 5000 rpm for 10 min. The obtained product was washed with 2 ml of methyl acetate and subjected to another centrifugation at 10000 rpm for 10 minutes. Finally, the product was dried in a vacuum oven at 60° for 12 hours. The $CsPbBr_3$ QDs were put in a toluene solution and the solution was treated under sonication for 10 min. Then the solution was dispersed on a SiO_2 (300 nm)/Si substrate. Then the graphene (Gr) was transferred on the $CsPbBr_3$ dispersed SiO_2 substrate. The PMMA-coated Gr prepared on a Cu foil was placed in a solution of Cu etchant (CE-100, Transene Company, Inc.) to remove the Cu foil. After the Cu foil was completely removed away, the PMMA-coated Gr was scooped using the $CsPbBr_3$ dispersed SiO_2. The PMMA layer was then removed with acetone, and the sample was rinsed several times with deionized (DI) water.

6.5 Density function theory calculation

The Density function theory calculations (DFT) were implemented in collaboration with Professor Geunsik Lee and Elham Oleiki from Department of Chemistry, College of Natural Science, Ulsan National Institute of Science and Technology, Ulsan 44919, in Korea. First of all, DFT calculations were performed using the Vienna ab initio simulation package based on the plane wave pseudopotential approach, [217] and by utilizing Generalized gradient approximation (GGA) within PBE parameterization [218] as exchange-correlation functional. To incorporate Van der Waals interactions, dispersion correction was added to the total energy and forces by employing Tkatchenko and Scheffler (TS) approach [219]. To model the $CsPbBr_3$ layer, first, the atomic structure of the bulk $CsPbBr_3$ cubic phase was optimized using the experimental lattice parameter

of 5.87 Å[220]. Then the optimized bulk unit cell was used and designed four different (001) $CsPbBr_3$ slabs considering both CsBr and $PbBr_2$ surface terminations insets as shown in Figure 6.1[202, 219].

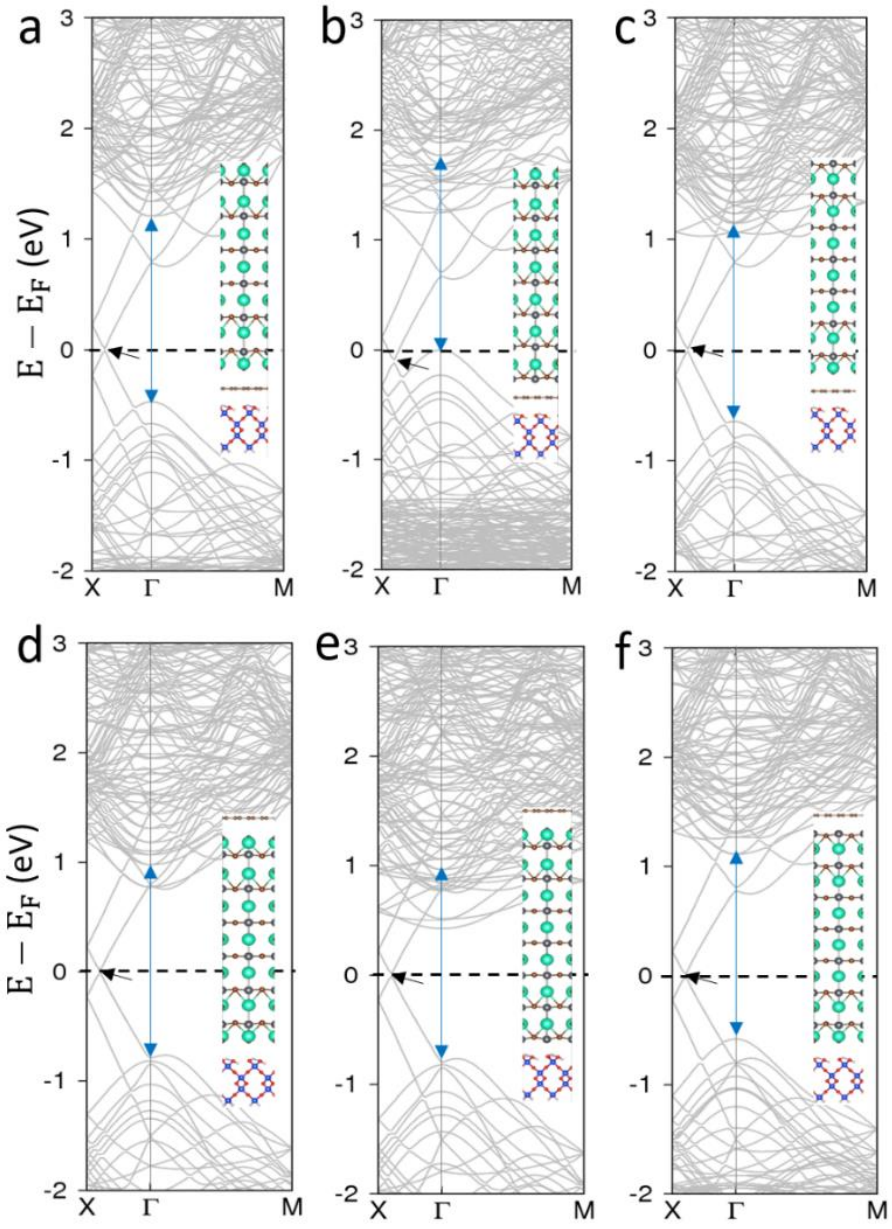

Figure 6.1: Calculated electronic band structure of (a)(b)(c) $CsPbBr_3$/graphene/SiO_2, and (d)(e)(f) graphene/$CsPbBr_3$/SiO_2 with different perovskite surface terminations. The electronic transition between the $CsPbBr_3$ band edges is indicated by the blue arrow, and graphene's Dirac point is mentioned by the black arrow. All side wives in insets are along [100]. Atomic color scheme: Cs (green), Pb (gray), Br (brown), Si (blue), O (red), H (pink), C (brown).

To have distinguishable contributions from surface and bulk states in the electronic structure, the unit cell was repeated 7 times along the [001] direction and optimized all atomic positions. Also, to gain the lowest amount of lattice mismatch in heterostructure supercells, $\times\sqrt{2}\times\sqrt{2}$ unit cells of 2D-$CsPbBr_3$ and 7×2 rectangular layer of Gr were employed, and $4\times$ 2 unit cells of SiO_2 composed of 4 atomic layers along [001] direction. The SiO_2 slab was made from its cubic bulk structure with the lattice parameter of 4.93. The lattice mismatch values for $CsPbBr_3$, Gr, and SiO_2 were 0.8%, 6%, and 30%, respectively. To avoid spurious interactions between the periodic images of heterostructures, 15 of space along the [001] direction was inserted and optimized for all the atomic positions except for the two bottom layers of SiO_2 by using a single Γ- point. The kinetic energy cutoff was set to 400 eV while convergence criteria of 10^{-4} eV and 0.05 eV/Å were employed for energies and forces, respectively. To model the $CsPbBr_3$ surface with V_Br defects, the ideal $CsPbBr_3$ /Gr supercell was used, and repeated it twice along [010] direction as illustrated in Figure 6.2, and introduced one surface Br vacancy per each 1×2 supercell.

The defect model for the $CsPbBr_3$ slab corresponded to a surface defect concentration of $10^{13}\,cm^{-2}$, comparable to the experimental value [191, 221]. Atomic positions of the Gr layer and four top atomicslayers of the $CsPbBr_3$ surface were optimized. Perdew-Burke -Ernzerhof (PBE) electronic structure calculations were performed on a $4\times4\times1$ K-point mesh by setting energy convergence criteria and kinetic energy cutoff 10^{-4} and 400 eV, respectively. The calculated direct band gap for cubic bulk structure was 1.53 eV which is consistent with other theoretical reports; [192] however, it underestimates the experimental value of 2.22 eV [193]. To get a better agreement with the experimental band gap, (the Green's function (G) and the screened Coulomb interaction (W) (GW) + spin-orbit coupling (SOC)) or HSE (Heyd-Scuseria-Ernzerh) of Hybrid Functional + spin-orbit coupling (SOC) method should be implemented, [192, 194, 222] though, considering the high number of atoms in the supercells (more than 300), employing this level of calculation was not plausible. Nonetheless, the main characteristics of the conduction and valance bands of $CsPbBr_3$ were maintained using the PBE method [43]. In addition, because of the quantum confinement effect, the band gap of the $CsPbBr_3$

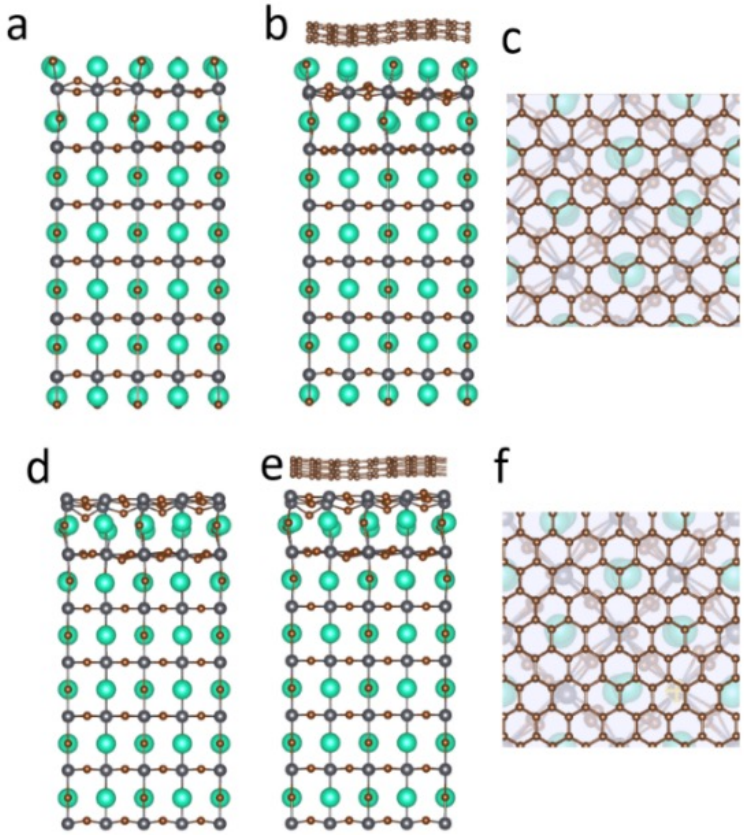

Figure 6.2: Side view along [100] of (a) CsBr terminated (001) $CsPbBr_3$ slab with VBr surface defect and (b) its interface with Gr. (c) Top view of (b). (d) $PbBr_2$ terminated (001) $CsPbBr_3$ slab with VBr surface defect and (e) its interface with Gr. (f) Top view of (e). Atomic color scheme: Cs (green), Pb (gray), Br (brown), Si (blue), O (red), H (pink), C (brown).

layer increased to 1.85 eV which is closer to the experimental value. Therefore, all the electronic structure calculations were performed using the PBE method.

6.6 Optical Characterization

A 100 fs frequency-doubled Ti:sapphire laser operating at 400 nm with a repetition rate of 80 MHz was used as the excitation source. The incident laser power on the $CsPbBr_3$ surface ranged from a few nW to a few tens of μW. Measurements were performed at cryogenic temperatures. The optical properties were characterized using a fiber-based confocal micro-photo-luminescence (μPL) setup. A 100× long working distance apochromatic objective was held by a sub-micron precision piezoelectric stage above

the cryostat and used to focus the incident laser beam diameter of $\sim 1\,\mu m^2$ and to collect the resulting luminescence. The luminescence was then directed to a 0.3 m focal length spectrometer with a 1200 gr/mm grating giving a spectral resolution of $\sim$ 700 μeV. The signal was finally detected using a cooled charge coupled device (CCD) detector. A telecentric lens arrangement was also present allowing the incident angle of the exciting laser at the entrance to the objective to be varied by a computer-controlled mirror thus providing an independent means to move the exiting spot relative to the collected emission, which is imaged confocally through the center of the objective. Time resolved photoluminescence (TRPL) measurements were carried out using the same experimental set up as above. The dispersed PL was reflected towards a photomultiplier connected to a commercial photon counting system. Measurements of the lifetimes of the confined states were then carried out over a range of excitation power densities.

6.7 Crystal structure properties of the $CsPbBr_3$ QDs

The detailed crystal structure of the individual $CsPbBr_3$ QDs was investigated using transmission electron microscopy (TEM). The TEM images were taken on a JEOL JEM-2100F electron microscope using a 200 kV electron source. Samples were prepared on 200-mesh carbon coated Cu grids by dropping NC solutions which were allowed to evaporate, and all TEM images were supplied by Professor Atanu Jana from Dongguk University in Korea. Figure 6.3(a) shows the TEM images of the $CsPbBr_3$ QDs. The individual QDs tend to aggregate, forming clusters of various sizes. Compared to previous reports for well-aligned $CsPbBr_3$ QDs [192, 223, 224]. Our small QDs have a tetragonal shape with dimensions randomly distributed from $\sim$ 10 to 50 nm as shown in high resolution TEM in Figure 6.3 (b). Even though the sizes are randomly distributed, each clump has70 $\sim$ 80 % of the QDs in the same direction. When we measure the PL, we dispersed the QD clusters with a size of $\sim 2\,\mu$m on the SiO_2 substrates as illustrated in the schematic diagram is depicted in Figure 6.3(c). The resulting PL emission will have both enhanced coherence and directionality. Note that the microscopic oscillating dipoles align with each other leading to the formation of a macroscopic dipole within a dephasing time limit. Like other semiconductor QDs, the size and geometry for a matrix of $CsPbBr_3$ QDs

are subject to some extent of variations. Although the spin coating process has helped to spatially filter the QD clusters based on their sizes, we often found that clusters of similar dimensions are clumped together. It is therefore possible to excite multiple QD arrays under slightly different conditions within a single laser spot. In most of the cases, the QD clusters produce independent signals given their distinct emission centers. However, clusters of very similar geometric formation, or even two closely alike matrices of QDs within a single cluster, can sit in close proximity such that their individual collective behaviors can overlap and they can interact with each other.

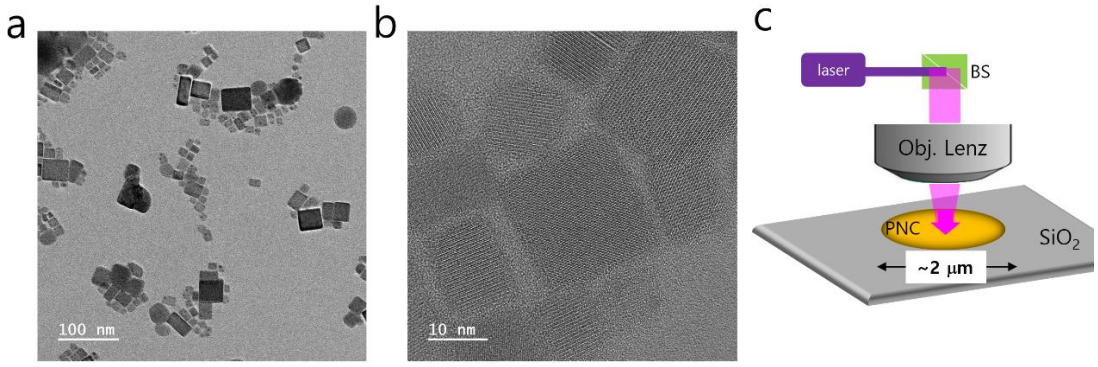

Figure 6.3: (a) Transmission electron microscopy images of $CsPbBr_3$ QD clusters. (b) High resolution transmission electron microscopy image of individual dots in a cluster. The QDs were ultra-sonicated for 10 min in toluene solution and then dispersed on the TEM grid. (c) Schematic diagram of the μ-PL setup. The laser beam focuses on the $CsPbBr_3$ cluster with a diameter of $\sim 2\,\mu$m.

6.8 Optoelectronic properties for the bare-$CsPbBr_3$ and Gr-coveredCsPbBr$_3$ QDs

Figure 6.4 presents excitation power-dependent PL spectra for the bare- $CsPbBr_3$ and Gr-covered $CsPbBr_3$ QDs, measured at low temperature. For the bare $CsPbBr_3$ QDs, a single excitonic emission near 2.33 eV with a full width at half maximum (FWHM) of ~ 8 meV (~ 2 nm) is observed at an excitation fluence of $\sim 32\,\mu$J/cm^2 (Inset in Figure 6.4 (a)). It should be noted that by increasing the excitation fluence, new blue-shifted emission lines appear. The integrated intensity of the emission line in Figure 6.4 (a) shows an S shape behavior as illustrated in Figure 6.5 (a), which indicates stimulated emission.

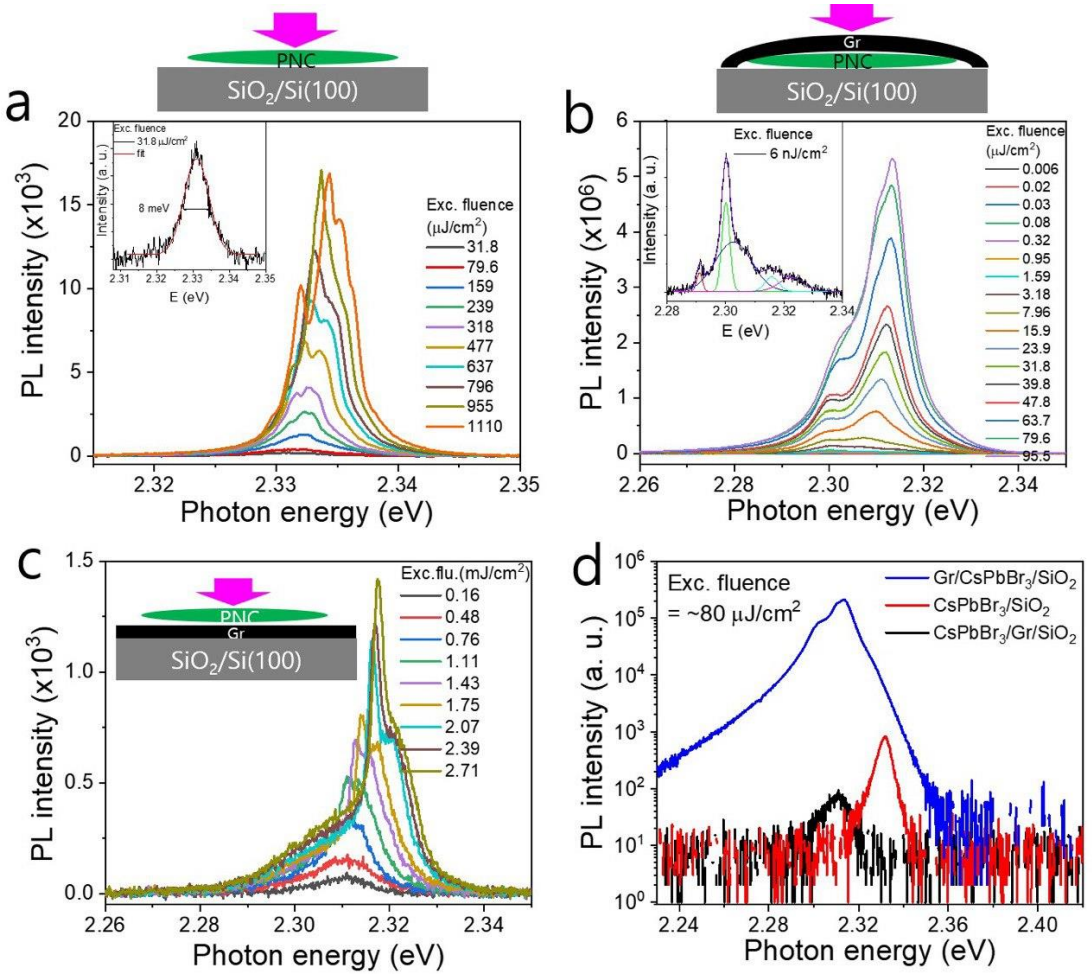

Figure 6.4: PL comparison between Gr-coated and uncoated $CsPbBr_3$ QD clusters at 4.2 K. (a) Power-dependent μPL spectra measured for the bare $CsPbBr_3$ QD cluster. Lasing is observed at high pumping fluence. Inset depicts the PL spectrum and fit (red) at the lowest excitation fluence of 31.8 $\mu J/cm^2$. (b) Power-dependent μPL spectra taken for a Gr-coated $CsPbBr_3$ (Gr/$CsPbBr_3$/SiO2) heterostructure clusters. Inset depicts the PL spectrum and fit at the lowest excitation fluence of 6 nJ/cm^2. Two distinguishable emission lines at 2.313 eV and 2.300 eV are present. With increasing pumping strength, the main emission evolves from the 2.300 eV peak towards the 2.313 eV peak. (c) The excitation power-dependent μPL spectra of the $CsPbBr_3$/Gr/SiO_2 structure. Even at the excitation power of 0.16 kJ/cm^2, the spectrum is very noisy and broad with an FWHM of $\sim$ 5 meV and the intensity doesn't increase much at high excitation power of 2.7 kJ/cm^2. (d) Comparison of the PL spectra of the bare $CsPbBr_3$ and Gr-covered $CsPbBr_3$ at the excitation fluence of $\sim$ 79.6 $\mu J/cm^2$. For the $CsPbBr_3$/Gr, the excitation fluence is $\sim$ 160$\mu J/cm^2$.

Unlike the bare $CsPbBr_3$ QDs, however, the PL spectra of the Gr-covered $CsPbBr_3$ QDs show several emission peaks even at a very low excitation fluence of $\sim$ 6 nJ/cm^2 Figure 6.4(b). The integrated PL intensity of the Gr-covered $CsPbBr_3$ QDs shows a linear dependence with excitation fluence in Figure 6.5 (b). Although no stimulated emission

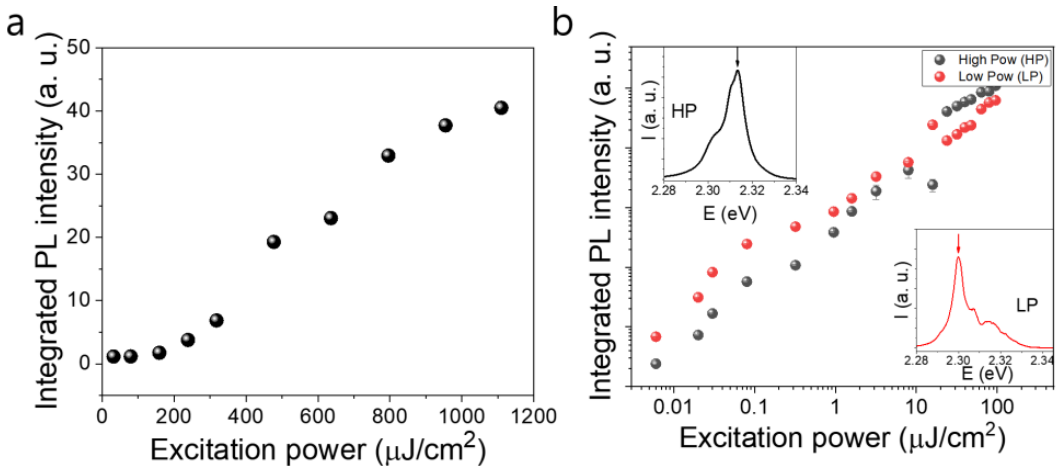

Figure 6.5: (a) Integrated PL intensity of the bare $CsPbBr_3$ QDs red dot marked peak in Fig. 2a. (b) Integrated PL intensity of the Gr covered $CsPbBr_3$ QDs at the main peaks of the low and high excitation power. Here, LP and HP mean the low excitation power and high excitation power, respectively

peak was observed in this case, the PL intensity was significantly enhanced as shown in Figure 6.4 (a)-(c) that presents the comparison of the PL spectra of the pure-$CsPbBr_3$, $CsPbBr_3$/Gr, and Gr-covered $CsPbBr_3$ at the similar excitation fluence of $\sim 80\ \mu J/cm^2$. On the other hand, the PL intensity of the$CsPbBr_3/Gr/SiO_2$ heterostructure is quenched Figure 6.4(c), consistent with the previous reports [202, 203]. In addition, it shows a much brighter emissive response with a high signal-to-noise ratio. At this level of pumping strength, no identifiable emission profile can be retrieved for the bare $CsPbBr_3$ QDs. Also, no new emission peaks emerge, and none of the original peaks show a blue-shift below an excitation fluence of a few tens of μW.

6.9 The electronic structure properties for the bare-$CsPbBr_3$ and Gr-covered $CsPbBr_3$ QDs

To investigate the origin of the PL intensity quenching, we explored the electronic structure of the $CsPbBr_3/Gr/SiO_2$ heterostructure by performing the DFT calculations. The model structure is described in the method section (6-5) and is illustrated in Figure 6.6 (a) and Figure 6.7(a).

According to the DFT calculation results, the $CsPbBr_3$/Gr interface is stabilized through weak Van der Waals interaction with an interlayer distance of 3.4 Å, and binding energy of -0.03 eV per carbon atom as represented in Eq. 6-1 in which Equations (6-1) to (6-3) define the binding energy of Gr and perovskite layer in $CsPbBr_3$/Gr/SiO_2, Gr/$CsPbBr_3$/SiO_2, and Gr/$CsPbBr_3$ heterostructure, respectively:

$$EB = E(\mathrm{CsPbBr_3/Gr/SiO_2}) - E(\mathrm{Gr/SiO_2}) - E(\mathrm{CsPbBr_3}) \tag{6.1}$$

$$EB = E(\mathrm{Gr/CsPbBr_3/SiO_2}) - E(\mathrm{Gr}) - E(\mathrm{CsPbBr_3/SiO_2}) \tag{6.2}$$

$$EB = E(\mathrm{Gr/CsPbBr_3}) - E(\mathrm{CsPbBr_3}) - E(\mathrm{Gr}) \tag{6.3}$$

where $E(\mathrm{CsPbBr_3/Gr/SiO_2})$ is the total energy of $CsPbBr_3$/Gr/SiO_2 heterostructure, $E(\mathrm{Gr/SiO_2})$ is the total energy of Gr/SiO_2 heterostructure, $E(\mathrm{CsPbBr_3})$ is the total energy of isolated $CsPbBr_3$, $E(\mathrm{Gr/CsPbBr_3/SiO_2})$ is the total energy of Gr/$CsPbBr_3$/SiO_2 system, $E(\mathrm{Gr})$ is the total energy of isolated Gr layer, and $E(\mathrm{Gr/CsPbBr_3})$ is the total energy of Gr/$CsPbBr_3$ heterostructure. According to these definitions, negative (positive) value of EB suggests a stable (unstable) interface.

The ground state electronic band structure of the $CsPbBr_3$/Gr/SiO_2 heterostructure, including a perovskite symmetry slab with $PbBr_2$ termination, is depicted in in Figure 6.6(a). The $CsPbBr_3$ layer shows a direct band gap of 1.9 eV located at the γ-point. In addition, upon forming $CsPbBr_3$/Gr interface, electrons transfer from the $CsPbBr_3$ to the graphene, indicating the n-doped character of graphene as evidenced by the Dirac point appearing below the Fermi level. Moreover, the Fermi level is strongly pinned to the perovskite's valence band maximum (VBM). Therefore, under the illumination of the perovskite light absorber, electrons will readily transfer from the graphene layer to photo-generated empty states in the perovskite valance band. Consequently, the radiative recombination of photo-excited electron-hole pairs in perovskite will be suppressed, leading to PL quenching in $CsPbBr_3$/Gr/SiO_2 system, which agrees with previous reports [189, 202, 203]. The Fermi level pinning at the perovskite VBM is confirmed to appear when the $PbBr_2$-terminated surface is in contact with Gr/SiO_2, being independent of the terminal type of the opposite side as shown in Figures 6.1 (a-c). We also modeled the Gr/$CsPbBr_3$/SiO_2 heterostructure in Figure 6.6(b) and Figure 6.7 (b) to determine the

reason for the PL intensity enhancement. Like the $CsPbBr_3$/Gr/ SiO_2 heterostructure, the interfacial interaction at the Gr/$CsPbBr_3$ junction is of van der Waals type with an interlayer distance of 3.3 Åand a binding energy of -0.03 eV per carbon atom in Eq. 6-2. The ground state electronic band structure of the Gr/$CsPbBr_3$/SiO_2 heterostructure is shown in Figure 6.6(b). The $CsPbBr_3$ layer exhibits a direct band gap of 1.80 eV at the Γ- point, which is slightly reduced compared with $CsPbBr_3$/Gr/SiO_3 heterostructure, and Gr's Dirac cone is located between the γ and X points. Interacting with the SiO_2 interface dipole increases the $CsPbBr_3$ work function, leading to a downward shift of its VBM and CBM. This, in turn, enhances the interfacial electrostatic potential barrier for charge transfer at the Gr/$CsPbBr_3$ interface which is evident by comparing the position of the perovskite's VBM and CBM relative to the graphene Dirac point (Figure 6.6(b)). Furthermore, following the downshift of the perovskite energy levels, the interfacial orbital coupling at the Gr/ $CsPbBr_3$ interface is suppressed. Therefore, the formation of the Gr/ $CsPbBr_3$/SiO_2 heterostructure does not result in charge transfer at the Gr/ perovskite interface in its ground state, even for the other termination types of the perovskite layer (Figures 6.1 (d-f)). Under illumination, the interfacial electrostatic potential barriers are high enough to prevent carrier leakage from the perovskite layer to graphene, which enhances radiative recombination compared to $CsPbBr_3$/Gr/SiO_2 heterostructure.

Another possibility for explaining the PL enhancement could be associated with a surface stabilization effect via defect passivation, as we have shown in our previous work on passivation effect giving rise to significant PL enhancement [207]. We explored the structural and electronic properties of a defected $CsPbBr_3$ layer with and without graphene on its surface. Since Br vacancy (V_Br) is reported to be the predominant defect in $CsPbBr_3$ perovskites [197, 205], we introduced a V_Br into a $PbBr_2$-terminated $CsPbBr_3$ (001) surface.

The optimized geometry for the defected interface Figure 6.6(d) indicates structural distortions in the perovskite top layers caused by V_Br. A Gr is physisorbed on the perovskite surface with a binding energy of -0.03 eV per carbon atom (Eq. 6-1). We should note that the graphene deformation is an artifact of our model supercell. As shown in Figure 6.6(c), the VBr generates a localized trap state close to the $CsPbBr_3$ conduction

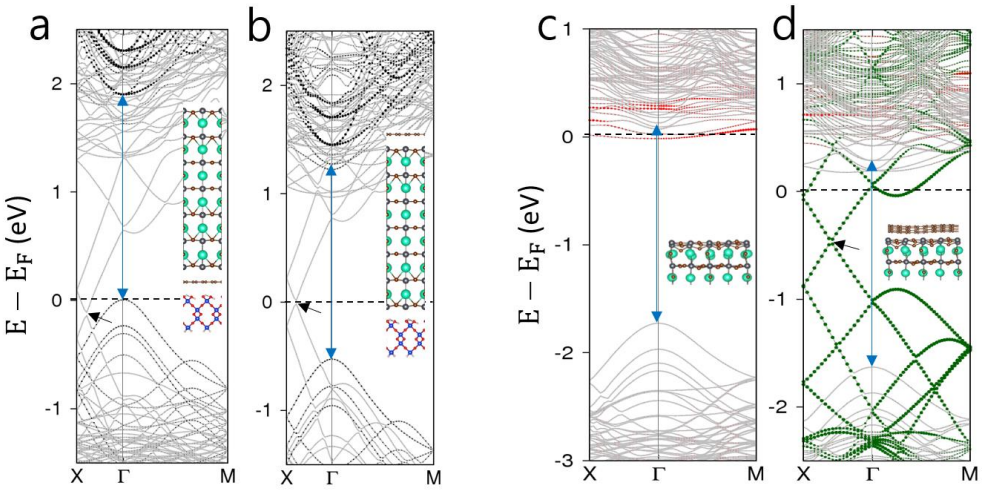

Figure 6.6: Calculated band structure of (a) $sPbBr_3$/Gr/SiO_2 (inset: side view along [100] of the model heterostructure). (b) Gr/ $CsPbBr_3$/ SiO_2. For easier recognition of the $CsPbBr_3$ band edges, the Pb bulk atom's 6p orbital contribution is shown by black circles. (c) $CsPbBr_3$ with a V_Br surface defect (inset: side view along [100] of the top 4 atomic layers of the model structure). (d) a defected $CsPbBr_3$/Gr interface (inset: side view along the [100] interface model structure with a perovskite top 4 atomic layers). Red circles show the contribution of the under-coordinated Pb atom below the V_Br site, and the carbon p_z orbital contribution is indicated by green circles. In all band structures, the electronic transition between the $CsPbBr_3$ band edges is indicated by the blue arrow. Gr's Dirac point is indicated by the black arrow in (a), (b), and (d). Atomic color scheme: Cs (green), Pb (gray), Br (brown), Si (blue), O (red), H (pink), C (brown).

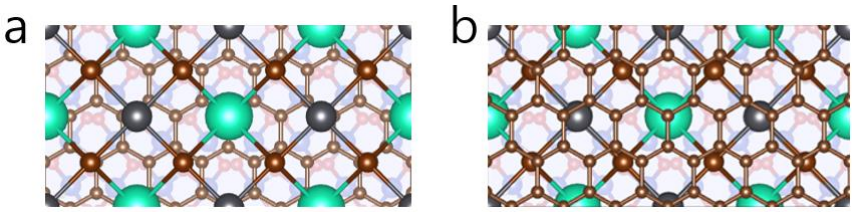

Figure 6.7: Top view of $2\times\sqrt{2}\times\sqrt{2}$ surface supercell of (a) $CsPbBr_3$/Gr/SiO_2, and (b) Gr/$CsPbBr_3$/SiO_2. Atomic color scheme: Cs (green), Pb (gray), Br (brown), Si (blue), O (red), H (pink), C (brown).

band minimum (CBM), which can act as a center for non-radiative recombination and suppress the PL intensity. However, after covering defected $CsPbBr_3$ with graphene, carbon p_z states hybridized with Pb dangling bond states and shifted them upward to the perovskite conduction band 6.6(d). Therefore, the Gr adsorption on the defected $CsPbBr_3$ surface eliminates non-radiative recombination centers leading to PL enhancement in the

Gr/ $CsPbBr_3$/ SiO_2 system. It should be noted that upon passivation of the VBr defect, the Gr is n-doped Figure6.6(d), with a charge density of $10^{13}\,cm^{-2}$ (Eq.6-4) [225]. Similar results are obtained for the Gr/ $CsPbBr_3$ interface consisting of the perovskite with a CsBr termination Figure6.8(a-b). Equation (6-4) relates the Dirac energy in electronic band structure to electron density in the Gr layer:

$$n_e = \frac{E_D^2}{\pi(\hbar.\upsilon_F)^2} \tag{6.4}$$

where υ_F is Fermi velocity. For $E_D = 0.5$ eV (from electronic band structure of Gr/defected-$CsPbBr_3$ interface Figure6.6(d) and $\upsilon_F = 1.12 \times 10^6$ m/s, the calculated n_e value is $10^{13}\,cm^{-2}$.

6.9.1 Electronic band structure of three-layered heterostructure considering $CsPbBr_3$ layer with CsBr and $PbBr_2$ terminations

Considering both CsBr and $PbBr_2$surface terminations of the perovskite layer, we calculated the ground state electronic band structure of four $CsPbBr_3$/graphene/SiO_2 in Figure 6.2(a-c) and Figure6.6(a) and four graphene/$CsPbBr_3$/SiO_2 model heterostructures (Figures6.2(d-e) and Figure 6.6(b)) to screen all possible interfacial interactions and their impact on the electronic structure. Among all $CsPbBr_3$/graphene/SiO_2 model heterostructures, the model including $CsPbBr_3$ (001) slab with $PbBr_2$ top and bottom terminations in Figure 6.6(a) showed considerable charge transfer at the graphene /$CsPbBr_3$ interface. However, none of the graphene/$CsPbBr_3$/SiO_2 model heterostructures showed interfacial charge transfer at $CSPbBr_3$/graphene interface in Figure 6.8.

Enhanced PL emission due to the resonant coupling between surface plasmon (SP) modes in a metallic layer and excitons in a semiconductor has been reported [74, 222, 226, 227]. Considering the semi-metallic nature of graphene, the significant PL enhancement of the Gr/$CsPbBr_3$/SiO_2 heterosystem could be understood in terms of the resonant excitation of graphene plasmon modes [210, 222, 228]. The perovskite's photo-generated excitons can induce resonant plasmon mode in the graphene layer. However, because of the considerable momentum mismatch between Gr's plasmon and photons in free space, a lateral modulation periodicity on the graphene [210, 229] or its substrate [222]

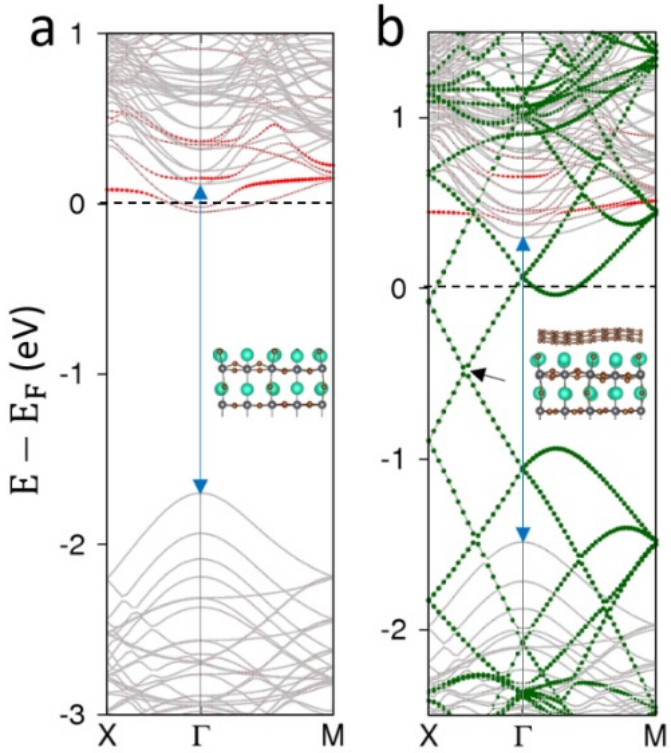

Figure 6.8: Calculated electronic band structure of (a)$PbBr_2$ terminated (001) $CsPbBr_3$ slab with V_Br surface defect (inset: side view along [100] of the top 4 atomic layers of model structure). (b) defected $CsPbBr_3$/Gr interface (inset: side view along [100] of interface model structure with perovskite top 4 atomic layers). Red circles show the contribution of two under-coordinated surface Pb atoms, and carbon p_z orbital contribution is indicated by green circles. In all band structures, $CsPbBr_3$ band edges are indicated by arrows. Atomic color scheme: Cs (green), Pb (gray), Br (brown), Si (blue), O (red), H (pink), C (brown).

is required to resolve the momentum mismatch and transform the excited plasmon mode to the light emission. The dispersion relation of the graphene plasmon in the random phase approximation is :

$$\omega(q) = \left(\frac{n_2 e^2}{\varepsilon_0 (1+\varepsilon_b) m^*} |q| \frac{3}{4} \upsilon_F^2 q^2 \right)^{1/2} \tag{6.5}$$

Where q is the in-plane wave number, n_e is the electron density, ε_0 is the vacuum permittivity, ε_b is the substrate static dielectric constant, m^* is electron effective mass in Gr, and υ_F is its Fermi velocity [222, 230, 231]. We supposed that the graphene plasmon could be resonantly excited at perovskite band gap energy of 2.3 eV and calculated the in-plane momentum q from our calculated $n_e = 10^{13}$ cm^{-2}, using $\varepsilon_b = 18.6$ for the $CsPbBr_3$ substrate [204, 232], $m^* = 0.077\, m_e$ [222] where m_e is the free electron mass, and

$\upsilon_F = 1.12 \times 10^6$ m/s [222]. We obtained $q = 2\pi/1.8\,\text{nm}^{-1}$, indicating a lateral modulation periodicity of $a = 1.8$ nm at the Gr/$CsPbBr_3$ interface would be required to extract light from the Gr's plasmon. Due to the V_Br defects, the surface structure of the $CsPbBr_3$ is distorted and not perfectly flat, resulting in interface corrugations on the order of a few nm. While it may not be feasible to measure $a = 1.8$ nm experimentally, this value is consistent with the lateral distance of 1.68 nm between V_Br surface defects in our model structure. Thus, the resonant activation of a Gr plasmon at the perovskite band gap, and its conversion to photons via interaction with interface surface corrugations, explains the observed PL enhancement for the Gr/$CsPbBr_3$/SiO_2 heterostructure.

6.10 Time-resolved Photoluminescence for bare $CsPbBr_3$ QDs (uncoated) and Gr-covered QDs.

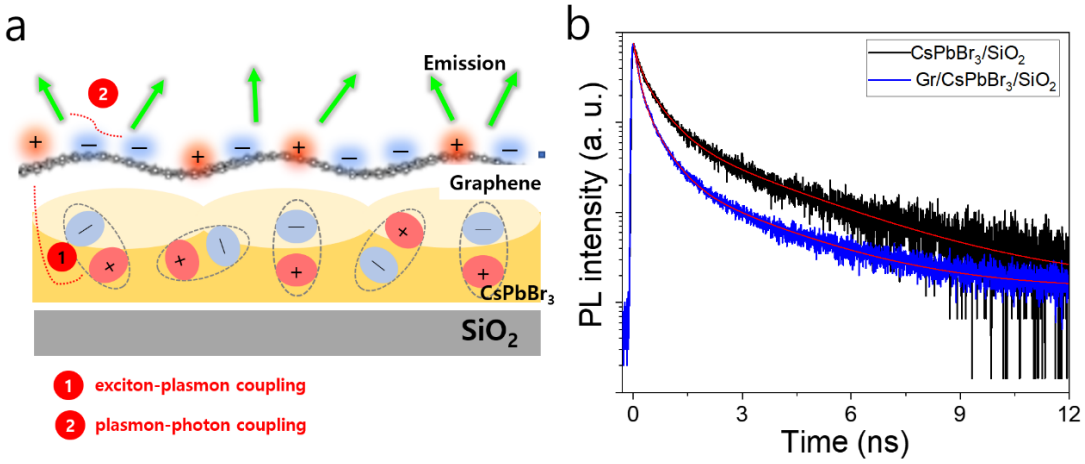

Figure 6.9: Time-resolved Photoluminescence. Time-resolved PL comparison for bare $CsPbBr_3$ QDs (uncoated) and Gr-covered QD cluster. The data of bare $CsPbBr_3$ and Gr-covered $CsPbBr_3$ are fitted with biexponential decays and the decay time are 0.61 ns and 0.14 ns for faster component and 2.96 ns and 3.26 ns for slow components, respectively. The TRPL measurement accuracy is 120 ps.

Resonant excitation of the graphene plasmon by the perovskite's photo-generated excitons, followed by its conversion to photons thorough interaction with the Gr/$CsPbBr_3$

interface corrugations, substantially enhances the PL intensity from Gr/$CsPbBr_3$/SiO_2 heterosystem Figure 6.9. In order to understand the dynamics of photoexcited carriers, time-resolved PL (TRPL) measurements were performed for the both bare $CsPbBr_3$ and Gr-coated $CsPbBr_3$ QDs Figure 6.9(b). The PL decay curves over time in both samples were fitted by a biexponential decay, as depicted by the red lines, which is indicating that there are two origins of the PL emission. The decay time of the bare $CsPbBr_3$ is $\sim$ 0.61 ns for the fast decay and $\sim$ 2.96 ns for the slow decay components. On the other hand, the decay time of the Gr covered $CsPbBr_3$ is $\sim$ 0.14 ns for the fast decay and $\sim$ 3.26 ns for the slow decay components, respectively which is dominated by direct exciton recombination for fast decay and related to shall trap-assisted recombination [233]. The major trap states are assumed to be the predominant V_Br and that changes the the Fermi level between perovskites and metal layer. Recently very similar decay curves were reported in Al metal covered Van der Waals contact on perovskite materials [234].

6.11 Kinetic series of the temporal response for bare $CsPbBr_3$ QDs (uncoated) and Gr-covered QDs

Figure 6.10(a) shows the separate PL lines emerging at very high excitation fluence measured by kinetic series measurement with a time resolution of 10 μs at initial and final states. It is clear from the spectrum that these carrier energy distribution profiles overlap with each other by more than 50% of the integrated area. Given that these individual PL lines are associated with multiple closely-related coupled QD matrices, charge transfer between these coupled systems is hence possible due to the almost coincidence of their energy profile. Since coupling from two QD matrices of sub-micrometer dimensions will take much longer than the intra-QD dynamics (within tens of nanosecond), we have investigated this effect at a time scale of milliseconds. This is a reasonable scale as charging/discharging related 'blinking' process in these inorganic halide perovskite nanocrystals can be studied with even longer time windows at an order of seconds.

Figure 6.10(b) presents the kinetics series taken for the same site under continuous exposure with a time resolution of 10 μs. The entire time series can be divided into two halves as shown in Figures6.10(c-d). In the first 30 μs, the 2.311 eV line gradually splits

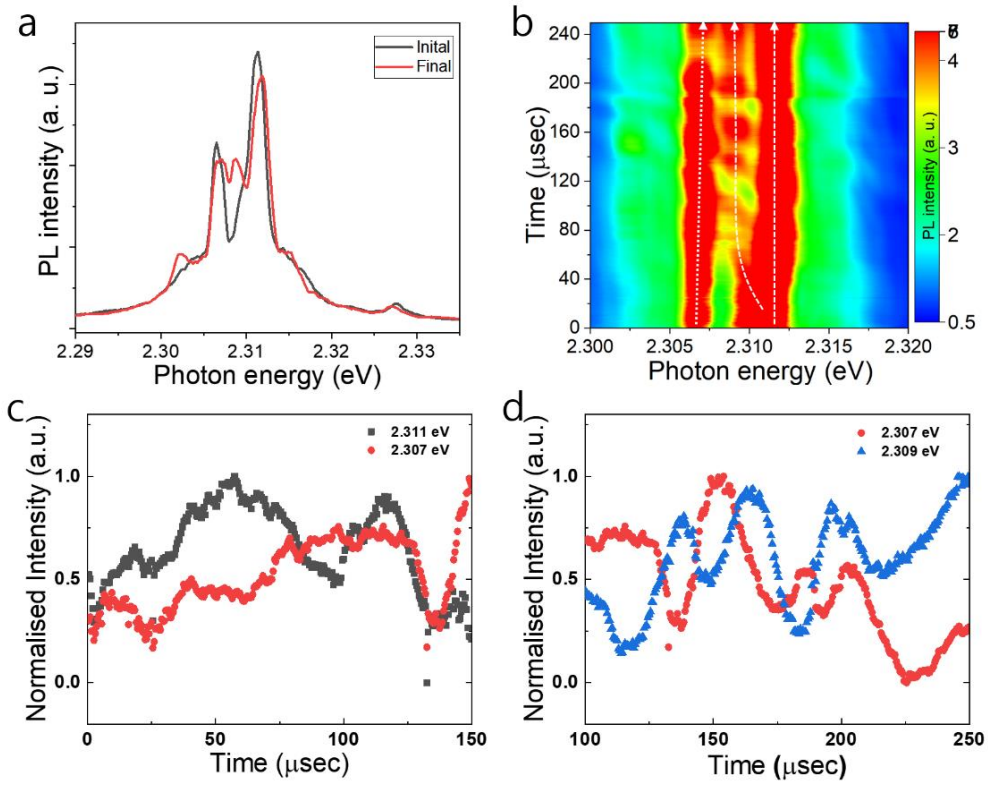

Figure 6.10: Kinetic series showing the temporal response. (a) PL spectra at the initial and final states. (b) time series counter plot taken with a step of 10 μs for 6 s. In the first 30 μs, the 2.311 eV line gradually splits into two individual lines at 2.312 eV and 2.309 eV respectively. (c) Comparison of the temporal evolution for the integrated intensity between the initial emission centers at 2.311 eV and 2.307 eV in the first 1.5 μs, no significant pattern is observed. (d) Comparison of the temporal evolution for the integrated intensity between the newly split emission center at 2.309 eV and the original red site at 2.307 eV. The two emissions are switching with a period of 250 μs.

into two emission sites at 2.311 eV and 2.309 eV respectively while the 2.307 eV line stays fixed. After the splitting of the bluer emission state, the newly emergent 2.309 eV line demonstrates a switching phenomenon with the 2.307 eV line, as shown in Figure 6.9(d). The blue line at 2.311 eV shows negligible switching effect. The observed switching can be linked to charge carrier movements between two large blocks of coupled QD systems. The oscillation indicates that the process is completely reversible and not subject to any permanent segregation effect to the chemical structure. It is also logical to infer that the initial splitting of the higher-energy line is due to the interaction with the QD matrix

sitting at the redder site, which induces the coupled system from 2.311 eV to break up into a higher energy subsystem and a lower energy subsystem to be coupled to itself.

6.12 Conclusion

Three different LHP heterojunctions were studied in this chapter involving bare $CsPbBr_3$ QDs /SiO_2,$CsPbBr_3$ QDs/graphene/SiO_2 and graphene/$CsPbBr_3$QDs/SiO_2. Using a graphene (Gr) sheet hybridized with $CsPbBr_3$ has improved optoelectronic performance, and these particular materials show improved stability and dramatic PL enhancement compared to other conventional semiconductors. Micro-photoluminescence spectroscopy measurements were carried out over a range of powers for all three LHP heterojunctions at 4.2 K. The integrated intensity of the emission of the bare $CsPbBr_3$ QDs was identified as an S-shaped behaviour suggesting stimulated emission, whereas the PL intensity of the $CsPbBr_3$/Gr/SiO_2 heterostructure was quenched. However, the integrated PL intensity of the Gr-covered $CsPbBr_3$ QDs shows a linear dependence with excitation power and significant PL enhancements. The DFT calculations were implemented to calculate the electronic structure of the $CsPbBr_3$/Gr/SiO_2 heterostructure. The $CsPbBr_3$ layer shows a direct band gap of 1.9 eV located at the Γ-point.

The cause of the quenching of the (PL) intensity in the $CsPbBr_3$/Gr/SiO_2 heterostructure has been determined to be the transfer of electrons from the $CsPbBr_3$ to the graphene (Gr). This is shown by the presence of the Dirac point below the Fermi level, which suggests that the graphene is n-doped. The Gr/$CsPbBr_3$/SiO_2 heterostructure was also simulated to investigate the cause of photoluminescence (PL) intensity enhancement. The $CsPbBr_3$ layer has a direct band gap of 1.80 eV at the Γ-point, while Gr's Dirac cone was positioned between the Γ and X points. The results indicated that three distinct factors could potentially induce the enhancement of photoluminescence (PL) intensity in the Gr/$CsPbBr_3$/SiO_2 hetero system. The first factor refers to the interaction with the SiO_2 interface dipole, which elevates the work function of $CsPbBr_3$, resulting in a downward displacement of its valence band maximum (VBM) and conduction band minimum (CBM). Consequently, this increased the electrostatic potential barrier at the interface, preventing the leakage of carriers from the perovskite layer to Gr. As a result, radiative

recombination rises compared to the $CsPbBr_3/Gr/SiO_2$ heterostructure. Moreover, the surface stabilizing effect occurs when defective $CsPbBr_3$ is covered with graphene (Gr), causing the carbon p_z states to hybridize with the Pb dangling bond states and move them upwards to the perovskite conduction band. Hence, the adsorption of Gr on the defective $CsPbBr_3$ surface effectively reduces non-radiative recombination centres.

The observed enhancement in (PL) for the $Gr/CsPbBr_3/SiO_2$ heterostructure can also be attributed to the resonant activation of the graphene (Gr) plasmon at the perovskite band gap. This plasmon is then converted to photons by interacting with surface corrugations at the interface. The experimental and theoretical studies demonstrated that the presence of graphene covering plays a crucial role in significantly enhancing the photoluminescence (PL) of $CsPbBr_3$.This finding could be utilized in the development of very luminous light-emitting diodes.

7 Conclusions

Contents

7.1 Introduction

This chapter will summarize the conclusions of this thesis. It will also provide some ideas and opportunities for improving the efficiency and performance of solar cells and diodes by using mixed-halide perovskite materials as active layers or absorbers. This chapter will also elucidate the significance of passivation methods in the coating of mixed-halide perovskites to enhance charge transport in solar cells or other applications that necessitate pure-color light emission. Moreover, it will discuss the potential feasibility of using graphene-perovskite interfaces and their impact on optimizing the perovskite interfaces, enhancing charge extraction, reducing recombination losses, and enhancing the overall efficiency of electronic devices.

7.2 Conclusion

In the first part of this thesis that represented in chapter 4 that investigated the microscopic processes occurring during halide segregation in $CsPbBrI_2$ films using combined spectroscopic measurements at room and cryogenic temperatures. We have put forward a passivation strategy for mitigating the halide migration of Br/I ions in the films by overcoating with a cyclic olefin copolymer (COC). We found that COC treatment optimizes the grain size in the threshold size range between 168 to 47.33 nm, thus increasing the activation energy barrier of ion migration from 20 to 28 meV. Room temperature time-dependent PL profiles at increasing excitation intensities showed that (i) the excitation threshold intensity induced phase-segregation decreases, (ii) the band gap difference between decreases, and (iii) the dominance of the entropy demixing halide ions driven by the kinetics of halide vacancy and polaron accumulation is reduced after coating. The entropy remixing halide ions and higher photostability against phase segregation are dominant at cryogenic temperatures (4.2 K).

Followed by monitoring halide ion mobility through photoinduced halide separation and dark recovery after reducing the dimensionality of mixed halide perovskites from films to nanocrystals in Chapter 5. Our results demonstrate a strategy for achieving long-term stability of the pure-red emission through the use of mixed-halide $CsPbI_2Br$ PNCs encapsulated in polymer COC. Experimental observations demonstrated that COC not only passivates uncoordinated surface (Pb and I/Br) defects and reduces I^- ion species but also increases the formation energy of halide vacancies. Moreover, the encapsulation of these materials can drive electron transfer from the $CsPbI_2Br$ PNCs to the COC, which extends the lifetime of charge carriers, and reduces non-radiative recombination rates. These results help to understand the causes of photodecomposition and highlight the function of halide vacancy passivation in increasing the stability of mixed halide $CsPbI_2Br$ PNCs compared to film counterparts, thus provide a better approach for fabricating highly efficient pure red LEDs using NCs/polymer matrices

The optical characterization of uncoated $CsPbBr_3$ QDs and graphene-coated $CsPbBr_3$ QDs through microphotoluminescence measurements and density functional theory

calculations was also examined in Chapter 6. Compared with bare $CsPbBr_3$ QDs, the PL intensity of the Gr-covered $CsPbBr_3$ QDs was dramatically enhanced by three orders of magnitude. The DFT calculation results showed that contacting Gr on the top side of $CsPbBr_3$ caused the Dirac point to appear at the centre of the $CsPbBr_3$ energy gap, in contrast to the Fermi level pinning behaviour to the valence band edge reported for bottom side contact as in $CsPbBr_3$/Gr/SiO_2. Thus, carrier leakage was prevented for the Gr-covered $CsPbBr_3$ with a high radiative recombination rate. In addition, the perovskite's surface defects were passivated via graphene covering, suppressing the non-radiative recombination of photo-generated charge carriers compared to uncovered perovskite QDs. Furthermore, resonant excitation of graphene plasmon by the perovskite's photo-generated excitons, followed by its conversion to photons through interaction with graphene/$CsPbBr_3$ interface corrugations, substantially enhanced the photoluminescence from graphene/$CsPbBr_3$/SiO_2 heterosystem. The experimental and theoretical investigations showed the significant role of graphene covering for dramatic PL enhancement of $CsPbBr_3$, which can be implemented for developing super bright light-emitting diodes.

The main drawback of the investigations above is their need for practical application, as the results were obtained at very low temperatures. In addition, industry-standard applications require more reliable operation systems and highly efficient devices operating in ambient conditions. However, additional chemical manipulations, such as ligand-related operations or encapsulation, can be incorporated to increase the system's stability and preserve these properties at high temperatures. Moreover, these results assist in a deep understanding of the nanoscopic performance and degradation landscape in all complex lead halides and provide a promising technical route for fabricating highly efficient optoelectronic applications.

7.3 Outlook and the future perspectives

The continuous effort to improve the stability of metal halide perovskites has paved the way for more advanced optoelectronic applications and opened up numerous research avenues in this area. Although significant advancements have been made, perovskites have yet to reach their maximum efficiency when applied to optoelectronic devices

involving solar cells and light-emitting diodes (LEDs).For instance, beyond the absorber layer, charge transport contacts and their interfaces with the active layer are of equal significance in perovskite photovoltaic devices, specifically in the context of perovskite solar cells that aim to achieve exceptional stability and efficiency. Here is a summary of anticipated future developments regarding the main topics of the thesis.

The results in this thesis demonstrate a unique passivation method involving COC and graphene to passivate non-radiative recombination pathways, enhancing luminescence efficiencies in perovskite films and nanocrystals. The results describe how excess halides are trapped at grain boundaries or surfaces to prevent halide migration and reduce non-radiative decay caused by interstitial halides. Further study on COC passivation and graphene needs to be conducted to assess its efficacy using different perovskite compositions, deposition techniques and contacts. In addition, how such an approach might eventually be used to prevent ionic migration and interfacial non-radiative losses or even replicated using different halide-sequestering agents. With high radiative efficiency, good charge transport, and photostable bandgaps, these passivisation methods are promising for taking perovskite devices to their efficiency limits across bandgaps.

Appendices

A
Appendix

Contents

A.1 Analysis of X-ray Diffraction Peaks

Chapter 4 studied X-ray broadening, crystallite sizes and lattice strain on the peak broadening of $CsPbBrI_2$ perovskite films using Williamson-Hall (W-H) analysis and size-strain plot. It is well known that the X-ray diffraction peaks broaden in perovskites due to structural imperfections and deviations from ideal crystallinity in all directions. Two main parameters can be extracted from the peak width analysis involving the crystallite size and lattice strain. It is worth mentioning that the particle size is unlikely to correspond to the crystallite size because of the polycrystalline aggregate formation [235]. The crystal defects can be quantified by analyzing the variations in lattice constants. In addition, the strain involves many factors such as contact, grain boundaries, triple junction and stacking faults [235]. In other words, the Bragg peak is influenced by the crystallites' size and the strain in the lattice. These factors can cause an increase in the width and intensity of the X-ray diffraction peaks, resulting in a corresponding shift in the position

of the peak at 2θ. Therefore, the crystallite size changes inversely with the cosine of θ, while the strain changes with the tangent of θ based on the width of the peak. The influence of size and strain on the broadening of the diffraction peaks can be determined based on the difference of 2θ. For this reason, W-H analysis is a method that can measure the integral broadenings of X-ray diffraction peaks resulting from size or strain effects by analyzing the peak width as a function of 2θ [236].

Williamson-Hall Methods

The relationship between the crystal imperfections in $CsPbBrI_2$ films and the distortion of strain-induced broadening of X-ray diffraction peaks as follows:

$$\varepsilon = \frac{\beta_s}{\tan\theta} \tag{A.1}$$

Equation A.1 has an exceptional characteristic that is contingent upon the diffraction angle θ.The Scherrer equation is dependent on the reciprocal of the cosine of θ as $[1/\cos\theta]$, while the W-H approach is dependent on the tangent of θ as $[\tan\theta]$. The fundamental distinction was that microstrain and small crystallite size were both caused by microstructural factors that resulted in reflection broadening. The analysis of size and strain broadening is performed using Williamson and Hall method, taking into account various θ positions. The following formulas represent the Scherrer equation and ε.

$$\beta_{hkl} = \beta_S + \beta_D \tag{A.2}$$

$$\beta_{hkl} = \frac{k\lambda}{D\cos\theta} + 4\varepsilon\tan\theta \tag{A.3}$$

$$\beta_{hkl}\cos\theta = \frac{k\lambda}{D} + 4\varepsilon\sin\theta \tag{A.4}$$

Therefore, a $\beta\cos\theta$ represented in the y-axis is plotted with respect to $4\sin\theta$ shown in the x-axis in which the strain and particle size can estimated from the slope and y-intercept of the fitted line, respectively. Upon the calculations of the lattice parameters, the strain can induce the lattice shrinkage.

Size-Strain Plot Method

The Williamson-Hall plot has demonstrated that the line broadening was predominantly isotropic. The diffracting domains exhibited isotropy as a result of the microstrain contribution. The "size-strain plot" can be used to derive size-strain parameters. An advantage of this is that it reduces the significance of data obtained from reflections at sharp angles. This calculation assumes that the profile is represented by a Gaussian function for the "strain profile" and a Lorentzian function for the "crystallite size" [237].Hence,

$$(d_{hkl}\beta_{hkl}\cos\theta)^2 = \frac{k}{D}[(d_{hkl})^2\beta_{hkl}\cos\theta] + [\frac{\varepsilon}{2}]^2 \tag{A.5}$$

where k is a constant, $\frac{3}{4}$ represents the shape spherical particles, $d_{hkl}\beta_{hkl}\cos\theta$ can be taken form x-axis and y-axis respectively for all peaks of $CsPbBrI_2$ films with cubic-α-phase from $2\theta = 10^\circ$ to $2\theta = 50^\circ$. The particle size is determined by calculating the slope of the linearly fitted data, while the square root of the y-intercept provides the measure of strain. The particle size is determined by calculating the slope of the linearly fitted data, while the square root of the y-intercept provides the measure of strain.

XRD refinement using Fullprof software

This section illustrates the process of refining X-ray diffraction (XRD) data using a comprehensive software package called full-prof. In order to execute this package, three distinct files are required: the crystallography information data file, which serves as a reference model for the $CsPbBrI_2$ films ; the XRD data file, which must be collected at a very slow scan count rate; and the optional instrument response function (IRF) result file, which is utilized to analyze the microstructure property of the materials. Before beginning the 10-step XRD refinements process, it is advisable to do two preliminary processes: downloading the CIF file (COD/AMCSD) database and converting the CIF file to a PCR file. The CIF file can be simply obtained from the crystallographic information open data website by conducting a search using the chemical element pattern of the $CsPbBrI_2$ compositions, as depicted in the figure.(a). The XRD data file's intensity of XRD results was copied to a new Notepad file, and the initial range of 2θ was adjusted to 20.1, with a

step of almost 0.02, and a final 2θ range of 49.99. The duplicated file was then saved as data.dat format in the exact location of the downloaded CIF file and IRF files as illustrated in figure(b). It is advisable to begin by selecting the EDPCR icon from the tool panel in the full-Proffitt software to import and convert the CIF file into a PCR file.

Furthermore, the refinement and calculation of a powder diffraction profile were used from a general setting. The data can be modified by specifying the file path for the data. The data was collected using X-ray simulation, with a peak shape described by the Thompson-Cox-Hastings pseudo-Voigt profile function. The range was defined in terms of θ scales. The analysis involved the utilization of phase patterns, a structural model, and a refinement approach. The user provided a coefficient to calculate the weight percentage of the phase. The calculation type was specified as X-ray, and the peak shape was determined to be the Thompson-Cox-Hastings pseudo-Voigt profile function. The refinement pattern included approximately 15 cycle refinements and utilized forced termination shifts of less than 0.30. In addition, the criterion of convergence not applied (profile matching mode) was implemented. It is necessary to verify and save the imported data, including parameters such as background, instruments, atoms, and profile. Another file will be generated as a PCR file in the exact location (document) where the CIF file was downloaded. Upon execution of the software, the data file will be displayed.To attain a higher level of refinement, it might be necessary to follow a series of steps in a sequential manner as follows:

1. Scale factor: the terms mentioned are scale factor, zero point of the detector, first background parameter, and lattice constant, which need to be modified upon the sample condition. If the background is extremely noisy, adjust at least two background parameters or, preferably, correct the background using linear interpolation.

2. The adjustment of atomic positions and, eventually, an overall Debye-Waller factor is essential for analyzing high-temperature data.

3. The adjustments of the peak shape and asymmetry properties are desirable.

4. Modification of the atom occupancy may be required.

5. The entire temperature component has to be converted into an indivisible isotropic thermal parameter.

6. It is preferable to incorporate additional background characteristics if the background is being refined.

7. If the data quality meets requirements, refining the individual anisotropic thermal parameter is preferable.

8. For wavelength data, the parameters Sycos and/or Sysin are used to compensate for instrumental or physical aberrations that have a cosine or sine angular dependence, respectively.

9. The new CIF file (microstructure file) will then be generated, which will estimate the average apparent size and standard deviation and the average maximum strain and standard deviation (isotropy).

10. WinPLOTR can be downloaded and used to run the microstructure file in order to execute the average size strain and W-H plots.

A.2 Theory Of Optical Frequency Response of Metals

Electromagnetic waves in media

The interaction of electromagnetic waves with matter at optical frequencies is typically explained by the macroscopic Maxwell's equations.

$$\nabla \cdot \mathbf{D} = \rho_{\text{ext}} \tag{A.6}$$

$$\nabla \cdot \mathbf{B} = 0 \tag{A.7}$$

$$\nabla \times \mathbf{E} = -\frac{\partial \mathbf{B}}{\partial t} \tag{A.8}$$

$$\nabla \times \mathbf{H} = j_{\text{ext}} + \frac{\partial \mathbf{D}}{\partial t} \tag{A.9}$$

in which, D stands for the displacement of electric charge, E for the electric field, H for the magnetic field, B for the magnetic induction, j_{ext} for the current density, and ρ_{ext} for the charge density, In this context, the average of all fields defined in the

macroscopic Maxwell's equations is computed across regions that are considerably larger than atomic scales. The electric flux through a confined surface is proportional to the charge (monopoles are present), as explained in Equation (6-1). In contrast, Equation (6-2) is derived from the absence of magnetic monopoles. An alternating magnetic field induces an electric field and generates an electric current, according to Equation (6-3), which is also referred to as Faraday's law of induction. A magnetic field is generated by an electric current or an alternating electric flux, according to Ampere's law in Equation (6-4). Fundamentally, the electromagnetic properties of a specific material can be identified by its macroscopic polarization (P), and its magnetization (M), as described in references [213, 214]:

$$\mathbf{D} = \varepsilon_0 \mathbf{E} + \mathbf{P} \tag{A.10}$$

$$\mathbf{H} = \frac{1}{\mu_0}\mathbf{B} + \mathbf{M} \tag{A.11}$$

The permittivity and permeability of vacuum are represented by ε_0 and μ_0, respectively. For linear and isotropic media with local and instantaneous interactions, the material equations, sometimes referred to as the constitutive relations, take the following form:

$$\mathbf{D} = \varepsilon_0 \varepsilon_r \mathbf{E} \tag{A.12}$$

$$\mathbf{B} = \mu_0 \mu_r \mathbf{H} \tag{A.13}$$

$$\mathbf{j} = \sigma \mathbf{E} \tag{A.14}$$

ε_r and μ_r represent the relative dielectric constant and relative permeability, respectively. The constitutive relations assume that ε_r remains constant in Eq. (6-8) to Eq. (6-9). However, ε_r typically varies with frequency. Therefore, a detailed examination of the dispersion relation of ε_r is necessary for fully understanding the frequency response of metals.

The Drude model of the optical response

Drude model can be a straightforward representation of the dispersion relationship of ε_r. It is predicated on the existence of a free electron gas or plasma that perturbs a spatially stable ion core background. Free electrons initiate oscillations when subjected

to a time-harmonic electric field, denoted as $E(t) = E_0\, e^{-i\omega t}$, with a given frequency ω. The following expression characterizes the time-dependent motion of a single electron:

$$m_e\ddot{\mathbf{r}} + m_e\gamma\dot{\mathbf{r}} = -e\mathbf{E} \tag{A.15}$$

The electron charge is denoted by e, the electron collision frequency or attenuation (damping) constant is represented by γ, and the effective mass is denoted by m_e. By substituting $r(t) \simeq r_0 e^{-i\omega t}$ into Eq. (6-10), the macroscopic polarization of the metal can be identified by calculating the equation.

$$\mathbf{P} = -N_e e\mathbf{r} = \varepsilon_0(\varepsilon_r - 1)\mathbf{E} \tag{A.16}$$

N_e denotes the electron density of metals. As a result, the following equations describe the dielectric function of the free electron gas:

$$\varepsilon_r(\omega) = (1 - \omega_p^2)/(\omega^2 + i\gamma\omega) \tag{A.17}$$

$$\varepsilon_r(\omega) = (1 - (\omega_p^2/\omega^2 + \gamma^2) + i(\omega_p^2\gamma/\omega(\omega^2 + \gamma^2)) \tag{A.18}$$

where the first term represents the real part of the dielectric function Re(ε_r (ω)) and the second term denotes the imaginary part of the dielectric function Im (ε_r (ω)), respectively. Using the plasma frequency $\omega_p = \sqrt{\frac{e^2 N_e}{\varepsilon_0 m_e}}$. The real part of the dielectric function Re(ε_r (ω)) represents the optical response of charge oscillations in phase with the applied field. In contrast, the imaginary part Im (ε_r (ω)) describes the optical response of charge oscillations out of phase with the applied field. Thus, the imaginary component serves as an indicator of the loss.

References

[1] Akihiro Kojima et al. “Organometal halide perovskites as visible-light sensitizers for photovoltaic cells”. In: *Journal of the american chemical society* 131.17 (2009), pp. 6050–6051.

[2] Phillip J Dale and Michael A Scarpulla. “Efficiency versus effort: A better way to compare best photovoltaic research cell efficiencies?” In: *Solar Energy Materials and Solar Cells* 251 (2023), p. 112097.

[3] Letian Dou et al. “Solution-processed hybrid perovskite photodetectors with high detectivity”. In: *Nature communications* 5.1 (2014), p. 5404.

[4] Kebin Lin et al. “Perovskite light-emitting diodes with external quantum efficiency exceeding 20 per cent”. In: *Nature* 562.7726 (2018), pp. 245–248.

[5] Oscar A Jaramillo-Quintero et al. “Bright visible-infrared light emitting diodes based on hybrid halide perovskite with Spiro-OMeTAD as a hole-injecting layer”. In: *The journal of physical chemistry letters* 6.10 (2015), pp. 1883–1890.

[6] Isaac Suárez et al. “Polymer/perovskite amplifying waveguides for active hybrid silicon photonics”. In: *Advanced materials* 27.40 (2015), pp. 6157–6162.

[7] Isaac Suárez et al. “Integrated optical amplifier–photodetector on a wearable nanocellulose substrate”. In: *Advanced Optical Materials* 6.12 (2018), p. 1800201.

[8] Felix Deschler et al. “High photoluminescence efficiency and optically pumped lasing in solution-processed mixed halide perovskite semiconductors”. In: *The journal of physical chemistry letters* 5.8 (2014), pp. 1421–1426.

[9] Samuel D Stranks et al. “The physics of light emission in halide perovskite devices”. In: *Advanced materials* 31.47 (2019), p. 1803336.

[10] Feng Wang et al. “Defects engineering for high-performance perovskite solar cells”. In: *npj Flexible Electronics* 2.1 (2018), p. 22.

[11] Anton R Chakhmouradian and Patrick M Woodward. *Celebrating 175 years of perovskite research: a tribute to Roger H. Mitchell*. 2014.

[12] Ershad Sharifahmadian and Alireza Ahmadian. “Adaptive signal processing algorithm for remote detection of heart rate (HR) using ultra-wideband waveforms based on principal component analysis”. In: *Annual International Conference of the IEEE Engineering in Medicine and Biology Society*. 2009, pp. 5717–5720.

[13] Victor Moritz Goldschmidt. “Die gesetze der krystallochemie”. In: *Naturwissenschaften* 14.21 (1926), pp. 477–485.

[14] Matias Acosta et al. “BaTiO3-based piezoelectrics: Fundamentals, current status, and perspectives”. In: *Applied Physics Reviews* 4.4 (2017).

[15] Eugene A Katz. “Perovskite: name puzzle and German-Russian odyssey of discovery”. In: *Helvetica Chimica Acta* 103.6 (2020), e2000061.

[16] Yongbo Yuan et al. “Arising applications of ferroelectric materials in photovoltaic devices”. In: *Journal of Materials chemistry A* 2.17 (2014), pp. 6027–6041.

[17] Chr Kn Møller. “A phase transition in cæsium plumbochloride”. In: *Nature* 180.4593 (1957), pp. 981–982.

[18] David B Mitzi. “Organic- inorganic perovskites containing trivalent metal halide layers: the templating influence of the organic cation layer”. In: *Inorganic chemistry* 39.26 (2000), pp. 6107–6113.

[19] Aron Walsh. “Principles of chemical bonding and band gap engineering in hybrid organic–inorganic halide perovskites”. In: *The Journal of Physical Chemistry C* 119.11 (2015), pp. 5755–5760.

[20] Jason J Yoo et al. “Efficient perovskite solar cells via improved carrier management”. In: *Nature* 590.7847 (2021), pp. 587–593.

[21] Federico Brivio et al. “Relativistic quasiparticle self-consistent electronic structure of hybrid halide perovskite photovoltaic absorbers”. In: *Physical Review B* 89.15 (2014), p. 155204.

[22] Feng Xu et al. “Mixed cation hybrid lead halide perovskites with enhanced performance and stability”. In: *Journal of Materials Chemistry A* 5.23 (2017), pp. 11450–11461.

[23] Zhen Li et al. “Stabilizing perovskite structures by tuning tolerance factor: formation of formamidinium and cesium lead iodide solid-state alloys”. In: *Chemistry of Materials* 28.1 (2016), pp. 284–292.

[24] Chonghea Li et al. “Formability of abx3 (x= f, cl, br, i) halide perovskites”. In: *Acta Crystallographica Section B: Structural Science* 64.6 (2008), pp. 702–707.

[25] Xiaoming Li et al. “All inorganic halide perovskites nanosystem: synthesis, structural features, optical properties and optoelectronic applications”. In: *Small* 13.9 (2017), p. 1603996.

[26] Xiaoming Li et al. “CsPbX3 quantum dots for lighting and displays: room-temperature synthesis, photoluminescence superiorities, underlying origins and white light-emitting diodes”. In: *Advanced Functional Materials* 26.15 (2016), pp. 2435–2445.

[27] Loredana Protesescu et al. “Nanocrystals of cesium lead halide perovskites (CsPbX3, X= Cl, Br, and I): novel optoelectronic materials showing bright emission with wide color gamut”. In: *Nano letters* 15.6 (2015), pp. 3692–3696.

[28] T Markvart. “Semiclassical theory of non-radiative transitions”. In: *Journal of Physics C: Solid State Physics* 14.29 (1981), p. L895.

[29] Arthur Marronnier et al. “Influence of disorder and anharmonic fluctuations on the dynamical Rashba effect in purely inorganic lead-halide perovskites”. In: *The Journal of Physical Chemistry C* 123.1 (2018), pp. 291–298.

[30] Quyet Van Le et al. “Investigation of energy levels and crystal structures of cesium lead halides and their application in full-color light-emitting diodes”. In: *Advanced Electronic Materials* 3.1 (2017), p. 1600448.

[31] Zhuo Yang et al. “Impact of the halide cage on the electronic properties of fully inorganic cesium lead halide perovskites”. In: *ACS Energy letters* 2.7 (2017), pp. 1621–1627.

[32] Claudine Katan, Nicolas Mercier, and Jacky Even. "Quantum and dielectric confinement effects in lower-dimensional hybrid perovskite semiconductors". In: *Chemical reviews* 119.5 (2019), pp. 3140–3192.

[33] Gerasimos Konstantatos. *Colloidal quantum dot optoelectronics and photovoltaics*. Cambridge University Press, 2013.

[34] A Paul Alivisatos. "Perspectives on the physical chemistry of semiconductor nanocrystals". In: *The Journal of Physical Chemistry* 100.31 (1996), pp. 13226–13239.

[35] Dmitri V Talapin et al. "Prospects of colloidal nanocrystals for electronic and optoelectronic applications". In: *Chemical reviews* 110.1 (2010), pp. 389–458.

[36] Louis Brus. "Electronic wave functions in semiconductor clusters: experiment and theory". In: *The Journal of Physical Chemistry* 90.12 (1986), pp. 2555–2560.

[37] Arthur Marronnier et al. "Anharmonicity and disorder in the black phases of cesium lead iodide used for stable inorganic perovskite solar cells". In: *ACS nano* 12.4 (2018), pp. 3477–3486.

[38] Rebecca J Sutton et al. "Bandgap-tunable cesium lead halide perovskites with high thermal stability for efficient solar cells". In: *Advanced Energy Materials* 6.8 (2016), p. 1502458.

[39] Yiliu Wang et al. "Chemical vapor deposition growth of single-crystalline cesium lead halide microplatelets and heterostructures for optoelectronic applications". In: *Nano Research* 10 (2017), pp. 1223–1233.

[40] Sergiu Draguta et al. "Rationalizing the light-induced phase separation of mixed halide organic–inorganic perovskites". In: *Nature communications* 8.1 (2017), p. 200.

[41] Niraj N Lal, Thomas P White, and Kylie R Catchpole. "Optics and light trapping for tandem solar cells on silicon". In: *IEEE Journal of Photovoltaics* 4.6 (2014), pp. 1380–1386.

[42] Yutao Wang et al. "Phase segregation in inorganic mixed-halide perovskites: from phenomena to mechanisms". In: *Photonics research* 8.11 (2020), A56–A71.

[43] Constantinos C Stoumpos et al. "Crystal growth of the perovskite semiconductor CsPbBr3: a new material for high-energy radiation detection". In: *Crystal growth & design* 13.7 (2013), pp. 2722–2727.

[44] Giles E Eperon et al. "Inorganic caesium lead iodide perovskite solar cells". In: *Journal of Materials Chemistry A* 3.39 (2015), pp. 19688–19695.

[45] LC Thomas and Rosemary A Chittenden. "Characteristic infrared absorption frequencies of organophosphorus compounds—I The phosphoryl (P O) group". In: *Spectrochimica Acta* 20.3 (1964), pp. 467–487.

[46] Eric T Hoke et al. "Reversible photo-induced trap formation in mixed-halide hybrid perovskites for photovoltaics". In: *Chemical Science* 6.1 (2015), pp. 613–617.

[47] Parth Vashishtha and Jonathan E Halpert. "Field-driven ion migration and color instability in red-emitting mixed halide perovskite nanocrystal light-emitting diodes". In: *Chemistry of Materials* 29.14 (2017), pp. 5965–5973.

[48] Dieter Weber. "CH3NH3PbX3, ein Pb (II)-system mit kubischer perowskitstruktur/CH3NH3PbX3, a Pb (II)-system with cubic perovskite structure". In: *Zeitschrift für Naturforschung B* 33.12 (1978), pp. 1443–1445.

[49] Michael C Brennan et al. “Light-induced anion phase segregation in mixed halide perovskites”. In: *ACS Energy Letters* 3.1 (2017), pp. 204–213.

[50] Alex J Barker et al. “Defect-assisted photoinduced halide segregation in mixed-halide perovskite thin films”. In: *ACS Energy Letters* 2.6 (2017), pp. 1416–1424.

[51] Anthony Ruth et al. “Vacancy-mediated anion photosegregation kinetics in mixed halide hybrid perovskites: coupled kinetic Monte Carlo and optical measurements”. In: *ACS Energy Letters* 3.10 (2018), pp. 2321–2328.

[52] Simone Meloni et al. “Ionic polarization-induced current–voltage hysteresis in CH3NH3PbX3 perovskite solar cells”. In: *Nature communications* 7.1 (2016), p. 10334.

[53] Federico Brivio, Clovis Caetano, and Aron Walsh. “Thermodynamic origin of photoinstability in the CH3NH3Pb (I1–x Br x) 3 hybrid halide perovskite alloy”. In: *The journal of physical chemistry letters* 7.6 (2016), pp. 1083–1087.

[54] Tor Elmelund et al. “How interplay between photo and thermal activation dictates halide ion segregation in mixed halide perovskites”. In: *ACS Energy Letters* 5.1 (2019), pp. 56–63.

[55] Maksym V Kovalenko, Loredana Protesescu, and Maryna I Bodnarchuk. “Properties and potential optoelectronic applications of lead halide perovskite nanocrystals”. In: *Science* 358.6364 (2017), pp. 745–750.

[56] Quinten A Akkerman et al. “Tuning the optical properties of cesium lead halide perovskite nanocrystals by anion exchange reactions”. In: *Journal of the American Chemical Society* 137.32 (2015), pp. 10276–10281.

[57] Hyejin Choe et al. “Mixed or segregated: Toward efficient and stable mixed halide perovskite-based devices”. In: *ACS omega* 6.38 (2021), pp. 24304–24315.

[58] Alexander J. Knight and Laura M. Herz. “Preventing phase segregation in mixed-halide perovskites: A perspective”. In: *Energy and Environmental Science* 13.7 (2020), pp. 2024–2046.

[59] Yu Tian et al. “Highly efficient spectrally stable red perovskite light-emitting diodes”. In: *Advanced materials* 30.20 (2018), p. 1707093.

[60] Hyojung Kim et al. “Halide perovskites for applications beyond photovoltaics”. In: *Small Methods* 2.3 (2018), p. 1700310.

[61] Huan Wang and Dong Ha Kim. “Perovskite-based photodetectors: materials and devices”. In: *Chemical Society Reviews* 46.17 (2017), pp. 5204–5236.

[62] Connor G Bischak et al. “Origin of reversible photoinduced phase separation in hybrid perovskites”. In: *Nano letters* 17.2 (2017), pp. 1028–1033.

[63] Juvinch R Vicente and Jixin Chen. “Phase segregation and photothermal remixing of mixed-halide lead perovskites”. In: *The journal of physical chemistry letters* 11.5 (2020), pp. 1802–1807.

[64] Bernard Geffroy, Philippe Le Roy, and Christophe Prat. “Organic light-emitting diode (OLED) technology: materials, devices and display technologies”. In: *Polymer international* 55.6 (2006), pp. 572–582.

[65] Wenxin Mao et al. “Light-induced reversal of ion segregation in mixed-halide perovskites”. In: *Nature materials* 20.1 (2021), pp. 55–61.

[66] Alexander J. Knight et al. “Trap states, electric fields, and phase segregation in mixed-halide perovskite photovoltaic devices”. In: *Advanced Energy Materials* 10.9 (2020), p. 1903488.

[67] Daniel J. Slotcavage, Hemamala I. Karunadasa, and Michael D. McGehee. “Light-induced phase segregation in halide-perovskite absorbers”. In: *ACS Energy Letters* 1.6 (2016), pp. 1199–1205.

[68] Rebecca A Belisle et al. “Impact of surfaces on photoinduced halide segregation in mixed-halide perovskites”. In: *ACS Energy Letters* 3.11 (2018), pp. 2694–2700.

[69] Masaru Kuno and Michael C Brennan. “What exactly causes light-induced halide segregation in mixed-halide perovskites?” In: *Matter* 2.1 (2020), pp. 21–23.

[70] Jeffrey T DuBose and Prashant V Kamat. “TiO2-assisted halide ion segregation in mixed halide perovskite films”. In: *Journal of the American Chemical Society* 142.11 (2020), pp. 5362–5370.

[71] Gergely F Samu et al. “Electrochemical hole injection selectively expels iodide from mixed halide perovskite films”. In: *Journal of the American Chemical Society* 141.27 (2019), pp. 10812–10820.

[72] Ross A Kerner et al. “The role of halide oxidation in perovskite halide phase separation”. In: *Joule* 5.9 (2021), pp. 2273–2295.

[73] Eric T Hoke et al. “Reversible photo-induced trap formation in mixed-halide hybrid perovskites for photovoltaics”. In: *Chemical Science* 6.1 (2015), pp. 613–617.

[74] Yicheng Zhao et al. “Strain-activated light-induced halide segregation in mixed-halide perovskite solids”. In: *Nature communications* 11.1 (2020), pp. 1–9.

[75] Rachel E Beal et al. “Cesium lead halide perovskites with improved stability for tandem solar cells”. In: *The journal of physical chemistry letters* 7.5 (2016), pp. 746–751.

[76] Alexander J Knight et al. “Electronic traps and phase segregation in lead mixed-halide perovskite”. In: *ACS Energy Letters* 4.1 (2018), pp. 75–84.

[77] Alexander J Knight and Laura M Herz. “Preventing phase segregation in mixed-halide perovskites: a perspective”. In: *Energy and Environmental Science* 13.7 (2020), pp. 2024–2046.

[78] Ross A Kerner et al. “The role of halide oxidation in perovskite halide phase separation”. In: *Joule* 5.9 (2021), pp. 2273–2295.

[79] Michael C Brennan et al. “Photolysis of Mixed Halide Perovskite Nanocrystals”. In: *ACS Energy Letters* 8.5 (2023), pp. 2150–2158.

[80] Lyubov A Frolova et al. “Reversible Pb2+/Pb0 and I-/I3- redox chemistry drives the light-induced phase segregation in all-inorganic mixed halide perovskites”. In: *Advanced Energy Materials* 11.12 (2021), p. 2002934.

[81] Rebecca A Belisle et al. “Impact of surfaces on photoinduced halide segregation in mixed-halide perovskites”. In: *ACS Energy Letters* 3.11 (2018), pp. 2694–2700.

[82] Yang Zhou et al. “Composition-tuned wide bandgap perovskites: From grain engineering to stability and performance improvement”. In: *Advanced Functional Materials* 28.35 (2018), p. 1803130.

[83] R Geetha Balakrishna, Steven M Kobosko, and Prashant V Kamat. “Mixed halide perovskite solar cells. Consequence of iodide treatment on phase segregation recovery”. In: *ACS Energy Letters* 3.9 (2018), pp. 2267–2272.

[84] Alex J Barker et al. “Defect-assisted photoinduced halide segregation in mixed-halide perovskite thin films”. In: *ACS Energy Letters* 2.6 (2017), pp. 1416–1424.

[85] Connor G Bischak et al. “Tunable polaron distortions control the extent of halide demixing in lead halide perovskites”. In: *The journal of physical chemistry letters* 9.14 (2018), pp. 3998–4005.

[86] Jae S. Yun et al. “Critical role of grain boundaries for ion migration in formamidinium and methylammonium lead halide perovskite solar cells”. In: *Advanced Energy Materials* 6.13 (2016), p. 1600330.

[87] Andrés F Gualdrón-Reyes et al. “Controlling the phase segregation in mixed halide perovskites through nanocrystal size”. In: *ACS Energy Letters* 4.1 (2018), pp. 54–62.

[88] Xi Wang et al. “Suppressed phase separation of mixed-halide perovskites confined in endotaxial matrices”. In: *Nature communications* 10.1 (2019), p. 695.

[89] Jifeng Yuan et al. “Surface trap states passivation for high-performance inorganic perovskite solar cells”. In: *Solar Rrl* 2.10 (2018), p. 1800188.

[90] Jun-Nan Yang et al. “Potassium bromide surface passivation on CsPbI3-xBr x nanocrystals for efficient and stable pure red perovskite light-emitting diodes”. In: *Journal of the American Chemical Society* 142.6 (2020), pp. 2956–2967.

[91] Ziming Wang et al. “Laser induced ion migration in all-inorganic mixed halide perovskite micro-platelets”. In: *Nanoscale Advances* 1.11 (2019), pp. 4459–4465.

[92] Ursula Keller. “Ultrashort Time Optics: An Overview”. In: *Photons and Local Probes* (1995), pp. 295–305.

[93] PA Franken AE Hill CW Peters and G Weinreich. “Generation of optical harmonics”. In: *Phys. Rev. Lett* 7.4 (1961), pp. 118–119.

[94] RH Stolen and A Ashkin. “Optical Kerr effect in glass waveguide”. In: *Applied Physics Letters* 22.6 (1973), pp. 294–296.

[95] David E Spence, P Np Kean, and Wilson Sibbett. “60-fsec pulse generation from a self-mode-locked Ti: sapphire laser”. In: *Optics letters* 16.1 (1991), pp. 42–44.

[96] P-T Ho et al. “Picosecond pulse generation with a cw GaAlAs laser diode”. In: *Applied Physics Letters* 33.3 (1978), pp. 241–242.

[97] Wilfried Neumann. *Fundamentals of dispersive optical spectroscopy systems*. 2014.

[98] Saad Ullah et al. “All-Inorganic $CsPbI_2Br$ Perovskite Solar Cells: Recent Developments and Challenges”. In: *Energy Technology* 9.12 (2021), p. 2100691.

[99] Liuwen Tian, Jingjing Xue, and Rui Wang. “Halide Segregation in Mixed Halide Perovskites: Visualization and Mechanisms”. In: *Electronics* 11.5 (2022), p. 700.

[100] Yutao Wang et al. “Phase segregation in inorganic mixed-halide perovskites: from phenomena to mechanisms”. In: *Photonics Research* 8.11 (2020), A56–A71.

[101] Zhiyong Liu et al. “Efficient carbon-based $CsPbBr_3$ inorganic perovskite solar cells by using Cu-phthalocyanine as hole transport material”. In: *Nano-micro letters* 10.2 (2018), pp. 1–13.

[102] Beilei Yuan et al. "PMMA passivated $CsPbI_2Br$ perovskite film for highly efficient and stable solar cells". In: *Journal of Physics and Chemistry of Solids* 153 (2021), p. 110000.

[103] Wenming Chai et al. "Suppressing Halide Phase Segregation in $CsPbIBr_2$ Films by Polymer Modification for Hysteresis-Less All-Inorganic Perovskite Solar Cells". In: *ACS Applied Materials & Interfaces* 13.2 (2021), pp. 2868–2878.

[104] Wei Li et al. "Phase segregation enhanced ion movement in efficient inorganic CsPbIBr2 solar cells". In: *Advanced Energy Materials* 7.20 (2017), p. 1700946.

[105] Georgian Nedelcu et al. "Fast anion-exchange in highly luminescent nanocrystals of cesium lead halide perovskites (CsPbX3, X= Cl, Br, I)". In: *Nano letters* 15.8 (2015), pp. 5635–5640.

[106] Dongliang Bai et al. "Interstitial Mn_2^+ driven high-aspect-ratio grain growth for low-trap-density microcrystalline films for record efficiency $CsPbI_2Br$ solar cells". In: *ACS Energy Letters* 3.4 (2018), pp. 970–978.

[107] Federico Brivio, Clovis Caetano, and Aron Walsh. "Thermodynamic origin of photoinstability inthe $CH_3NH_3Pb(I_1-xBrx)_3$ hybrid halide perovskite alloy". In: *The journal of physical chemistry letters* 7.6 (2016), pp. 1083–1087.

[108] Xi Wang et al. "Suppressed phase separation of mixed-halide perovskites confined inendotaxial matrices". In: *Nature communications* 10.1 (2019), pp. 1–7.

[109] Tor Elmelund et al. "How interplay between photo and thermal activation dictates halide ion segregation in mixed halide perovskites". In: *ACS Energy Letters* 5.1 (2019), pp. 56–63.

[110] Sergiu Draguta et al. "Rationalizing the light-induced phase separation of mixed halide organic–inorganic perovskites". In: *Nature communications* 8.1 (2017), pp. 1–8.

[111] Michael C Brennan et al. "Photoinduced anion segregation in mixed halide perovskites". In: *Trends in Chemistry* 2.4 (2020), pp. 282–301.

[112] Ilia M Pavlovetc et al. "Distinguishing Models for Mixed Halide Lead Perovskite Photosegregation via Terminal Halide Stoichiometry". In: *ACS Energy Letters* 6.6 (2021), pp. 2064–2071.

[113] Gee Yeong Kim et al. "Photo-Effect on Ion Transport in Mixed Cation and Halide Perovskites and Implications for Photo-Demixing". In: *Angewandte Chemie* 133.2 (2021), pp. 833–839.

[114] Michael C Brennan et al. "Light-induced anion phase segregation in mixed halide perovskites". In: *ACS Energy Letters* 3.1 (2017), pp. 204–213.

[115] Long Hu et al. "Linking phase segregation and photovoltaic performance of mixed-halide perovskite films through grain size engineering". In: *ACS Energy Letters* 6.4 (2021), pp. 1649–1658.

[116] Zehua Chen et al. "Unified theory for light-induced halide segregation in mixed halide perovskites". In: *Nature communications* 12.1 (2021), p. 2687.

[117] Junsang Cho et al. "Photoinduced halide segregation in Ruddlesden–Popper 2D mixed halide perovskite films". In: *Advanced Materials* 33.48 (2021), p. 2105585.

[118] Jiang Tang et al. "Quantum dot photovoltaics in the extreme quantum confinement regime: the surface-chemical origins of exceptional air-and light-stability". In: *ACS nano* 4.2 (2010), pp. 869–878.

[119] Zhaobing Zeng et al. “In situ grain boundary functionalization for stable and efficient inorganic $CsPbI_2Br$ perovskite solar cells”. In: *Advanced Energy Materials* 8.25 (2018), p. 1801050.

[120] Yujing Hu et al. “Encapsulation of colloid perovskite nanocrystals into solid polymer matrices: Impact on electronic transition and photoluminescence”. In: *Journal of Luminescence* 219 (2020), p. 116938.

[121] Yuxiao Guo. “Photoinduced self-healing of halide segregation in mixed-halide perovskites”. In: *ACS Energy Letters* 6 (2021), pp. 2502–2511.

[122] Mojtaba Abdi-Jalebi et al. “Maximizing and stabilizing luminescence from halide perovskites with potassium passivation”. In: *Nature* 555.7697 (2018), pp. 497–501.

[123] Klara Suchan et al. “Multi-Stage Phase-Segregation of Mixed Halide Perovskites under Illumination: A Quantitative Comparison of Experimental Observations and Thermodynamic Models”. In: *Advanced Functional Materials* 33.3 (2023), p. 2206047.

[124] Qiuju Han et al. “Temperature-dependent photoluminescence of $CsPbX_3$ nanocrystal films”. In: *Journal of Luminescence* 198 (2018), pp. 350–356.

[125] Benjamin J Foley et al. “Temperature dependent energy levels of methylammonium lead iodide perovskite”. In: *Applied physics letters* 106.24 (2015), p. 243904.

[126] Hiroki Kawai et al. “The mechanism of slow hot-hole cooling in lead-iodide perovskite: first-principles calculation on carrier lifetime from electron–phonon interaction”. In: *Nano letters* 15.5 (2015), pp. 3103–3108.

[127] Silvia G Motti et al. “Phase segregation in mixed-halide perovskites affects charge-carrier dynamics while preserving mobility”. In: *Nature communications* 12.1 (2021), pp. 1–9.

[128] Zehua Chen et al. “Unified theory for light-induced halide segregation in mixed halide perovskites”. In: *Nature communications* 12.1 (2021), pp. 1–10.

[129] Chen Chen et al. “Polyacrylonitrile-Coordinated Perovskite Solar Cell with Open-Circuit Voltage Exceeding 1.23 V”. In: *Angewandte Chemie International Edition* 61.8 (2022), e202113932.

[130] Jingru Zhang et al. “Defects in CsPbX3 Perovskite: From Understanding to Effective Manipulation for High-Performance Solar Cells”. In: *Small Methods* 5.11 (2021), p. 2100725.

[131] Jing Wang et al. “Highly efficient all-inorganic perovskite solar cells with suppressed non-radiative recombination by a Lewis base”. In: *Nature communications* 11.1 (2020), pp. 1–9.

[132] Sawanta S Mali, Jyoti V Patil, and Chang Kook Hong. “Hot-air-assisted fully air-processed barium incorporated CsPbI2Br perovskite thin films for highly efficient and stable all-inorganic perovskite solar cells”. In: *Nano letters* 19.9 (2019), pp. 6213–6220.

[133] Mengjin Yang et al. “Do grain boundaries dominate non-radiative recombination in CH 3 NH 3 PbI 3 perovskite thin films?” In: *Physical Chemistry Chemical Physics* 19.7 (2017), pp. 5043–5050.

[134] Jae S Yun et al. “Benefit of grain boundaries in organic–inorganic halide planar perovskite solar cells”. In: *The journal of physical chemistry letters* 6.5 (2015), pp. 875–880.

[135] Richard Ciesielski et al. “Grain boundaries act as solid walls for charge carrier diffusion in large crystal MAPI thin films”. In: *ACS applied materials & interfaces* 10.9 (2018), pp. 7974–7981.

[136] Connor G Bischak et al. “Origin of reversible photoinduced phase separation in hybrid perovskites”. In: *Nano letters* 17.2 (2017), pp. 1028–1033.

[137] David T Limmer and Naomi S Ginsberg. “Photoinduced phase separation in the lead halides is a polaronic effect”. In: *The Journal of chemical physics* 152.23 (2020), p. 230901.

[138] Silvia G Motti et al. “Phase segregation in mixed-halide perovskites affects charge-carrier dynamics while preserving mobility”. In: *Nature communications* 12.1 (2021), pp. 1–9.

[139] Samuel D Stranks et al. “Electron-hole diffusion lengths exceeding 1 micrometer in an organometal trihalide perovskite absorber”. In: *Science* 342.6156 (2013), pp. 341–344.

[140] Wenhao Bai et al. “Perovskite light-emitting diodes with an external quantum efficiency exceeding 30%”. In: *Advanced Materials* 35.39 (2023), p. 2302283.

[141] Michael M. Lee et al. “Efficient Hybrid Solar Cells Based on Meso-Superstructured Organometal Halide Perovskites”. In: *Science* 338.6107 (2012), pp. 643–647.

[142] Samuel D. Stranks et al. “Electron-Hole Diffusion Lengths Exceeding 1 Micrometer in an Organometal Trihalide Perovskite Absorber”. In: *Science* 342.6156 (2013), pp. 341–344.

[143] Zhaohua Zhu et al. “Highly Efficient Sky-Blue Perovskite Light-Emitting Diode Via Suppressing Nonradiative Energy Loss”. In: *Chemistry of Materials* 33.11 (June 2021), pp. 4154–4162. URL: https://doi.org/10.1021/acs.chemmater.1c00903.

[144] Sandeep Pathak et al. “Perovskite Crystals for Tunable White Light Emission”. In: *Chemistry of Materials* 27.23 (Dec. 2015), pp. 8066–8075. URL: https://doi.org/10.1021/acs.chemmater.5b03769.

[145] Gabriele Rainò et al. “Ultra-narrow room-temperature emission from single CsPbBr3 perovskite quantum dots”. In: *Nature Communications* 13.1 (May 2022), p. 2587.

[146] Wei Zou et al. “Minimising efficiency roll-off in high-brightness perovskite light-emitting diodes”. In: *Nature Communications* 9.1 (Feb. 2018), p. 608.

[147] Jun-Nan Yang et al. “High Color Purity and Efficient Green Light-Emitting Diode Using Perovskite Nanocrystals with the Size Overly Exceeding Bohr Exciton Diameter”. In: *Journal of the American Chemical Society* 143.47 (Dec. 2021), pp. 19928–19937. URL: https://doi.org/10.1021/jacs.1c09948.

[148] Daniel J. Slotcavage, Hemamala I. Karunadasa, and Michael D. McGehee. “Light-Induced Phase Segregation in Halide-Perovskite Absorbers”. In: *ACS Energy Letters* 1.6 (Dec. 2016), pp. 1199–1205. URL: https://doi.org/10.1021/acsenergylett.6b00495.

[149] Huichao Zhang et al. “Phase segregation due to ion migration in all-inorganic mixed-halide perovskite nanocrystals”. In: *Nature Communications* 10.1 (Mar. 2019), p. 1088. URL: https://doi.org/10.1038/s41467-019-09047-7.

[150] Eric T. Hoke et al. “Reversible photo-induced trap formation in mixed-halide hybrid perovskites for photovoltaics”. In: *Chem. Sci.* 6 (1 2015), pp. 613–617.

[151] Lyubov A Frolova et al. “Reversible Pb2+/Pb0 and I-/I3- Redox Chemistry Drives the Light-Induced Phase Segregation in All-Inorganic Mixed Halide Perovskites”. In: *Advanced Energy Materials* 11.12 (2021), p. 2002934.

[152] Shangshang Chen et al. “Iodine reduction for reproducible and high-performance perovskite solar cells and modules”. In: *Science Advances* 7.10 (2021), eabe8130.

[153] Hongguang Meng et al. “Inhibition of halide oxidation and deprotonation of organic cations with dimethylammonium formate for air-processed p–i–n perovskite solar cells”. In: *Nature Energy* (2024), pp. 1–12.

[154] Michael C Brennan et al. “Superlattices are greener on the other side: how light transforms self-assembled mixed halide perovskite nanocrystals”. In: *ACS Energy Letters* 5.5 (2020), pp. 1465–1473.

[155] Huichao Zhang et al. “Phase segregation due to ion migration in all-inorganic mixed-halide perovskite nanocrystals”. In: *Nature Communications* 10.1 (2019).

[156] Shuai You et al. “Radical polymeric p-doping and grain modulation for stable, efficient perovskite solar modules”. In: *Science* 379.6629 (2023), pp. 288–294.

[157] Xiaofeng Tang et al. “Local observation of phase segregation in mixed-halide perovskite”. In: *Nano letters* 18.3 (2018), pp. 2172–2178.

[158] Qi Chen et al. “Controllable self-induced passivation of hybrid lead iodide perovskites toward high performance solar cells”. In: *Nano letters* 14.7 (2014), pp. 4158–4163.

[159] Zhe Li et al. “Beyond the Phase Segregation: Probing the Irreversible Phase Reconstruction of Mixed-Halide Perovskites”. In: *Advanced Science* 9.5 (2022), p. 2103948.

[160] Akriti et al. “Layer-by-layer anionic diffusion in two-dimensional halide perovskite vertical heterostructures”. In: *Nature Nanotechnology* 16.5 (2021), pp. 584–591.

[161] R Becker and Werner Döring. *Kinetic treatment of the nucleation in supersaturated vapors*. 1374. National Advisory Commitee for Aeronautics, 1954.

[162] Alasdair Brown. “Lead halide perovskite nanocrystals: enhancing commercial viability for light emitting applications”. PhD thesis. University of Southampton, 2020.

[163] Mutibah Alanazi et al. “Stability of Mixed Lead Halide Perovskite Films Encapsulated in Cyclic Olefin Copolymer at Room and Cryogenic Temperatures”. In: *The Journal of Physical Chemistry Letters* 14 (2023), pp. 11333–11341.

[164] Shengfan Wu et al. “Redox mediator-stabilized wide-bandgap perovskites for monolithic perovskite-organic tandem solar cells”. In: *Nature Energy* (2024), pp. 1–11.

[165] Max Karlsson et al. “Mixed halide perovskites for spectrally stable and high-efficiency blue light-emitting diodes”. In: *Nature communications* 12.1 (2021), p. 361.

[166] Yun Lin et al. “Suppressed ion migration in low-dimensional perovskites”. In: *ACS Energy Letters* 2.7 (2017), pp. 1571–1572.

[167] Nan Li et al. “Ion Migration in Perovskite Light-Emitting Diodes: Mechanism, Characterizations, and Material and Device Engineering”. In: *Advanced Materials* 34.19 (2022), p. 2108102.

[168] Jibin Zhang et al. “A Multifunctional “Halide-Equivalent” Anion Enabling Efficient CsPb (Br/I) 3 Nanocrystals Pure-Red Light-Emitting Diodes with External Quantum Efficiency Exceeding 23%”. In: *Advanced Materials* 35.8 (2023), p. 2209002.

[169] Xi Chen et al. “Substantial Improvement of Operating Stability by Strengthening Metal-Halogen Bonds in Halide Perovskites”. In: *Advanced Functional Materials* 32.22 (2022), p. 2112129.

[170] Ya-Kun Wang et al. “In Situ Inorganic Ligand Replenishment Enables Bandgap Stability in Mixed-Halide Perovskite Quantum Dot Solids”. In: *Advanced Materials* 34.21 (2022), p. 2200854.

[171] Yuanzhi Jiang et al. “Unraveling Size-Dependent Ion-Migration for Stable Mixed-Halide Perovskite Light-Emitting Diodes”. In: *Advanced Materials* 35.39 (2023), p. 2304094.

[172] Wei Li et al. “The critical role of composition-dependent intragrain planar defects in the performance of MA1–x FA x PbI3 perovskite solar cells”. In: *Nature Energy* 6.6 (2021), pp. 624–632.

[173] Valter H Carvalho-Silva, Nayara D Coutinho, and Vincenzo Aquilanti. “Temperature dependence of rate processes beyond Arrhenius and Eyring: Activation and Transitivity”. In: *Frontiers in chemistry* 7 (2019), p. 380.

[174] Sidney W Benson and Otto Dobis. “Existence of negative activation energies in simple bimolecular metathesis reactions and some observations on too-fast reactions”. In: *The Journal of Physical Chemistry A* 102.27 (1998), pp. 5175–5181.

[175] Neo Lin and Tomoyasu Mani. “Anti-Arrhenius behavior of electron transfer reactions in molecular dimers”. In: *Chemical Science* 14.45 (2023), pp. 13095–13107.

[176] Einav Scharf et al. “Ligands mediate anion exchange between colloidal lead-halide perovskite nanocrystals”. In: *Nano Letters* 22.11 (2022), pp. 4340–4346.

[177] RI Dawood, AJ Forty, and MR Tubbs. “The photodecomposition of lead iodide”. In: *Proceedings of the Royal Society of London. Series A. Mathematical and Physical Sciences* 284.1397 (1965), pp. 272–288.

[178] Fanglong Yuan et al. “Color-pure red light-emitting diodes based on two-dimensional lead-free perovskites”. In: *Science Advances* 6.42 (2020), eabb0253.

[179] Zhengguo Xiao et al. “Efficient perovskite light-emitting diodes featuring nanometre-sized crystallites”. In: *Nature Photonics* 11.2 (2017), pp. 108–115.

[180] VG Vasavi Dutt et al. “High-quality CsPbX3 (X= Cl, Br, or I) perovskite nanocrystals using ascorbic acid post-treatment: implications for light-emitting applications”. In: *ACS Applied Nano Materials* 5.5 (2022), pp. 5972–5982.

[181] Brent A Koscher et al. “Essentially trap-free CsPbBr3 colloidal nanocrystals by postsynthetic thiocyanate surface treatment”. In: *Journal of the American Chemical Society* 139.19 (2017), pp. 6566–6569.

[182] Jingjing He et al. “Surface chelation of cesium halide perovskite by dithiocarbamate for efficient and stable solar cells”. In: *Nature communications* 11.1 (2020), p. 4237.

[183] Gee Yeong Kim et al. “Photo-Effect on Ion Transport in Mixed Cation and Halide Perovskites and Implications for Photo-Demixing”. In: *Angewandte Chemie* 133.2 (2021), pp. 833–839.

[184] Gee Yeong Kim et al. “Large tunable photoeffect on ion conduction in halide perovskites and implications for photodecomposition”. In: *Nature materials* 17.5 (2018), pp. 445–449.

[185] X Hong, T Ishihara, and AV Nurmikko. “Dielectric confinement effect on excitons in PbI 4-based layered semiconductors”. In: *Physical Review B* 45.12 (1992), p. 6961.

[186] Mingzhen Liu, Michael B Johnston, and Henry J Snaith. “Efficient planar heterojunction perovskite solar cells by vapour deposition”. In: *Nature* 501.7467 (2013), pp. 395–398.

[187] Martin A Green, Anita Ho-Baillie, and Henry J Snaith. “The emergence of perovskite solar cells”. In: *Nature photonics* 8.7 (2014), pp. 506–514.

[188] Himchan Cho et al. “Overcoming the electroluminescence efficiency limitations of perovskite light-emitting diodes”. In: *Science* 350.6265 (2015), pp. 1222–1225.

[189] Do-Hyun Kwak et al. “High performance hybrid graphene–CsPbBr 3- x I x perovskite nanocrystal photodetector”. In: *RSC advances* 6.69 (2016), pp. 65252–65256.

[190] Jia Liang et al. “All-inorganic perovskite solar cells”. In: *Journal of the American Chemical Society* 138.49 (2016), pp. 15829–15832.

[191] Jian Wang et al. “Reducing surface recombination velocities at the electrical contacts will improve perovskite photovoltaics”. In: *ACS Energy Letters* 4.1 (2018), pp. 222–227.

[192] Abhishek Swarnkar et al. “Quantum dot–induced phase stabilization of α-CsPbI3 perovskite for high-efficiency photovoltaics”. In: *Science* 354.6308 (2016), pp. 92–95.

[193] Jun Kang and Lin-Wang Wang. “High defect tolerance in lead halide perovskite CsPbBr3”. In: *The journal of physical chemistry letters* 8.2 (2017), pp. 489–493.

[194] Gabriele Rainò et al. “Single cesium lead halide perovskite nanocrystals at low temperature: fast single-photon emission, reduced blinking, and exciton fine structure”. In: *ACS nano* 10.2 (2016), pp. 2485–2490.

[195] Guanhua Ying et al. “Highly Efficient Photoluminescence and Lasing from Hydroxide Coated Fully Inorganic Perovskite Micro/Nano-Rods”. In: *Advanced Optical Materials* 8.23 (2020), p. 2001235.

[196] Sergii Yakunin et al. “Low-threshold amplified spontaneous emission and lasing from colloidal nanocrystals of caesium lead halide perovskites”. In: *Nature communications* 6.1 (2015), p. 8056.

[197] Wenna Du et al. “Strong exciton–photon coupling and lasing behavior in all-inorganic CsPbBr3 micro/nanowire Fabry-Pérot cavity”. In: *ACS Photonics* 5.5 (2018), pp. 2051–2059.

[198] Michael A Becker et al. “Bright triplet excitons in caesium lead halide perovskites”. In: *Nature* 553.7687 (2018), pp. 189–193.

[199] Gabriele Rainò et al. “Superfluorescence from lead halide perovskite quantum dot superlattices”. In: *Nature* 563.7733 (2018), pp. 671–675.

[200] Andre K Geim and Konstantin S Novoselov. “The rise of graphene”. In: *Nature materials* 6.3 (2007), pp. 183–191.

[201] Rahul Raveendran Nair et al. “Fine structure constant defines visual transparency of graphene”. In: *science* 320.5881 (2008), pp. 1308–1308.

[202] Jiangni Yun et al. “Enhanced optical absorption and interfacial carrier separation of CsPbBr3/graphene heterostructure: Experimental and theoretical insights”. In: *ACS applied materials & interfaces* 12.2 (2019), pp. 3086–3095.

[203] Youngbin Lee et al. “High-performance perovskite–graphene hybrid photodetector”. In: *Advanced materials* 27.1 (2015), pp. 41–46.

[204] Jun Kang, Jingbo Li, and Su-Huai Wei. “Atomic-scale understanding on the physics and control of intrinsic point defects in lead halide perovskites”. In: *Applied Physics Reviews* 8.3 (2021).

[205] Jun Pan et al. “Halogen Vacancies Enable Ligand-Assisted Self-Assembly of Perovskite Quantum Dots into Nanowires”. In: *Angewandte Chemie International Edition* 58.45 (2019), pp. 16077–16081.

[206] Jan Meiss et al. “Fluorinated Zinc Phthalocyanine as Donor for Efficient Vacuum-Deposited Organic Solar Cells”. In: *Advanced Functional Materials* 22.2 (2012), pp. 405–414.

[207] Youngsin Park et al. “Enhanced photoluminescence quantum yield of MAPbBr 3 nanocrystals by passivation using graphene”. In: *Nano Research* 13 (2020), pp. 932–938.

[208] DY Lei, J Li, and HC Ong. “Tunable surface plasmon mediated emission from semiconductors by using metal alloys”. In: *Applied Physics Letters* 91.2 (2007).

[209] Koichi Okamoto et al. “Surface-plasmon-enhanced light emitters based on InGaN quantum wells”. In: *Nature materials* 3.9 (2004), pp. 601–605.

[210] YL Chen et al. “Effect of graphene on photoluminescence properties of graphene/GeSi quantum dot hybrid structures”. In: *Applied Physics Letters* 105.2 (2014).

[211] Yulu Chen et al. “The photoelectric response of the graphene/GeSi QDs hybrid structure”. In: *Nanotechnology* 29.50 (2018), p. 504005.

[212] David Pines. “Collective energy losses in solids”. In: *Reviews of modern physics* 28.3 (1956), p. 184.

[213] Kasper v an Wijk. *Classical Electrodynamics*. 1999.

[214] Lukas Novotny and Bert Hecht. *Principles of nano-optics*. Cambridge university press, 2012.

[215] En Cao et al. “Exciton-plasmon coupling interactions: from principle to applications”. In: *Nanophotonics* 7.1 (2018), pp. 145–167.

[216] Heinz Faether. “Surface plasmons”. In: *Smooth and Rough Surfaces and on Gratings (Springer Tracts in Modem Physics 111* (1988), pp. 642–646.

[217] Georg Kresse and Jürgen Furthmüller. “Efficiency of ab-initio total energy calculations for metals and semiconductors using a plane-wave basis set”. In: *Computational materials science* 6.1 (1996), pp. 15–50.

[218] John P Perdew, Kieron Burke, and Matthias Ernzerhof. “Generalized gradient approximation made simple”. In: *Physical review letters* 77.18 (1996), p. 3865.

[219] Alexandre Tkatchenko and Matthias Scheffler. “Accurate molecular van der Waals interactions from ground-state electron density and free-atom reference data”. In: *Physical review letters* 102.7 (2009), p. 073005.

[220] Insung Hwang et al. “Enhancing stability of perovskite solar cells to moisture by the facile hydrophobic passivation”. In: *ACS applied materials & interfaces* 7.31 (2015), pp. 17330–17336.

[221] Michael Kulbak et al. “Cesium enhances long-term stability of lead bromide perovskite-based solar cells”. In: *The journal of physical chemistry letters* 7.1 (2016), pp. 167–172.

[222] Sung Won Hwang et al. “Plasmon-enhanced ultraviolet photoluminescence from hybrid structures of graphene/ZnO films”. In: *Physical Review Letters* 105.12 (2010), p. 127403.

[223] Juan A Castañeda et al. “Efficient biexciton interaction in perovskite quantum dots under weak and strong confinement”. In: *ACS nano* 10.9 (2016), pp. 8603–8609.

[224] Xiangtian Xiao et al. “Enhanced hole injection assisted by electric dipoles for efficient perovskite light-emitting diodes”. In: *Communications Materials* 1.1 (2020), p. 81.

[225] Frédéric Joucken et al. “Localized state and charge transfer in nitrogen-doped graphene”. In: *Physical Review B* 85.16 (2012), p. 161408.

[226] Jiangtian Li et al. “Plasmon-induced resonance energy transfer for solar energy conversion”. In: *Nature Photonics* 9.9 (2015), pp. 601–607.

[227] Xinyu Huang et al. “Efficient plasmon-hot electron conversion in Ag–CsPbBr3 hybrid nanocrystals”. In: *Nature communications* 10.1 (2019), p. 1163.

[228] Koichi Okamoto et al. “High-efficiency light emission by means of exciton–surface-plasmon coupling”. In: *Journal of Photochemistry and Photobiology C: Photochemistry Reviews* 32 (2017), pp. 58–77.

[229] Mohamed Farhat, Sébastien Guenneau, and Hakan Bağcı. “Exciting graphene surface plasmon polaritons through light and sound interplay”. In: *Physical review letters* 111.23 (2013), p. 237404.

[230] Yu Liu et al. “Plasmon dispersion and damping in electrically isolated two-dimensional charge sheets”. In: *Physical Review B* 78.20 (2008), p. 201403.

[231] Yu Liu and Roy F Willis. “Plasmon-phonon strongly coupled mode in epitaxial graphene”. In: *Physical Review B* 81.8 (2010), p. 081406.

[232] Marina R Filip, Jonah B Haber, and Jeffrey B Neaton. “Phonon screening of excitons in semiconductors: halide perovskites and beyond”. In: *Physical review letters* 127.6 (2021), p. 067401.

[233] Andrés. F. Gualdrón-Reyes et al. “Controlling the Phase Segregation in Mixed Halide Perovskites through Nanocrystal Size”. In: *ACS Energy Letters* 4.1 (2019). PMID: 30662954, pp. 54–62.

[234] Jun-Ho Park et al. “Reduction of Hole Carriers by van der Waals Contact for Enhanced Photoluminescence Quantum Yield in Two-Dimensional Tin Halide Perovskite”. In: *ACS Energy Letters* 8.8 (2023), pp. 3536–3544.

[235] K Ramakanth. “Basics of X-ray Diffraction and its Application”. In: *IK, New Delhi* (2007).

[236] Challapalli Suryanarayana et al. *X-rays and Diffraction*. Springer, 1998.

[237] John Frederick Nye. *Physical properties of crystals: their representation by tensors and matrices*. Oxford university press, 1985.